Imaging Polarimeter for a Sub-MeV Gamma-Ray All-sky Survey Using an Electron-tracking Compton Camera

Shotaro Komura

Department of Physics, Faculty of Science, Kyoto University
Kitashirakawa Oiwake-cho, Sakyo-ku, Kyoto, 606-8502, Japan
komura@cr.scphys.kyoto-u.ac.jp

This thesis was submitted to the Department of Physics,
Graduate School of Science, Kyoto University
on November 6, 2017
in partial fulfillment of the requirements
for the degree of Doctor of Philosophy in physics.

Abstract

X-ray and gamma-ray polarimetry is a promising tool to study the geometry and the magnetic configuration of various celestial objects, such as binary black holes or gamma-ray bursts (GRBs). However, statistically significant polarizations have been detected in few of the brightest objects. Even though future polarimeters using X-ray telescopes are expected to observe weak persistent sources, there are no effective approaches to survey transient and serendipitous sources with a wide field of view (FoV). Here we present an electron-tracking Compton camera (ETCC) as a highly sensitive gamma-ray imaging polarimeter. The ETCC provides powerful background rejection and a high modulation factor over an FoV of up to 2π sr thanks to its excellent imaging based on a well-defined point-spread function. Importantly, we demonstrated for the first time the stability of the modulation factor under realistic conditions of off-axis incidence and huge backgrounds using the SPring-8 polarized X-ray beam. The measured modulation factor of the current ETCC was 0.65±0.01 at 154 keV for the off-axis incidence with the oblique angle of 30° and was not degraded compared to the 0.58±0.02 at 130 keV for the on-axis incidence. These measured results are well consistent with the simulation results. Consequently, we found that the satellite-ETCC proposed in Tanimori et al. would provide all-sky surveys of weak persistent sources of 13 mCrab with 10% polarization for a 10^7 s exposure and over 20 GRBs down to a 6×10^{-6} erg cm^{-2} fluence and 10% polarization during a one-year observation.

Contents

Chapter 1

Introduction

X-ray and gamma-ray polarimetry in astronomy is widely viewed as a new probe for important open questions about high-energy sources such as gamma-ray bursts (GRBs), binary black holes (BBHs), active galactic nuclei (AGNs), and pulsars. For example, statistical observations of GRB polarizations in the energy range of several tens of keV to a few MeV will be able to constrain competitive emission models with different magnetic field structures, for which current photometric and spectroscopic observations hardly constraint (Toma et al., 2009). In addition, BBHs and AGNs are thought to emit linearly polarized X-rays and gamma-rays due to scattering processes in their accretion disks, and therefore the measurement of these polarization properties and their energetic variations will enable us to determine the corona geometry, which is too small to be spatially resolved by current imaging observations (Schnittman & Krolik, 2010).

Despite their scientific importance, statistically significant polarization results have been reported in only a few of the brightest celestial X-ray and gamma-ray objects over the past four decades. In the 1970s, the Bragg-reflection X-ray polarimeter on board the *OSO-8* satellite first detected the polarization of the Crab nebula at 2.6 and 5.2 keV (Weisskopf et al., 1978) and measured the upper limits for several X-ray objects (Long et al., 1980; Hughes et al., 1984). In the 2000s, two coded-mask detectors on board the *INTEGRAL* satellite reported the polarization of the Crab nebula in the energy band between 0.1 MeV and 1 MeV (Dean et al., 2008; Forot et al., 2008); however, these results are plagued by large uncertainties because the instruments were not designed or calibrated for polarimetric observations. As for transient objects, many recent studies have reported that the prompt gamma-ray emission of several GRBs showed a high degree of polarization of 30–80% and a time variation in the polarization direction in the energy band between 70 keV and 2 MeV. However, the statistical significances of these studies were marginal (2–3σ level). Due to the lack of imaging capabilities, they also have difficulty evaluating the systematic errors originated from the huge background in space.

The current approaches to X-ray and gamma-ray polarimetry are classified roughly into two types. The first is a pointing polarimeter that aims to observe persistent sources

with a flux of 10–100 mCrab with high sensitivity (Soffitta et al., 2013; Beilicke et al., 2014; Weisskopf et al., 2016; Iwakiri et al., 2016; Krawczynski et al., 2016; Chauvin et al., 2016a; Katsuta et al., 2016). These polarimeters use a X-ray focusing mirror or a fine collimator to suppress the background which causes serious degradation in the polarization sensitivity. The second approach is a wide field of view (FoV) polarimeter with large detection area (Bloser et al., 2009; Yonetoku et al., 2011a; Orsi & Polar Collaboration, 2011; Gunji et al., 2014; Yatsu et al., 2014); these are dedicated to observations of bright transient objects, especially prompt emissions of bright and short-duration GRBs. Even though a wide FoV increases the chance of GRB detection, it also accepts a huge background contribution coming from all directions. Therefore, these polarimeters have difficulty observing low signal-to-noise ratio sources, such as persistent sources and long-duration GRBs which last several tens of seconds or more. Even though these wide FoV polarimeters require the uniform sensitivity in the whole FoV to suppress the systematic effects, it is not yet realized. As mentioned above, there are no promising approaches to simultaneously explore both persistent and transient polarized sources in the universe; an X-ray or gamma-ray polarimeter with both a moderate sensitivity and a wide FoV is required.

In the energy range from a few hundreds of keV to a few tens of MeV, Compton cameras have been studied as gamma-ray imaging telescopes capable of polarimetry and wide FoV. A clear gamma-ray image based on a well-defined point spread function (PSF) could provide powerful background suppression by constraining the direction of incident photons. However, the Imaging Compton telescope (COMTEPL) (Schoenfelder et al., 1993), the only satellite-borne Compton camera, eventually indicated that it is difficult to reduce the background sufficiently using gamma-ray images obtained by via conventional Compton cameras (Weidenspointner et al., 2001; Schönfelder, 2004).

As a next-generation MeV gamma-ray telescope, we have demonstrated the performance of an electron-tracking Compton camera (ETCC) utilizing a gaseous three-dimensional electron tracker since 2004 (Tanimori et al., 2004). The fine electron tracking enables us to reduce the PSF dramatically and consequently greatly improve the detection and polarization sensitivity. In Tanimori et al. (2015), we experimentally demonstrated that our ETCC has the ability to form a well-defined PSF of several degrees in the energy range from 100 keV to a few MeV. Such a sharp PSF reduces a huge background contribution coming from all directions by nearly 3 orders of magnitude without any heavy shield, similarly to the focusing telescope, compared to typical non-imaging gamma-ray detectors such as coded-mask detectors and GRB polarimeters mentioned above. The satellite model ETCC is expected to have an effective area of 240 cm^2 with a PSF of 2° at 1 MeV, and the detection sensitivity would reach 1 mCrab flux at 1 MeV in a 10^6 s observation (Tanimori et al., 2015). Thanks to its powerful background suppression and wide FoV of up to 2π sr (Matsuoka et al., 2015), an ETCC has the capabilities of a highly-sensitive gamma-ray polarimeter that can be used not only to survey new faint persistent sources but also to observe transient objects including GRBs.

In this thesis, we investigate the basic polarimetric performance of the ETCC using both Monte Carlo simulations and experiments performed in the linearly polarized hard X-ray beamline at SPring-8. We begin with an overview of the potential MeV gamma-ray sources of polarized emission, including a theoretical predictions and the observational polarization results. In Chapter 3, we explain the principles of a Compton polarimeter, and how the polarization measurements are disturbed by the statistical and systematic errors in space. In Chapter 4, we review the astronomical Compton polarimeters by dividing them into the following four types: non-dedicated instruments, pointing polarimeters, GRB polarimeters, and Compton cameras. In Chapter 5, we present the detector configurations and the performances of the ETCC. In Chapter 6, we describe the polarimetric performance of the ETCC using the Monte Carlo simulation. In Chapter 7, we report the analysis and results of the beam experiments. Finally, we discuss the polarization sensitivities for future all-sky surveys using balloons and satellites in Chapter 8.

Chapter 2

Polarization in MeV Gamma-Ray Astronomy

2.1 MeV Gamma-ray Sources

The gamma-ray imaging and spectroscopic survey in MeV region was only performed by COMPTEL onbord *Compton Gamma-Ray Observatory (CGRO)* satellite launched in 1991 (Schoenfelder et al., 1993). As shown in Table 2.1, COMPTEL detected only 32 persistent sources and 31 transient sources in the 0.75–30 MeV band (Schönfelder et al., 2000). The *INTEGRAL*/IBIS reported the catalogue of the all sky survey in the sub-MeV band (100–300 keV), which includes 113 persistent sources at a significance above 5σ (Krivonos et al., 2015). These number of the detected sources in sub-MeV and MeV bands are quite smaller than that of *Swift* and *Fermi*/LAT, which detected 1171 sources in the 14–195 keV band (Baumgartner et al., 2013) and more than 3000 sources in the 0.1–100 GeV band (Nolan et al., 2012), respectively. This divergence is explained by the poor sensitivity in MeV region as shown in Figure 2.1.

Despite of the large amount of imaging and spectroscopic observations in X-ray and sub-GeV region, there are still remaining open questions, such as the prompt emission mechanism of GRBs and the origin of the seed photons for inverse-Compton scattering emission in AGNs. Therefore, we need not only to improve the imaging and spectroscopic sensitivity in MeV band but also to use the polarization properties in addition to the image and the energy spectrum of the astronomical objects.

2.2 Potential Sources of Polarized Emission

Polarization measurement provides two additional observational parameters, the degree of polarization and the polarization direction of the source emission, which enables us to discriminate the competing physics models. The only dedicated X-ray polarimetry mission to date is the *OSO-8* experiment, which detected the polarization of the Crab nebula at

Table 2.1: The detected sources with COMPTEL (Schönfelder et al., 2000).

Spin-Down Pulsars	3	Crab, Vela, PSR 1509-58
Other Galactic sources	7	Cyg X-1, Crab Nebula, etc.
Active Galactic Nuclei	10	Cen A, etc.
Gamma-Ray Line Source	7	SN1991T (^{56}Co), etc.
Unidentified Sources	5	
Total Number	32	
Gamma-Ray Burst	31	

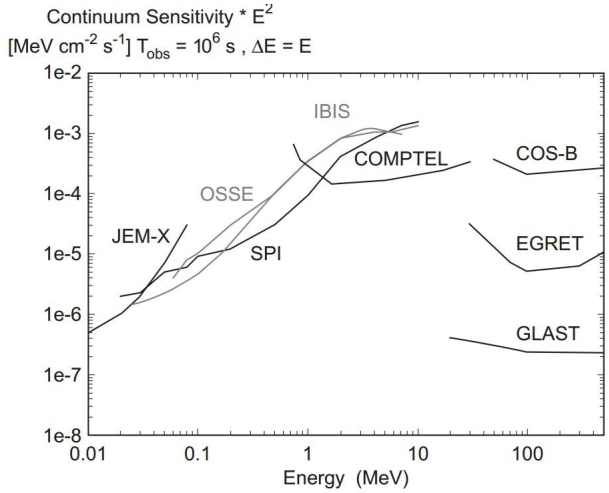

Figure 2.1: Sensitivity for continuum in X-ray and gamma-ray region (Schönfelder, 2004).

2.6 and 5.2 keV (Weisskopf et al., 1978). The recent progress of X-ray detectors, such as an increasing efficiency of the X-ray focusing mirrors, enables to design highly-sensitive X-ray polarimeters (Soffitta et al., 2013; Weisskopf et al., 2016), whose sensitivities are more than two orders of magnitude better than that of *OSO-8*. For those reasons, the scientific importances of X-ray polarimetry (< 100 keV) has already been well discussed (for recent review see Krawczynski et al. 2011, and Soffitta et al. 2013). In the following section, we focus on the scientific importances of sub-MeV/MeV gamma-ray polarimetry (> 100 keV) for GRBs, AGNs, BHBs, and Pulsars, according to the results of COMPTEL.

2.2.1 Gamma-Ray Bursts

Gamma-ray bursts (GRBs) are the most luminous transient objects in gamma-ray region, whose luminosity reach 10^{54} erg s^{-1}. Burst and Transient Source Experiment (BATSE) on *CGRO* reveals that GRBs are isotropically distributed in the sky with an occurrence rate of roughly one every day (Kouveliotou et al., 1993; Fishman, 1999). The observed distribution of burst durations are shown in in Figure 2.2, which suggest that GRBs can be separated into two classes, short events (< 2 s) and longer ones (> 2 s) (Kouveliotou et al.,

1993; Fishman, 1999). The typical time-averaged emission spectrum such as Figure 2.3 is well described by a broken power-law with a smooth break at a characteristic energy, E-peak (E_p) (Band et al., 1993). The observed distribution of E_p values range from ∼10 keV up to at least 1 MeV, with a broad peak near 200 keV as shown in Figure 2.4. After the burst emission, broadband afterglows have been observed from the radio band up to X-ray band, as first reported in Costa et al. (1997). These emission characteristics of GRBs has generally been explained by the internal-external shocks scenario: prompt gamma-ray emission is produced by the dissipation in the relativistic jet ejected from the center of the explosion, and the afterglow is the synchrotron emission of electrons accelerated by the interaction of the jet with external matters. However, this scenario is still under investigation especially for the prompt emission.

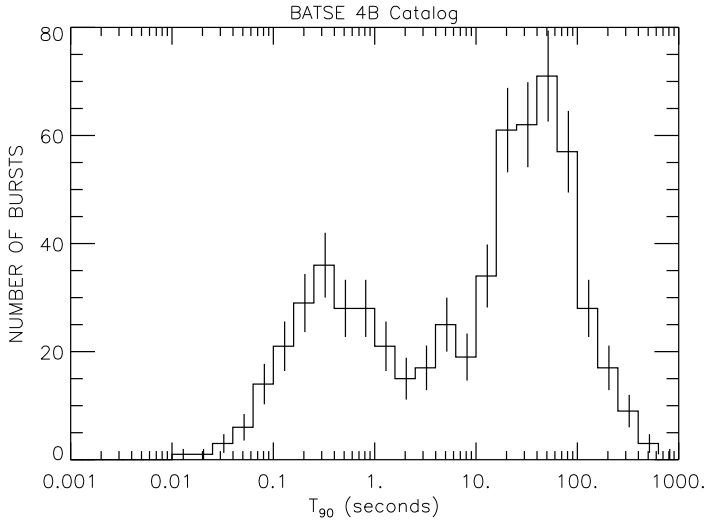

Figure 2.2: Durations of the 2704 GRBs recorded with the BATSE on board *CGRO* (Mallozzi, 2014).

Many polarization measurements have been performed for the radio and optical afterglows (e.g., Covino & Gotz 2016 and earlier references therein), providing highly significant polarization level of $< 30\%$, which is the strong observational evidence for the synchrotron origin of the afterglow emission. In prompt gamma-ray emission, polarization observations are a unique probe to understand the prompt emission mechanism. Prompt emission models are often classified into two general types, intrinsic and geometric models (for recent reviews see Covino & Gotz 2016; McConnell 2017). Intrinsic models assume an intrinsic characteristics, namely a globally ordered magnetic field in the emission region. In this case, the polarization properties depend on the uniformity of the magnetic field of the synchrotron jet, and when the typical degrees of polarization range from $\sim 20\%$ up to $\sim 60\%$ is expected (described as SO model in the following Figure 2.5). Geometric models assume a random magnetic field and require an optimistic viewing direction to observe a high degree of polarization, whether the emission mechanism is synchrotron or

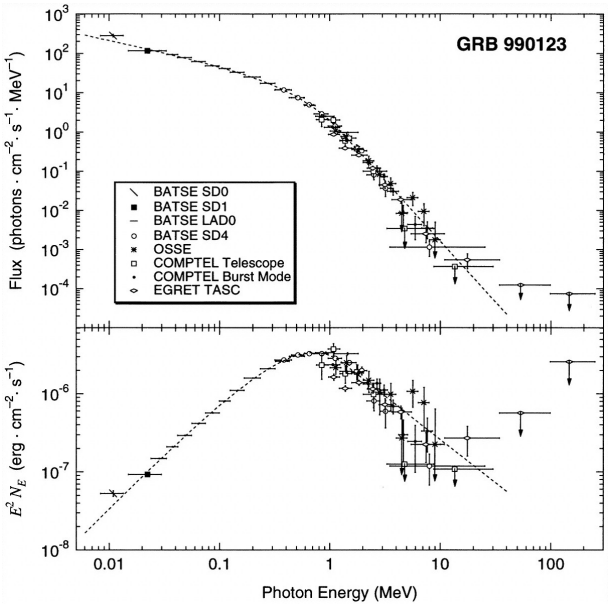

Figure 2.3: Energy spectrum of GRB 990123 (Briggs et al., 1999).

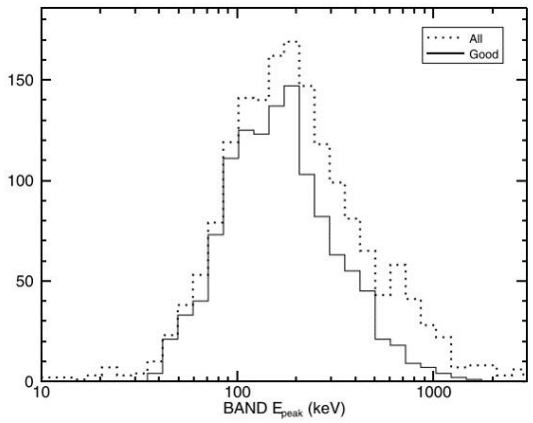

Figure 2.4: Distributions of E_p (Goldstein et al., 2013).

inverse Compton. The typical degree of polarization is $< 20\%$ for most viewing angles, although synchrotron emission can produce the degree of polarization as high as $\sim 70\%$ (SR model), and inverse Compton models (CD model) can achieve $\sim 100\%$ of degree of polarization under optimistic geometries. Therefore, the intrinsic and geometric models can be distinguished by a statistical study of polarization properties in prompt emission (Toma et al., 2009). In particular, the dependence of the degree of polarization on E_p can be a clear diagnostic, as shown in Figure 2.5.

The polarimetric observations of the prompt gamma-ray emission to date are summarized in Table 2.2. These studies have reported a high degree of polarization of 30%–80% and a time variation in the polarization signatures in some GRBs. Some authors suggested that the prompt emissions of the GRBs are more likely to originate in synchrotron radiation, and the direction of the magnetic field varies temporally or spatially. However the statistical significances of all studies were marginal, typically having a confidence level of 2–3σ. Even in the experiments by the Gamma-Ray Burst Polarimeter (GAP; Yonetoku et al. 2011a), which is optimized for the GRB polarimetry, only three GRBs are detected with the significance of 3σ level ($<3.7\sigma$).

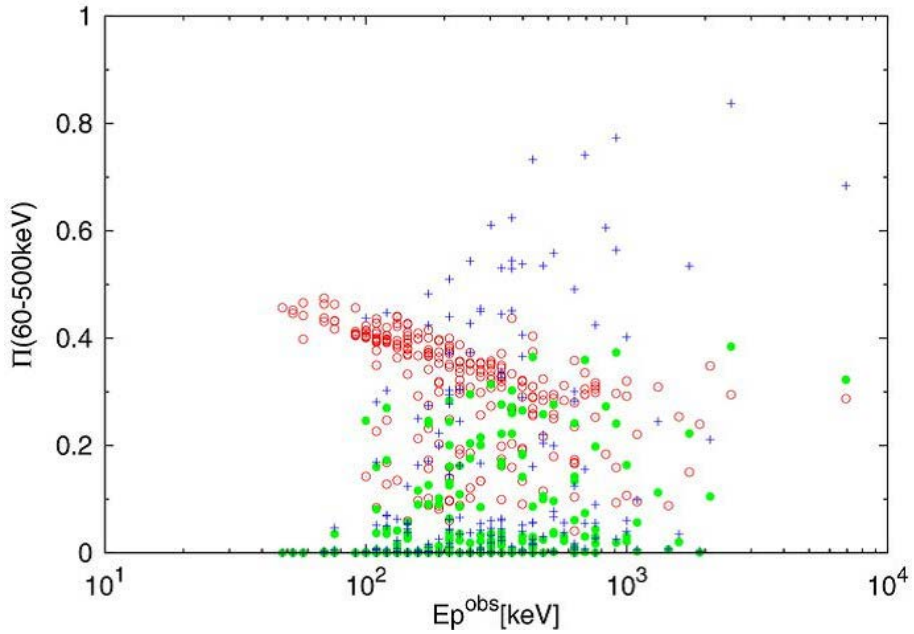

Figure 2.5: Simulated distribution of the degree of polarization as a function of E_p in the SO (red open circles), SR (green filled circles), and CD (blue plus signs) models (Toma et al., 2009).

Table 2.2: GRB polarization observations for prompt gamma-ray emission. Table adapted from McConnell (2017).

Pub Date	GRB	Instrument	Energy (keV)	Degree of Polarization
2004	GRB 021206	RHESSI	150–2000	80%±20%
2004	GRB 021206	RHESSI	150–2000	$< 4.1\%$
2004	GRB 021206	RHESSI	150–2000	$41^{+57}_{-44}\%$
2005	GRB 930131	CGRO/BATSE	20–1000	(35–100%)[a]
2005	GRB 960924	CGRO/BATSE	20–1000	(50–100%)[a]
2007	GRB 041219a	INTEGRAL/SPI	100–350	98%±33%
2007	GRB 041219a	INTEGRAL/SPI	100–350	96%±40%
2009	GRB 041219a	INTEGRAL/IBIS	200–800	43%±25%[b]
2009	GRB 061122	INTEGRAL/SPI	100–1000	$< 60\%$
2011	GRB 100826a	IKAROS/GAP	70–300	27%±11%[c]
2012	GRB 110301a	IKAROS/GAP	70–300	70%±22%
2012	GRB 110721a	IKAROS/GAP	70–300	80%±22%
2013	GRB 061122	INTEGRAL/IBIS	250–800	$> 60\%$
2014	GRB 140206a	INTEGRAL/IBIS	200–800	$> 48\%$
2016	GRB 151006a	Astrosat/CZTI	100–300	–

[a] albedo polarimetry
[b] variable degree of polarization
[c] variable polarization angle

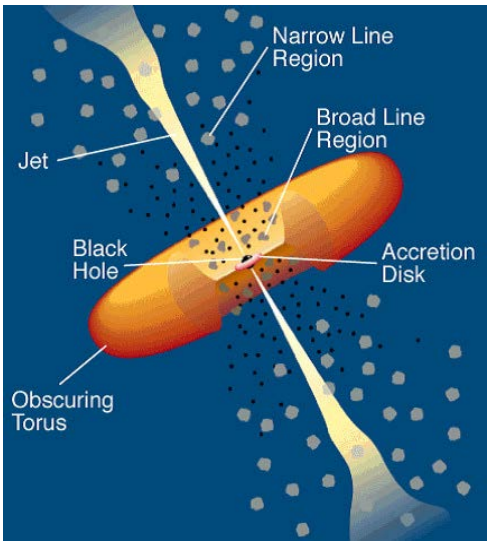

Figure 2.6: The schematic view of AGN.
Retrieved from https://heasarc.gsfc.nasa.gov/docs/cgro/images/epo/gallery/agns/index.html

2.2.2 Active Galactic Nuclei

An active galactic nucleus (AGN) is thought to be a compact region at the center of a host galaxy with a strong broadband emission. The radiation from an AGN is believed to be a result of accretion of matter by a supermassive black hole at the center of its host galaxy. Figure 2.6 shows the schematic view of the unified model of AGN. Radio and optical band observation indicates that many AGN have relativistic jet outflows. The AGNs dominated by relativistic jets pointing in our direction are commonly known as blazars. Blazars are characterized by a non-thermal spectral energy distribution, where two broad components exhibit as shown in Figure 2.7. The low-energy component is in the range of radio to UV or even X-rays, and the high-energy component starts from the X-ray band and can reach TeV or even higher energies. The high-energy component of flat-spectrum radio quasar (FSRQ) type blazars is expected to be peaked in MeV band as shown on the left in Figure 2.7.

It is expected that the low-energy component is due to the synchrotron radiation of the relativistic electrons. Indeed, measurements in the radio and optical bands showed a polarization level of a few percent up to as much as 40%. The high-energy component is construed to be typically associated with inverse-Compton scattering of low-energy photons (leptonic models), although the origin of the seed photons is less well understood. The polarization measurement would be the key to distinguish between the following scenarios: (i) Seed photons are the synchrotron photons emitting in the optical/UV band (synchrotron self Compton model). In this case, the polarization of the hard X-rays is expected to track the polarization at radio and optical bands. If the magnetic fields are perfectly ordered, the degree of polarization would reach $> 30\%$ (Poutanen, 1994). (ii)

Seed photons are the accretion disk photons or the emission coming from broad line region (external Compton model). In this case, the high-energy component will have a relatively small fraction of polarization (<10%) (McNamara et al., 2009).

It has been pointed out that high energy proton in the jet can be induced by hadronic interactions (hadronic model). Because of the dominance of synchrotron radiation in hadronic models, a high polarization is expected compared to that for leptonic models (Zhang & Böttcher, 2013). In the case of famous FSRQ-type blazar 3C279, as shown in Figure 2.8, the degree of polarization of hadronic models is over 0.6 in the wide energy band, on the other hand that of leptonic models approaches to 0 as increased the energy.

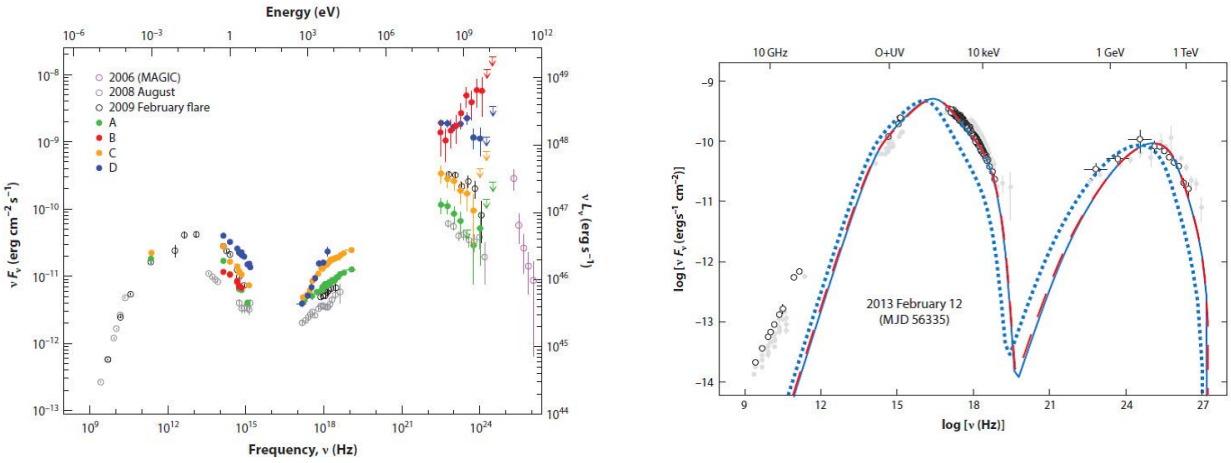

Figure 2.7: The broadband spectral energy distribution of the FSRQ-type blazar 3C279 (left panel) and the high-synchrotron-peak BL-type blazar Mkn421 (right panel) (Madejski & Sikora, 2016).

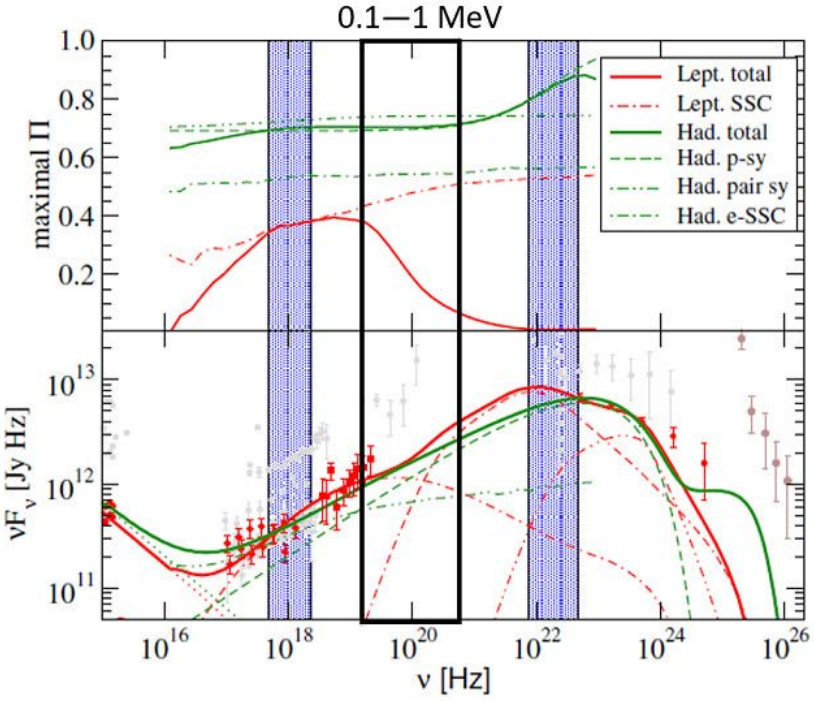

Figure 2.8: UV through gamma-ray spectrum energy distributions (lower panel) and maximum degree of polarization (upper panel) for the FSRQs 3C279. Leptonic model fits are plotted in red and hadronic models in green. Black bold-framed area indicate the 0.1–1 MeV range. Figure adapted from Zhang & Böttcher (2013).

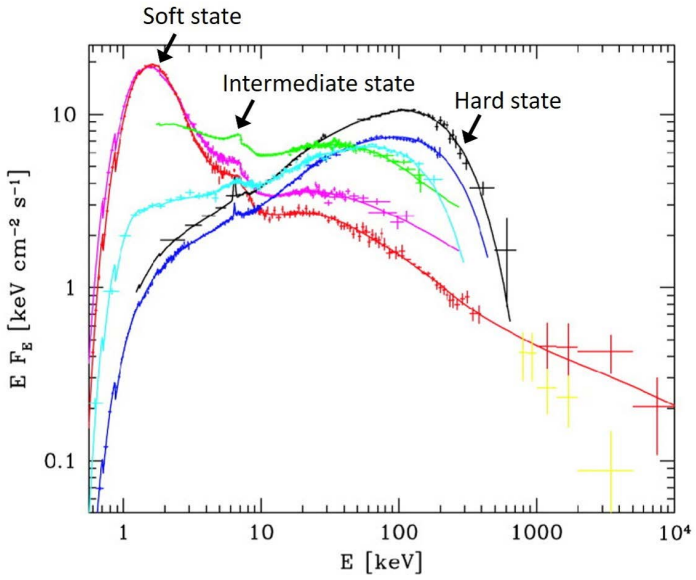

Figure 2.9: The energy spectra of Cygnus X-1 in soft state, hard state, and intermediate state (Zdziarski et al., 2002).

2.2.3 Binary Black Holes

In the final evolution of a massive star with a mass above $30M_{\odot}$, the core is considered to collapse to a black hole after a type II supernova. Binary black hole (BHB) is a binary system with a black hole and a companion star, where an accretion disk is created because the matter from the companion star flows onto the black hole. This accretion disk radiates photons in wide band including X-rays and gamma-rays.

It is well known that BHB transit through different spectral states during their outbursts. The two main states are the soft state and the hard state. In addition, the intermediate state exists between the soft and hard state. Figure 2.9 shows the spectra of the soft, hard and intermediate state of Cyg X-1, which is one of the most well-studied black hole binary. The X-ray spectrum in the soft state is generally associated with a blackbody radiation from the accretion disk with a characteristic temperature of $\sim$ 1 keV. In the hard state, the X-ray and γ-ray spectrum is generally described by a power law model with an exponential cutoff at about 100 keV. The standard explanation for the high energy emission is a inverse Compton scattering of disk photons by hot ($\sim$ 100 keV) thermal electrons (corona) in the inner region of the accretion flow and its reflection component at the disk. However, it has been observed that some bright sources exhibit an excess of emission above 300 keV, extending to the MeV range, whose emission mechanism is still under debate.

X-ray and gamma-ray polarization measurement of BHB is conventionally expected as the probe to investigate the geometrical distribution of corona in hard state.Schnittman & Krolik (2010) calculated the expected polarization signatures for various corona geometries be-

low 100 keV, and they predicted that the degree of polarization would be $< 10\%$ for any corona geometries even with small differences. Recent findings of high polarization in Cygnus X-1 by INTEGRAL suggests that gamma-ray polarization measurements enable us to understand the emission mechanism of the high-energy tail. Laurent et al. (2011) reported that the degree of polarization of Cygnus X-1 between 400 keV and 2 MeV is $67\pm30\%$, whereas they obtained only a 20% upper limit in the 250–400 keV band. Its high degree of polarization suggests that the high-energy tail is due to synchrotron emission from a compact jet. An alternative model was introduced by Romero et al. (2014), where the MeV tail is the synchrotron radiation of secondary non-thermal electrons in the corona. This coronal model also predicts significant polarization during intermediate states, therefore this can be tested in the future sub-MeV gamma-ray polarimetric observations (Romero et al., 2014).

2.2.4 Pulsars

Pulsars radiate a short periodic pulse, and hence are considered to be neutron stars spinning with a high speed. A neutron star also has a strong magnetic field of about 10^{12} G. Because the magnetic axis inclines to the rotation axis generally, the emission near the magnetic poles sweeps around the rotation axis. Since the emission region of the pulsar rotating around the axis is observed from the earth, we see it like a light house. Within thousand pulsars observed so far, the emission of MeV gamma-rays are only observed from several of them.

The Crab pulsar, one of the most famous pulsars, has a nebula around it. The Crab pulsar and the Crab nebula have been well observed from the radio to the TeV gamma-ray as shown in Figure 2.10. In the MeV range, both the pulsar and nebular components contribute significantly to the total emission. The hard X-ray and gamma-ray emission is explained by synchrotron radiation and at higher energies via inverse Compton scattering. The bright synchrotron radiation is a good probe for detailed studies of the inner region of the Crab pulsar and the Crab nebula. The polarized gamma-ray emission from the nebula and pulsar have been measured, having a confidence level of 5σ. The results of these measurements are summarized in Figure 2.11. More precise measurements are required to confirm the energy dependence or the time variation of the polarization states.

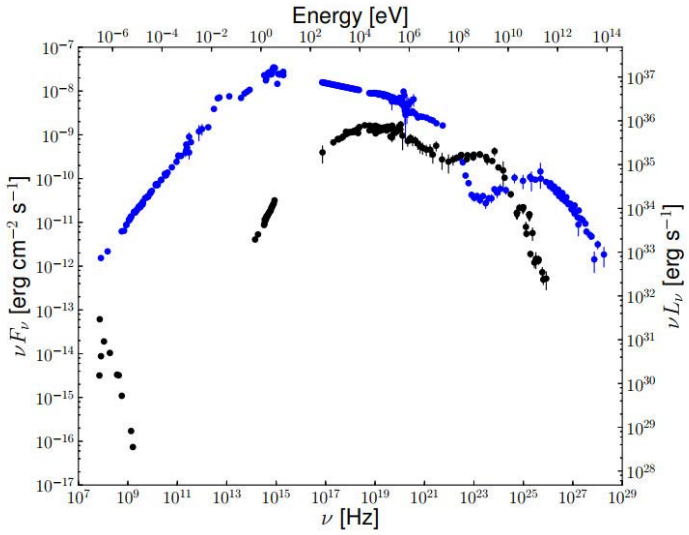

Figure 2.10: Spectral energy distribution of the average emission of the Crab nebula (blue) and the phase averaged emission of the Crab pulsar (black) (Bühler & Blandford, 2014).

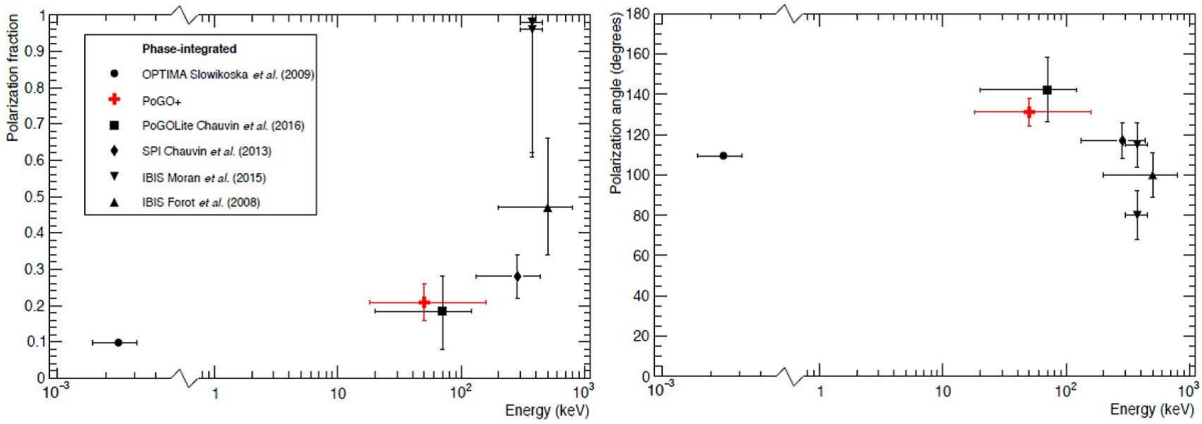

Figure 2.11: Comparison of severak phase-integrated polarimetric studies of the Crab. Data is shown for the degree of polarization (left) and the polarization angle (right) (Chauvin et al., 2017).

Chapter 3

Compton Gamma-ray Polarimetry

3.1 Polarization Modulation

3.1.1 Compton Scattering Cross Section

The polarization states of photons are quantified by the degree of polarization and the polarization angle. In the energy range from approximately 50 keV to several MeV, where the dominant interaction is the Compton scattering, they are determined by measuring the statistical distribution of Compton scattering angle, which is modulated according to the polarization states.

In this section, we derive the intensity of Compton scattered photons when the light source is partially polarized. To evaluate the modulation of the intensity properly, we require careful attention to the coordinate systems for measurement. Figure 3.1 shows a schematic view of Compton scattering of a polarized photon, where the photon polar coordinate system is denoted as (θ_{ph}, ϕ_{ph}). The differential cross section of Compton scattering by a free electron is given by the Klein-Nishina formula (Klein & Nishina, 1929). For unpolarized photons this is given by,

$$f_{UnP}(\theta_{ph}) = \frac{r_0^2}{2}\frac{E^2}{{E_0}^2}\left(\frac{E_0}{E} + \frac{E}{E_0} - \sin^2\theta_{ph}\right), \tag{3.1}$$

where r_0 is the classical electron radius, E_0 and E are the incident and scattered photon energies, respectively. E is given by,

$$E = \frac{E_0}{1 + \frac{E_0}{m_e c^2}(1 - \cos\theta_{ph})}. \tag{3.2}$$

In the case of completely polarized photons, the differential cross section is expressed as (e.g., Lei et al. (1997) and references therein),

$$f_{Pol}(\theta_{ph}, \eta_{ph}) = \frac{r_0^2}{2}\frac{E^2}{{E_0}^2}\left(\frac{E_0}{E} + \frac{E}{E_0} - 2\sin^2\theta_{ph}\cos^2\eta_{ph}\right), \tag{3.3}$$

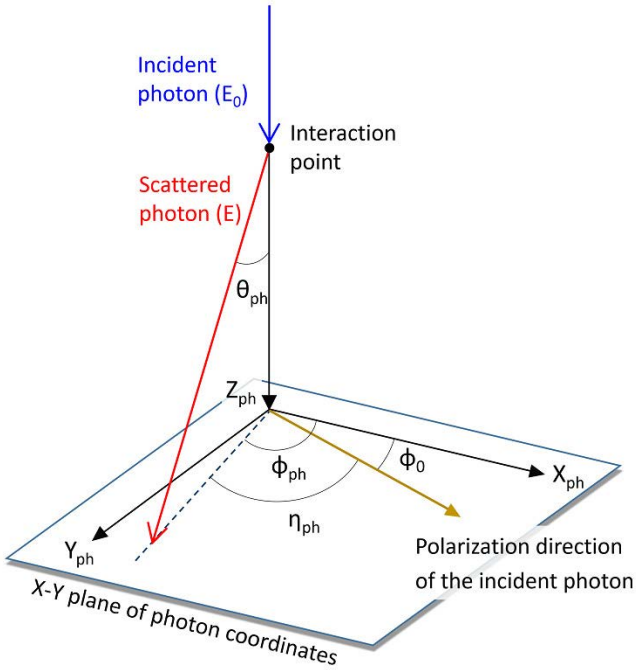

Figure 3.1: Schematic of the Compton scattering of a polarized photon in the photon Cartesian coordinate system (X_{ph}, Y_{ph}, Z_{ph}) and the photon polar coordinate system (θ_{ph}, ϕ_{ph}). The Z_{ph}-axis is defined along the incident direction of the photon, and the X_{ph}-Y_{ph} plane is chosen appropriately. θ_{ph} and ϕ_{ph} is corresponding to the polar and azimuthal scattering angle, respectively. Figure adapted from Komura et al. (2017).

where η_{ph} is the azimuthal angle of the scattered photon relative to the polarization direction of the incident photon. After averaging over η_{ph}, Equation (3.3) is reduced to Equation (3.1).

The degree of polarization Π_0 ($0 < \Pi_0 < 1$) can be defined as,

$$\Pi_0 \equiv \frac{I_{Pol}}{I_0} = \frac{I_{Pol}}{I_{Pol} + I_{UnP}}, \tag{3.4}$$

where I_0 is the intensity of incident photons to be measured, I_{Pol} and I_{UnP} is the polarized and unpolarized component of I_0, respectively. These are constant values at one-time measurement. Then, the intensity of scattered photons can be written as,

$$\begin{aligned} \mathcal{J}(\theta_{ph}, \phi_{ph}) &= I_{Pol} f_{Pol}(\theta_{ph}, \phi_{ph} - \phi_0) + I_{UnP} f_{UnP}(\theta_{ph}) \\ &= I_0 \left[\Pi_0 f_{Pol}(\theta_{ph}, \phi_{ph} - \phi_0) + (1 - \Pi_0) f_{UnP}(\theta_{ph})\right] \\ &= I_0 f_{UnP}(\theta_{ph}) \left[1 + \mu(\theta_{ph}) \Pi_0 \cos\left(2(\phi_{ph} - \phi_0 - \frac{\pi}{2})\right)\right], \end{aligned} \tag{3.5}$$

where ϕ_0 is the polarization angle of incident photon, and $\mu(\theta_{ph})$ is given by,

$$\mu(\theta_{ph}) = \frac{\sin^2\theta_{ph}}{E_0/E + E/E_0 - \sin^2\theta_{ph}}. \tag{3.6}$$

Plots of $\mu(\theta_{ph})$ for various E_0 are shown in Figure 3.2.

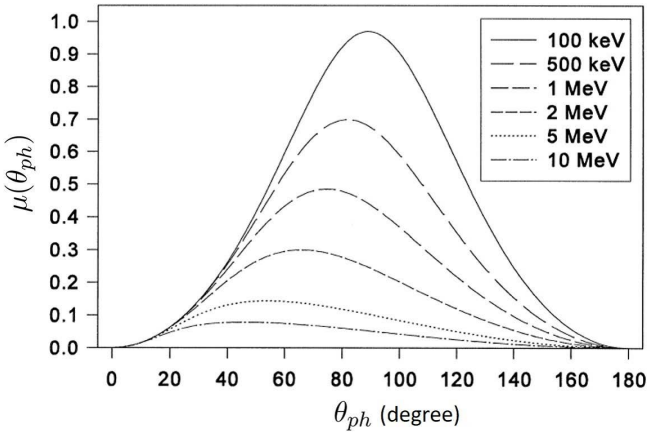

Figure 3.2: Dependences of μ on θ_{ph} for various E_0. Figure adapted from Lei et al. (1997).

3.1.2 On-axis measurement

$\mathcal{J}(\theta_{ph}, \phi_{ph})$ includes Π_0 and ϕ_0 in a simple form, in which Π_0 and ϕ_0 correspond to the amplitude and the phase angle of $\cos(2\phi_{ph})$-curve, respectively. Therefore Π_0 and ϕ_0 are determined by measuring $\mathcal{J}(\theta_{ph}, \phi_{ph})$, which is the basic principle of Compton polarimetry. However, quantities measured by polarimeters are recorded in the detector coordinate system, which is generally different from the photon coordinate system. The three dimensional angular distribution of scattered photons measured in the detector coordinate system is expressed as,

$$\mathcal{D}(\theta_{det}, \phi_{det}) = \hat{\mathcal{J}}(\theta_{det}, \phi_{det})\epsilon(\theta_{det}, \phi_{det}), \tag{3.7}$$

where θ_{det} and ϕ_{det} are the polar and azimuthal angle in the detector coordinates, respectively, $\hat{\mathcal{J}}(\theta_{det}, \phi_{det})$ is $\mathcal{J}(\theta_{ph}, \phi_{ph})$ that is transformed from the photon coordinates, and $\epsilon(\theta_{det}, \phi_{det})$ is the detection efficiency of the detector. Also, the two dimensional angular distribution is given by,

$$\mathcal{N}(\phi_{det}) = \int_{\theta_{min}}^{\theta_{max}} \mathcal{D}(\theta_{det}, \phi_{det}) \sin\theta_{det} \mathrm{d}\theta_{det}. \tag{3.8}$$

In addition, the number of photons (constant value) can be calculated as,

$$N_0 = \int_0^{2\pi} \mathcal{N}(\phi_{det})\mathrm{d}\phi_{det}. \tag{3.9}$$

In the simplest case when the detector coordinates coincide with the photon coordinates (in the case of on-axis incidence), $\mathcal{N}(\phi_{det})$ is explicitly described as,

$$\begin{aligned}\mathcal{N}(\phi_{det}) =& I_0 \int_{\theta_{min}}^{\theta_{max}} f_{UnP}(\theta_{det}) \\ &\times \left[1 + \mu(\theta_{det})\Pi_0 \cos\left(2(\phi_{det} - \phi_0 - \frac{\pi}{2})\right)\right] \epsilon(\theta_{det}, \phi_{det}) \sin\theta_{det}\mathrm{d}\theta_{det}.\end{aligned} \tag{3.10}$$

If we assume $\epsilon(\theta_{det}, \phi_{det})$ is equal to 1, $\mathcal{N}(\phi_{det})$ follows a $\cos(2\phi_{det})$ function as described by

$$\mathcal{N}(\phi_{det}) = \frac{N_0}{2\pi}\left[1 + \overline{\mu}\Pi_0 \cos\left(2(\phi_{det} - \phi_0 - \frac{\pi}{2})\right)\right], \tag{3.11}$$

where,

$$\overline{\mu} = \frac{\int_{\theta_{min}}^{\theta_{max}} f_{UnP}(\theta_{det})\mu(\theta_{det}) \sin\theta_{det}\mathrm{d}\theta_{det}}{\int_{\theta_{min}}^{\theta_{max}} f_{UnP}(\theta_{det}) \sin\theta_{det}\mathrm{d}\theta_{det}}, \tag{3.12}$$

which is plotted in Figure 3.3 as a function of E_0. In this case, the polarization modulation follows a $\cos(2\phi_{det})$-curve with the amplitude of $\overline{\mu}\Pi_0$ and the phase angle of ϕ_0. We can uniquely determine the Π_0 and ϕ_0 by fitting $\mathcal{N}(\phi_{det})$ with the function such as,

$$g(\phi) = C\left[1 + a_{mes} \cos\left(2(\phi - \phi_{mes} - \frac{\pi}{2})\right)\right], \tag{3.13}$$

where C is the constant of proportionality, and a_{mes} and ϕ_{mes} are the amplitude ($0 < a_{mes} < 1$) and the phase angle ($0 < \phi_{mes} < 2\pi$) to be measured, respectively. By comparing Equation (3.11) with Equation (3.13), a_{mes} is assumed to be directly proportional to Π_0. Here we define the factor of proportionality as

$$M \equiv \frac{a_{mes}}{\Pi_0} \quad (0 < M < 1). \tag{3.14}$$

When $\mathcal{N}(\phi_{det})$ is measured with very high precision and there is no statistical and systematic errors described in the following sections, M is equal to $\overline{\mu}$; otherwise M have to be determined by the simulations and measurements. If M is known, Π_0 is calculated by

$$\Pi_0 = \frac{a_{mes}}{M}. \tag{3.15}$$

According to Equation (3.15), polarimeters with large M is more sensitive to the change

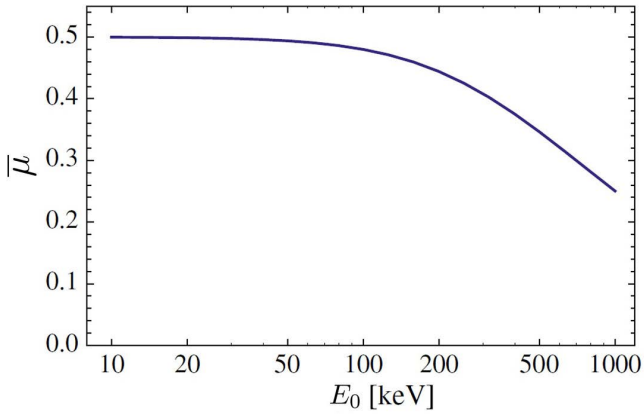

Figure 3.3: Dependence of $\overline{\mu}$ on E_0 assuming that the integration range of θ_{det} is from 0 to π. Figure adapted from Krawczynski et al. (2011).

of Π_0 than those with small M. In this sense, M is often used as the figure of merit of the polarimeter, which is often called as "Modulation Factor".

In most cases, a_{mes} includes the fake modulations due to the statistical and systematic errors as discussed in the following section. Therefore, the measured degree of polarization would be larger than Π_0 when Π_0 is small. The 99% confidence level of the measured degree of polarization for the unpolarized ($\Pi_0 = 0$) incident light is widely called as "Minimum Detectable Polarization (MDP)". By this definition, the MDP is the degree of polarization, which has only a 1% probability of being detected by chance. The MDP is widely used as the polarization sensitivity limit; MDP should be smaller than the degree of polarization of the target astronomical objects. The suppression of the degradation of MDP is a key issue in astronomical polarimetric observations.

3.2 Statistical and Systematic Modulation

3.2.1 Statistical Fluctuation

The chance probability of measuring a particular amplitude a_{mes} and a phase ϕ_{mes}, for the true amplitude and phase are a_0 and ϕ_0, is given by Weisskopf et al. (2010),

$$\mathcal{P}(a_{mes}, \phi_{mes}|a_0, \phi_0) = \frac{N_0 a_{mes}}{4\pi} \exp\left[-\frac{N_0}{4}\left(a_{mes}^2 + {a_0}^2 - 2a_{mes}a_0 \cos 2(\phi_{mes} - \phi_0)\right)\right]. \tag{3.16}$$

Due to the statistical fluctuation, a_{mes} is always positive even if the incident light is unpolarized (Π_0, $a_0 = 0$). Therefore, we need to evaluate the effect of the statistical fluctuation to a_{mes} in any measurement.

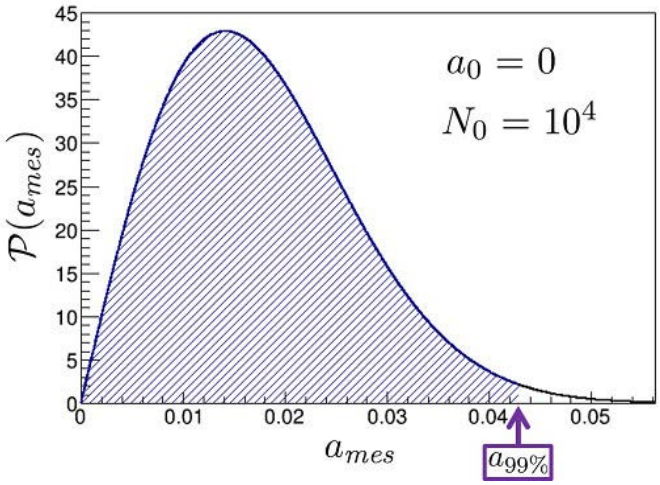

Figure 3.4: Probability distribution of a_{mes} due to the statistical fluctuation, for an unpolarized source ($a_0 = 0$) assuming $N_0 = 10^4$. The region of integration in Equation 3.18 is shown by the hatched area.

For unpolarized case, Equation (3.16) is integrated over ϕ_{mes} analytically. The probability distribution of a_{mes} is therefore,

$$\mathcal{P}(a_{mes}) = \frac{N_0 a_{mes}}{2} \exp\left(-\frac{N_0}{4} a_{mes}^2\right), \tag{3.17}$$

which is plotted in Figure 3.4 assuming $N_0 = 10^4$. Now the 99% confidence interval $a_{99\%}$ is calculated from the following equation:

$$\frac{N_0}{2} \int_0^{a_{99\%}} a_{mes} \exp\left(-\frac{N_0}{4} a_{mes}^2\right) \mathrm{d}a_{mes} \quad = \quad 0.99. \tag{3.18}$$

Then we get $a_{99\%}$ as,

$$a_{99\%} \quad = \quad \frac{4.29}{\sqrt{N_0}}. \tag{3.19}$$

According to the definition provided in the previous section, MDP at 99% confidence level is calculated as the degree of polarization corresponding to $a_{99\%}$:

$$MDP = \frac{4.29}{M\sqrt{N_0}}. \tag{3.20}$$

N_0 is determined by the multiplication of the source flux, the effective area of the polarimeter, and the exposure time. Therefore, a polarimeter has to be designed to have a large effective area and large M to improve the MDP.

3.2.2 Non-uniformity of Detector Response

As shown in Equation (3.10), $\mathcal{N}(\phi_{det})$ does not generally follows a $\cos(2\phi_{det})$ function even in the case of on-axis incidence due to the non-uniformity of the detector response $\epsilon(\theta_{det}, \phi_{det})$. Therefore Π_0 and ϕ_0 cannot be measured by fitting $\mathcal{N}(\phi_{det})$ with Equation (3.13). Although the non-uniformity is canceled out by the detector rotation around its optical axis, which is incompatible with the polarimeters with wide-FoV.

Lei et al. (1997) suggested that the effect of the non-uniformity can be removed by using the azimuthal angle distribution of unpolarized photons with the same energy distribution as the incident photons, $\mathcal{N}_{\Pi=0}(\phi_{det})$, which is mainly obtained by Monte Carlo simulations. The corrected azimuthal angle distribution is generated from

$$\mathcal{N}_{cor}(\phi_{det}) = \frac{\mathcal{N}(\phi_{det})}{\mathcal{N}_{\Pi=0}(\phi_{det})}. \tag{3.21}$$

Lei et al. (1997) said that a good fit to Equation (3.13) has been achieved for $\mathcal{N}_{cor}(\phi_{det})$. Figure 3.5 shows the examples of $\mathcal{N}(\phi_{det})$, $\mathcal{N}_{\Pi=0}(\phi_{det})$, and $\mathcal{N}_{cor}(\phi_{det})$ presented in Lei et al. (1997).

However, $\mathcal{N}_{cor}(\phi_{det})$ does not always follow a $\cos(2\phi_{det})$-curve even in the on-axis case. Using Equation (3.10) and Equation (3.21), $\mathcal{N}_{cor}(\phi_{det})$ is calculated as

$$\mathcal{N}_{cor}(\phi_{det}) = 1 + \overline{\nu}(\phi_{det}) P \cos\left(2(\phi_{det} - \phi_{det,0} - \frac{\pi}{2})\right), \tag{3.22}$$

where

$$\overline{\nu}(\phi_{det}) = \frac{\int_{\theta_{min}}^{\theta_{max}} f_{UnP}(\theta_{det}) \mu(\theta_{det}) \epsilon(\theta_{det}, \phi_{det}) \sin\theta_{det} \mathrm{d}\theta_{det}}{\int_{\theta_{min}}^{\theta_{max}} f_{UnP}(\theta_{det}) \epsilon(\theta_{det}, \phi_{det}) \sin\theta_{det} \mathrm{d}\theta_{det}}. \tag{3.23}$$

Therefore, the amplitude of $\cos(2\phi_{det})$ is not strictly constant, and $\mathcal{N}_{cor}(\phi_{det})$ cannot be fitted by Equation (3.13). When the detector has a high symmetry, we can assume that $\epsilon(\theta_{det}, \phi_{det}) = \epsilon_0(\theta_{det})\epsilon_1(\phi_{det})$ for the appropriate integration interval $[\theta_{min}, \theta_{max}]$. In this case, $\overline{\nu}(\phi_{det})$ is constant and $\mathcal{N}_{cor}(\phi_{det})$ depend only on $\cos(2\phi_{det})$. Therefore, we need to check whether the detector has a high symmetry enough to apply this analysis.

In the correction of the detector response, the reliability of the Monte Carlo simulations to obtain $\mathcal{N}_{\Pi=0}(\phi_{det})$ is critical to suppress the degradation of MDP, where fake modulations are generated in the process of Equation (3.21) due to the difference between simulated $\mathcal{N}_{\Pi=0}(\phi_{det})$ and its true distribution. In space observations, particularly, we have to check the reliability of the simulation by comparing the simulated $\mathcal{N}_{\Pi=0}(\phi_{det})$ and measured one. The most proper way is measuring the $\mathcal{N}_{\Pi=0}(\phi_{det})$ and the energy distribution of the unpolarized background coming from the same direction as the source signal. Therefore, for the wide-FoV polarimetery, it is essential to have the capability of imaging spectroscopy based on the reliable PSF.

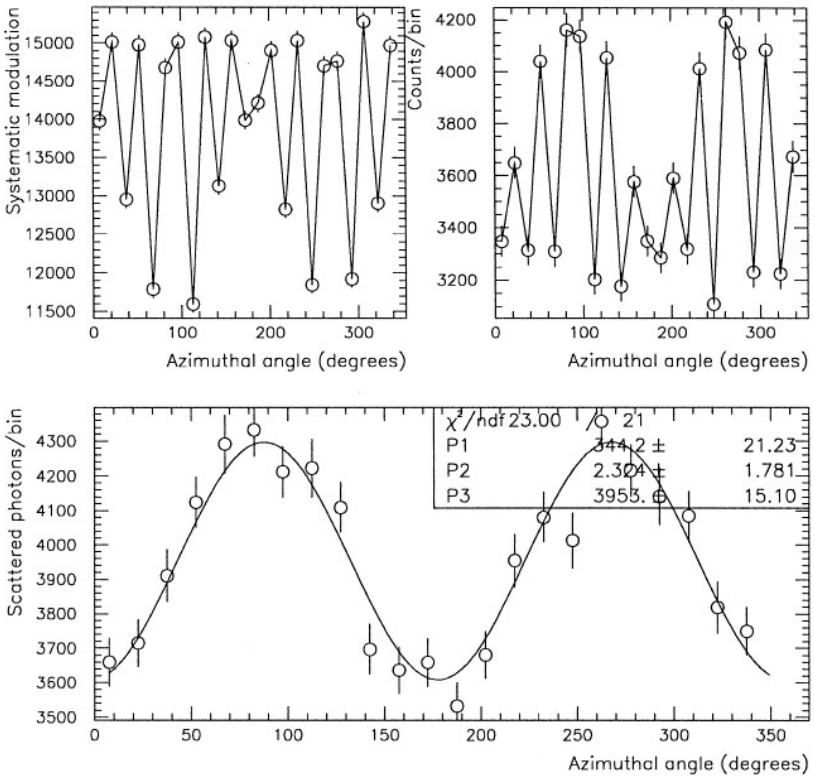

Figure 3.5: Azimuthal angle distributions of scattered photons calculated by the Monte Carlo simulation of COMPTEL; top left) unpolarized incident photons, $\mathcal{N}_{\Pi=0}(\phi_{det})$; top right) completely polarized photons, $\mathcal{N}(\phi_{det})$; bottom) corrected distribution, $\mathcal{N}_{cor}(\phi_{det})$ and its best fit with $\cos(2\phi_{det})$ function. The incident photons are on-axis with energy of 1 MeV (Lei et al., 1997).

3.2.3 Off-axis Incidence

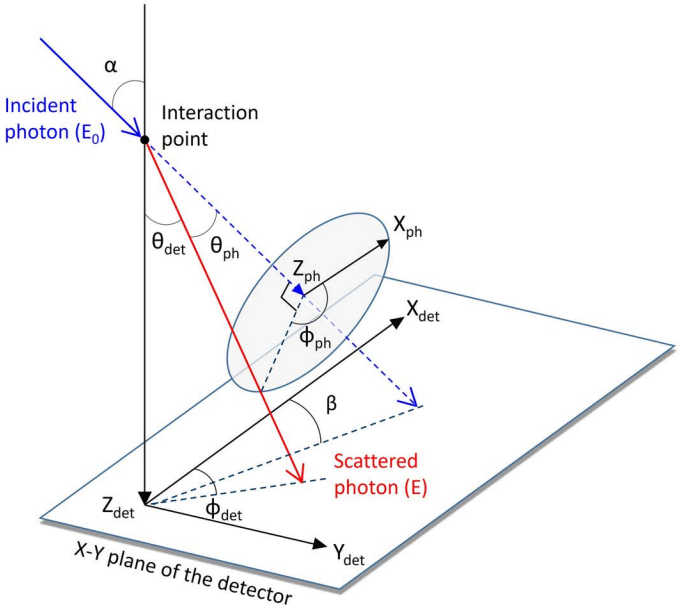

Figure 3.6: Schematic of Compton scattering in the case of off-axis incidence in the detector Cartesian coordinate system (X_{det}, Y_{det}, Z_{det}) and polar coordinate system (θ_{det}, ϕ_{det}). The Z_{det}-axis is defined along the optical axis of the detector, and the X_{det}-Y_{det} plane is chosen appropriately. The travel direction of incident photon is described as (α, β). The remaining symbols have the same meaning as in Figure 3.1. Figure adapted from Komura et al. (2017).

As shown in Figure 3.6, when the incident photon has an incident angle of α relative to the optical axis of the detector (in the case of off-axis incidence), the detector coordinates are not coincident with the photon coordinates. Therefore, $\mathcal{N}(\phi_{det})$ described in Equation (3.8) have to be transformed to this coordinates using Equation (3.7), and then transformed $\mathcal{N}(\phi_{det})$ follows a $\cos(2\phi_{det})$ function. Then, nontransformed $\mathcal{N}(\phi_{det})$ possibly cause fake modulations even for unpolarized photons (Lei et al., 1997; Muleri, 2014).

If the polarimeter measures θ_{det} in addition to ϕ_{det} event by event, we can move to the photon coordinate system photon by photon, where $\cos(2\phi)$-curve is recovered (Lei et al., 1997). The displacement of the scattered photon in the photon coordinate system from the detector coordinate system is calculated by the following transformation

matrix (Lei et al., 1997; Muleri, 2014):

$$\begin{cases} x_{ph} = (x_{det}\cos\beta + y_{det}\sin\beta)\cos\alpha - z_{det}\sin\alpha, \\ y_{ph} = -x_{det}\sin\beta + y_{det}\cos\beta, \\ z_{ph} = (x_{det}\cos\beta + y_{det}\sin\beta)\sin\alpha - z_{det}\cos\alpha, \end{cases} \tag{3.24}$$

where (x_{det}, y_{det}, z_{det}) is the displacement of the scattered photon in the detector coordinate system and (α, β) are the polar and azimuthal angle of incident photon, respectively.

Now, we calculate the angular distribution of the scattered photon $\hat{\mathcal{D}}(\theta_{ph}, \phi_{ph})$. Then, the integrated azimuthal angle distribution $\hat{\mathcal{N}}(\phi_{ph})$ is expressed as,

$$\begin{aligned} \hat{\mathcal{N}}(\phi_{det}) &= \int_{\theta_{min}}^{\theta_{max}} \hat{\mathcal{D}}(\theta_{ph}, \phi_{ph}) \sin\theta_{ph} \mathrm{d}\theta_{ph} \\ &= I_0 \int_{\theta_{min}}^{\theta_{max}} f_{UnP}(\theta_{ph}) \\ &\quad \times \left[1 + \mu(\theta_{ph}) P \cos\left(2(\phi_{ph} - \phi_{ph,0} - \frac{\pi}{2})\right)\right] \hat{\epsilon}(\theta_{ph}, \phi_{ph}) \sin\theta_{ph} \mathrm{d}\theta_{ph}. \end{aligned} \tag{3.25}$$

Although $\mathcal{N}(\phi_{ph})$ includes $\hat{\epsilon}(\theta_{ph}, \phi_{ph})$, the same analysis in Section 3.2.2 removes the non-uniformity and recovers the $\cos(2\phi_{ph})$-curve. Figure 3.7 shows the example. Lei et al. (1997) said that a polarization modulation is visible only after the removal of the modulations due to the off-axis incidence and the non-uniformity of the detector response and can be fitted by Equation (3.13).

Unfortunately, the most of Compton polarimeters do not measure θ_{det}. Therefore, it is difficult to perform the coordinate transformation and to cancel out the effect of off-axis incidence and detector response even if reliable $\mathcal{N}_{\Pi=0}(\phi_{det})$ is obtained in some way. Several authors have reported that M of their developed GRB polarimeters, which is discussed in Chapter 4, decreased by approximately 40% for an incident angle of 60° in Monte Carlo simulations (Xiong et al., 2009; McConnell et al., 2009; Gunji et al., 2014) due to the lack of θ_{det}. Figure 3.8 shows the dependence of the simulated M on incident angles for a certain model of POLAR detector. Due to the degradation of M, MDP is increased by more than 1.7 times according to Equation (3.20) when the incident angle is larger than 60°, where the solid angle corresponds to the half of the 2Π-steradian-FoV. As a result, the measurement of θ_{det} is essential for the wide-FoV polarimetry in principle.

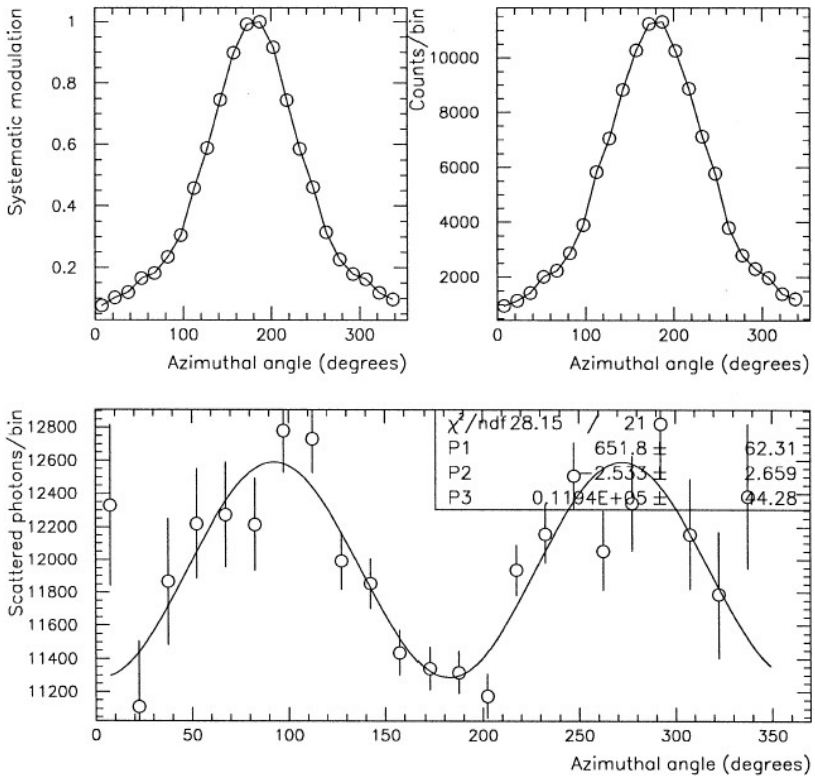

Figure 3.7: An example of the removal of off-axis incidence effect from a polarized dataset to reveal the underlying polarimetric distribution. The detector configuration used in the simulation is the COMPTEL. Incident photons are 15° off-axis. : top left) unpolarized incident photons, $\hat{\mathcal{N}}_{\Pi=0}(\phi_{ph})$; top right) completely polarized photons, $\hat{\mathcal{N}}(\phi_{ph})$; bottom) corrected distribution, $\hat{\mathcal{N}}_{cor}(\phi_{ph})$ and its best fit with $\cos(2\phi_{det})$ function (Lei et al., 1997).

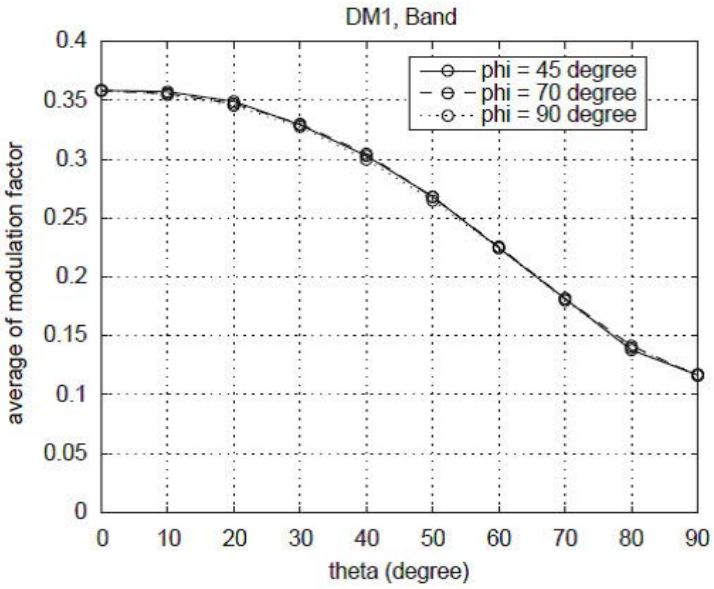

Figure 3.8: The simulated modulation factors of a certain model of POLAR detector. They varies with incident angle theta but remains almost constant with polarization angle phi (Xiong et al., 2009).

3.3 Background Noise in Space

In astronomical observations of hard X-ray and MeV gamma-ray, the background noise is always the dominant signal. Cosmic rays interact with the instruments and satellites and produce large amount of gamma rays by the nuclear reaction and Bremsstrahlung. Thus, MeV gamma-rays generated in the satellite are dominant background source. The shielding of MeV gamma-rays is also difficult due to their high transmittance. The large fake modulations in $\mathcal{N}(\phi_{det})$ are usually produced by these various types of background with anisotropic directional distributions.

In order to minimize the background effect, its distribution has to be measured by an on-source/off-source observation strategy or derived by detailed modeling although simulated background distribution contains large uncertainty in most cases. Any residual of background in $\mathcal{N}(\phi_{det})$ would lead to the degradation of M and introduce fake modulations after the correction and transformation of Equations (3.21) and (3.24). These fake modulations reduce the MDP systematically.

Even if background is well understood and properly removed, it reduces the MDP statistically. Weisskopf et al. (2010) derived the MDP calculation formula assuming a contribution from a steady background to $\mathcal{N}(\phi_{det})$,

$$\mathrm{MDP} = \frac{4.29}{MR_S}\sqrt{\frac{R_S + R_B}{T_{obs}}}, \tag{3.26}$$

where T_{obs} is the exposure time of the observation, R_S and R_B are the count rate of the signal photons and backgrounds, respectively. R_S and R_B correspond to $F_S A$ and $I_B \Delta\Omega A$, respectively, using the signal photon flux F_S and the background intensity I_B. A and $\Delta\Omega$ are the effective area and the PSF of the detector, respectively. In most cases, the MDP degrades in proportion to the square root of the PSF ($\mathrm{MDP} \propto \sqrt{\Delta\Omega}/(M\sqrt{AT_{obs}})$) where the background is dominant ($R_B \gg R_S$). Therefore, a sharp PSF is required to suppress the statistical background contribution, with a large effective area, a large M, and long exposure time, in order to obtain a small MDP as same as mentioned in Section 3.2.1.

Chapter 4

Astronomical Compton Polarimeters

As discussed in Chapter 3, the polarization of emission source is simply obtained by the measurement of $\mathcal{N}(\phi_{det})$. There were several challenges to measure $\mathcal{N}(\phi_{det})$ of celestial objects by using sub-MeV and MeV gamma-ray instruments, such as *CGRO*/COMPTEL, *RHESSI*, *INTEGRAL*/SPI and IBIS, and *AstroSat*/CZTI. However, high quality measurements of the polarization were difficult due to their low modulation factor and a large uncertainty of the systematic modulations. Recently, several types of dedicated Compton polarimeters have been proposed depending on their target celestial objects. In this section, I briefly summarize these astronomical gamma-ray instruments where the principle of Compton polarimetry is utilized.

4.1 Non-dedicated Instruments

COMPTEL

COMPTEL is a unique Compton cameras used in space, which consists of forward liquid-organic and backward NaI(Tl) scintillators as shown in Figure 4.1. The energy range of COMPTEL is 0.8–30 MeV, and the effective is 20–50 cm^2, which is reduced to the half after the event selections are applied to the data. A Compton camera measures the momentum of scattered photon in Compton scattering processes, and reconstructs the direction as like the event circle. Therefore, COMPTEL were able to measure the three-dimensional direction of the scattered gamma-ray and the polarization states of incident photon. The simulation study of COMPTEL (Lei et al., 1996) shows that COMPTEL has very small modulation factor $\sim$0.01 as shown in Figure 4.2, due to the geometrical configuration where the forward scattering events were dominant. You note that these modulation factors are obtained using the analysis of the cancellation of the systematic modulations shown in Equation (3.21) and (3.24). In addition to the small modulation factor, the huge background in space was not sufficiently removed by the Compton camera imaging (Weidenspointner et al., 2001; Schönfelder, 2004). Consequently, COMPTEL did not measure any statistically significant polarizations.

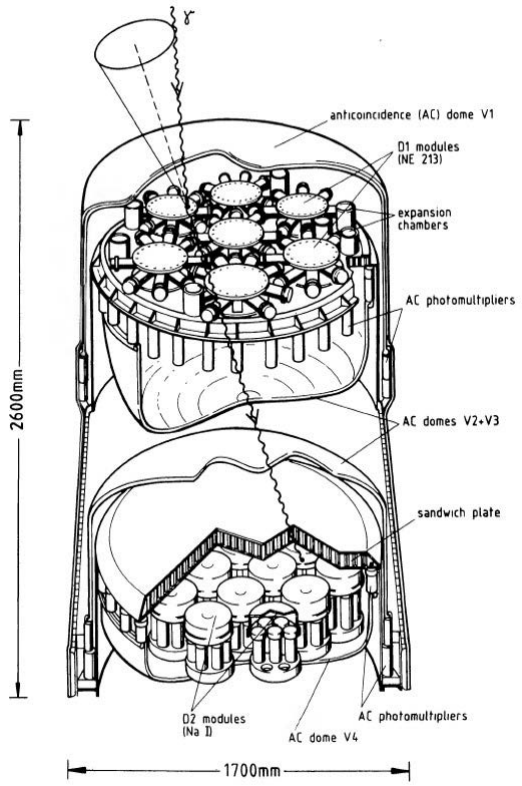

Figure 4.1: Schematic view of the COMPTEL instrument (Schoenfelder et al., 1993).

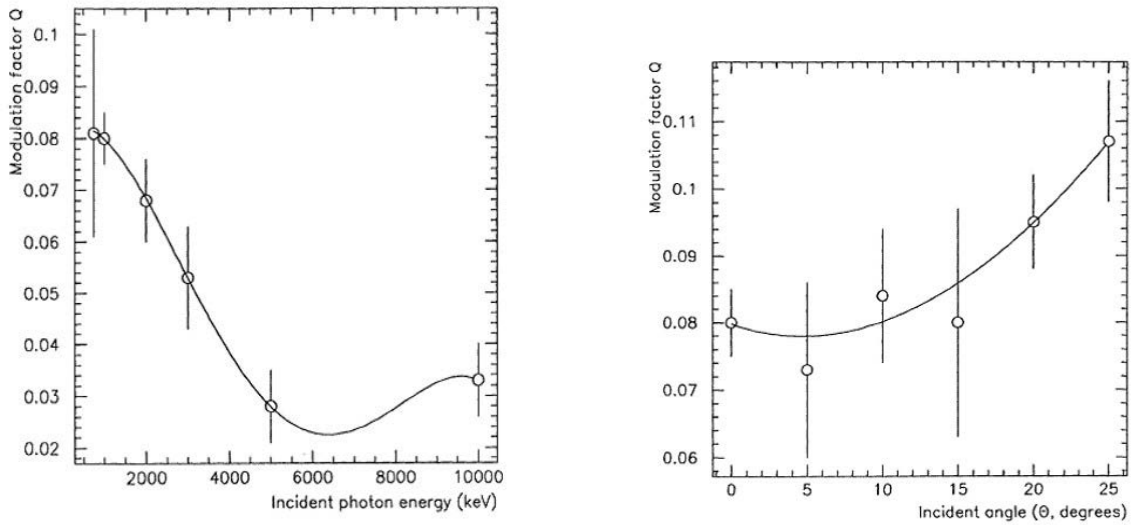

Figure 4.2: (left) Modulation factor of COMPTEL as a function of incident photon energy. (right) Modulation factor of COMPTEL as a function of incident angle. The energy of the incident photons is 1 MeV. Figures from Lei et al. (1996).

RHESSI

The Reuven Ramaty High Energy Solar Spectroscopic Imager (*RHESSI*) is a solar gamma-ray telescope designed to make imaging and spectroscopic observations of solar flares at energies between 3 keV and 20 MeV (Smith et al., 2002) using a coded mask. *RHESSI* has an array of nine coaxial Germanium (Ge) detectors, as shown in Figure 4.3, which are unshielded, and therefore GRBs are frequently observed. Although there is no positional information available inside a Ge detector, these Ge detectors can be used as a Compton polarimeter in the 0.15–2 MeV range since $\mathcal{N}_{mes}(\phi_{det})$ is constructed from the coincidence events that scatter between detectors (McConnell et al., 2002). *RHESSI* rotates at a rate of $\sim$ 15 rotations per minute, which help to reduce the geometrical non-uniformity response when the GRB placed near on-site. Coburn & Boggs (2003) obtained $\mathcal{N}_{mes}(\phi_{det})$ for extremely bright GRB (GRB 021206) using the *RHESSI* data (see Figure 4.4) and reported the high degree of polarization of $80 \pm 20\%$ with a significance of 5.7σ, even though subsequent studies of the data done by other authors did not confirm the initial result (Wigger et al., 2004; Rutledge & Fox, 2004). Thus, these results are still conflict.

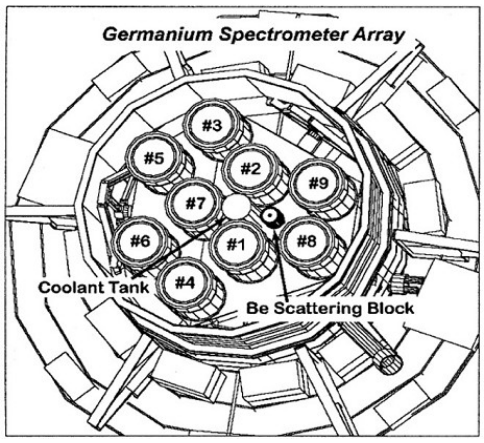

Figure 4.3: The *RHESSI* spectrometer array consists of nine Germanium detectors. Each Ge detector is 7.1 cm in diameter and 8.5 cm long (McConnell et al., 2004).

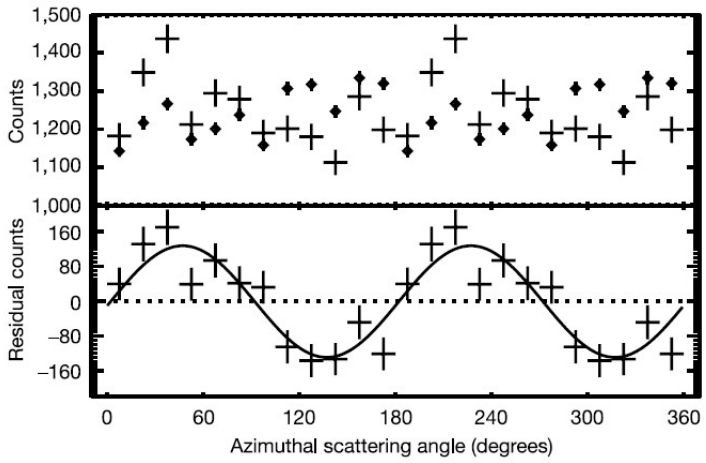

Figure 4.4: *RHESSI* observation of GRB 021206. The top panel shows both the measured scattered angle distribution (crosses) and the simulated scatter angle distribution (diamonds) for unpolarized radiation. The bottom panel shows the difference between the two distributions and the best-fit modulation curve, corresponding to a linear polarization of $80 \pm 20\%$ (Coburn & Boggs, 2003).

INTEGRAL

The International Gamma-Ray Astrophysics Laboratory (*INTEGRAL*; Winkler et al. 2003) contains two coded-mask detectors, Spectrometer on *INTEGRAL* (SPI; Vedrenne et al. 2003; Roques et al. 2003) and Imager on Board the INTEGRAL Satellite (IBIS; Ubertini et al. 2003), which are designed to spectroscopy and imaging of gamma-rays, respectively. The SPI has 19 large hexagonal Ge-detectors covering energies from 20 keV to 8 MeV as shown on the left in Figure 4.5. Although not optimized for polarization measurements, the SPI is sensitive to polarization for the same reasons as *RHESSI*. The IBIS has two layers of pixellated detector planes separated by $\sim$ 10 cm as shown on the right in Figure 4.5. The top layer detector plane is made of 16384 square CdTe detectors ($4\times4\times2\mathrm{mm}^2$), and the bottom detector layer consists of 4096 square CsI detectors ($8.7\times8.7\times30\mathrm{mm}^2$). These detectors can be combined to work as a Compton telescope, and therefore IBIS is also sensitive to the polarization for the same reasons as COMPTEL.

The simulation studies show that SPI and IBIS have the moderate modulation factors for on-axis measurement as shown in Figure 4.6 (Kalemci et al., 2007). The *INTEGRAL* group reported the polarization of the Crab nebula (Dean et al., 2008; Forot et al., 2008) and Cygnus X-1 (Laurent et al., 2011), however, these results are plagued by large uncertainties. The major problem of the *INTEGRAL* polarimetry is the lack of proper ground calibration of its modulation factors and a large uncertainty of the systematic caused by the complicated geometrical response due to their coded-masks.

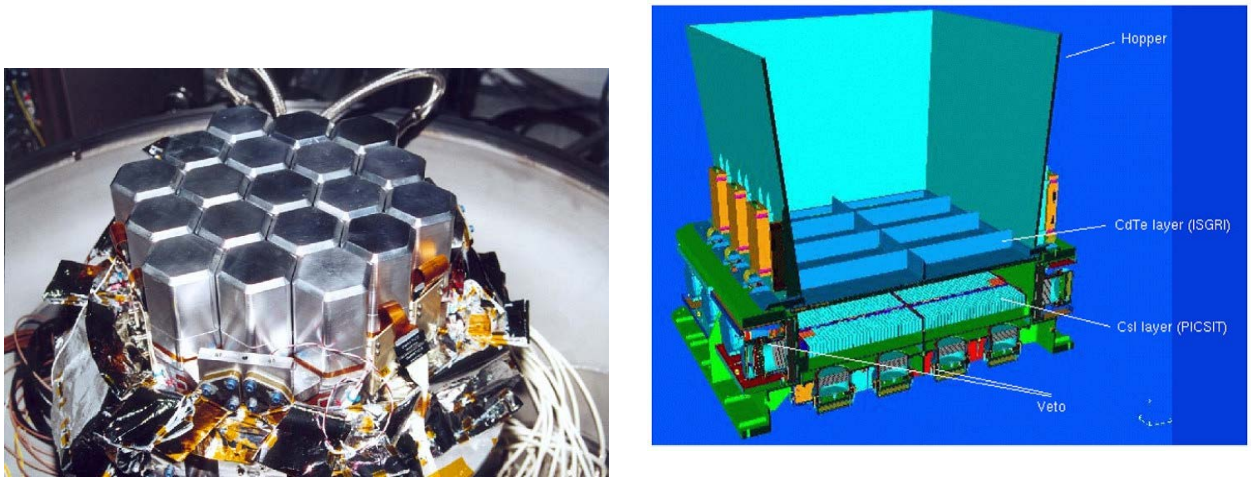

Figure 4.5: Schematic view of the SPI (left) and IBIS (right).

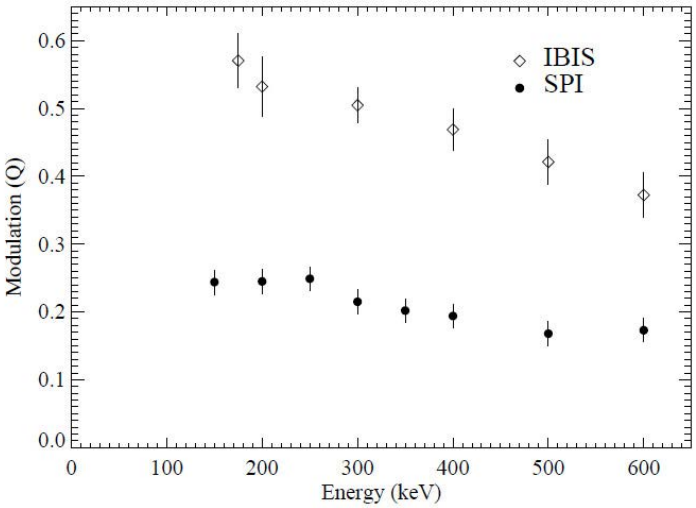

Figure 4.6: The modulation factors for on-axis photons as a function of energy for both SPI and IBIS Compton mode (Kalemci et al., 2007).

CZTI

The Cadmium-Zinc-Telluride Imager (CZTI) is a coded aperture telescope that is originally designed to the imaging and spectroscopy of bright X-ray sources in the 20–150 keV band. The CZTI is launched on-board *AstroSat* satellite on September 28, 2015. As shown in Figure 4.7, the whole CZTI instrument consists of an array of 64 pixelated CZT detector modules, and each detector module is of size 39.06× 39.06 mm^2 and has a 16×16 pixel array. The collimator and masks are designed to be effective up to 100 keV, and therefore CZTI acts as an GRB polarimeter with wide-FoV in the 100–300 keV band. They reported that a distinct modulation pattern is shown in the azimuthal angle distribution for GRB 151006A (Rao et al., 2016) as shown in Figure 4.8, where we clearly see a large uncertainties.

Figure 4.7: Photographs of CZT Imager: (left) Fully assembled CZTI payload. (right) CZTI detector plane with 64 detector modules arranged to four identical quadrants. Figures from Vadawale et al. (2016).

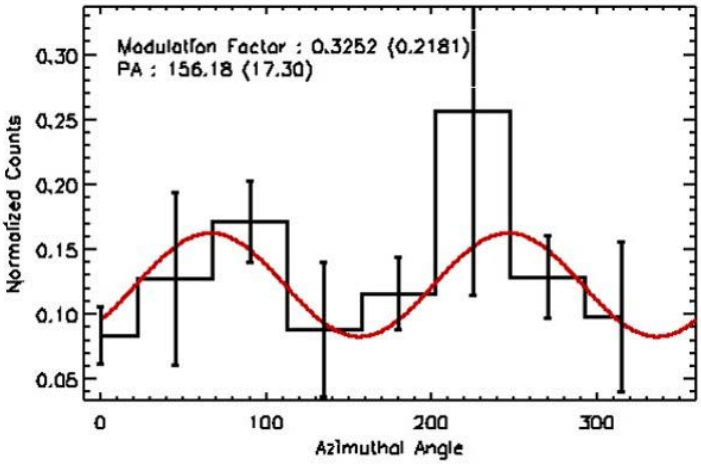

Figure 4.8: CZTI observation of GRB 151006A. The red solid line is the $\cos(2\phi)$ fit to the azimuthal scattering distribution. The degree of polarization is obtained as $\sim$0.32 with a detection significance of 1.5σ. The fitted polarization angle is $\sim$156° in the CZTI plane (Rao et al., 2016).

4.2 Pointing Polarimeter

A pointing observation is a simple solution to constrain the direction of incident photons. Thanks to their narrow FoV, we do not need to consider the systematic modulations due to the off-axis incidence. In addition, the non-uniformity of the detector is canceled out when the detector rotates around its optical axis. Furthermore, on-source/off-source observation strategy allows an estimation of the background without relying on the simulation, and enables the subtraction of possible background modulation as mentioned in Section 3.3.

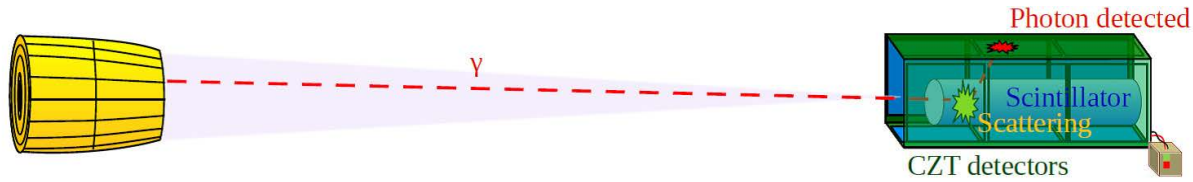

Figure 4.9: Schematic view of the X-Calibur (Kislat et al., 2017).

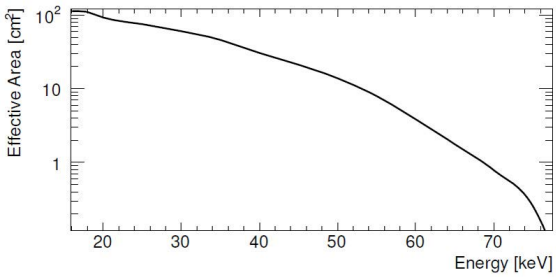

Figure 4.10: Effective area as function of the photon energy of the X-ray mirror (Guo, 2014).

X-Calibur (Beilicke et al., 2014) is a balloon-borne Compton polarimeter combined with the InFOCuS grazing incidence X-ray mirror (Ogasaka et al., 2005) for the energy range from 20 to 60 keV. X-rays from a celestial source are focused with the X-ray mirror and scattered onto a 13 mm-diameter plastic scintillator rod as shown in Figure 4.9. The scattered X-ray is recorded by an array of Cadmium-Zinc-Telluride (CZT) detectors surrounding the scattering rod. The focal length of the mirror is 8 m and the field of view is 8 arcmin at 20 keV. In addition to the background suppression by the active and passive shielding around the detector, the X-ray mirror collects only photons coming from the source direction to a small focusing spot area and dramatically improve the statistical accuracy. The limit of the energy in focusing by reflection is order of 10 keV, and the effective area of the mirror falls suddenly in the higher energy as shown in Figure 4.10. The X-Calibur group reported a high modulation factor of 0.5–0.7, which is close to limit set determined by geometrical configuration of Compton polarimeters. In addition, they control the systematic modulations through the rotation of detector at 2 rotations per

minute. The calculated MDPs for bright celestial sources, such as Crab nebula, Sco X-1, and Cyg X-1, are ∼10% for several hours observations in balloon experiment. Although a one-day balloon-borne experiment was carried out in 2014, no cosmic X-ray sources were observed due to a failure of the pointing system. They have upgraded X-Calibur and plan to perform a long-duration balloon flight for the 2018 or 2019 season (Kislat et al., 2017).

PoGO+ (Chauvin et al., 2016a), a successor to PoGOLite Pathfinder (Chauvin et al., 2016b), is a balloon-born Compton polarimeter combined with a fine collimator in the energy range 20–160 keV. The aim of PoGO+ is to achieve MDP 10% for Crab observations during a single balloon flight. A schematic view of the PoGO+ polarimeter is shown in Figure 4.11. The PoGO+ uses an array of 61 plastic scintillator rods, each with hexagonal cross-section (12 cm long, side length of 2.8 cm). The polarization events are characterized by a Compton scatter in one rod followed by a secondary Compton scatter or a photoelectric absorption in another rod. A hexagonal cross-section copper tube collimator (0.5 mm wall thickness, 67.5 cm length) is mounted in front of each scintillator rod. The FoV of the instrument is limited to 2×2°. As shown in Figure 4.11, the aperture background is reduced by a collimator system, the atmospheric photon or charged particle background are reduced by the BGO anti-coincidence system, and the atmospheric neutron background is reduced by the shield of polyethylene. In addition, the polarimeter assembly is rotated around the viewing axis at a rate of 1° per second, which allows to average the variations in detection efficiency between scintillator units. The simulated energy dependence of the effective area and the modulation factors are shown in Figure 4.12 The MDPs for the Crab and Cygnus X-1 (hard state) are calculated as about ∼10% after a 5 day flight. Very recently, PoGO+ group reported the measurement of the phase-integrated Crab polarization above 4σ in 5-days balloon observation (Chauvin et al., 2017).

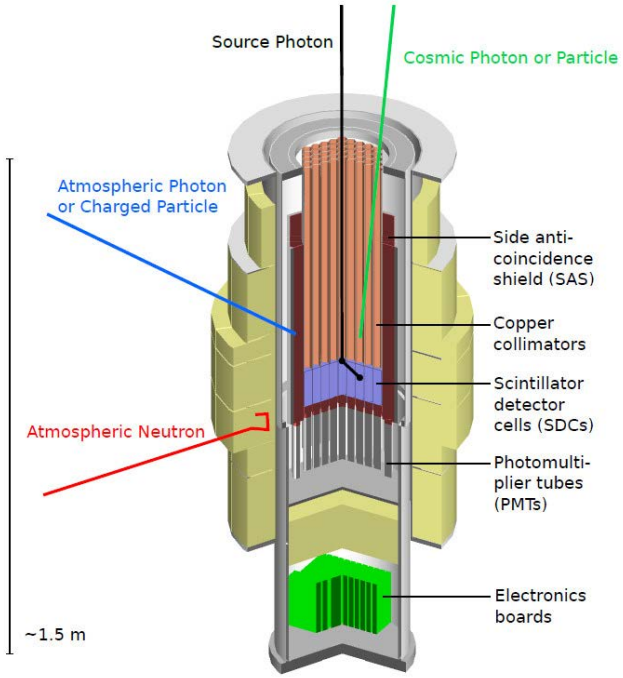

Figure 4.11: Schematic view of the PoGO+ polarimeter (Chauvin et al., 2017).

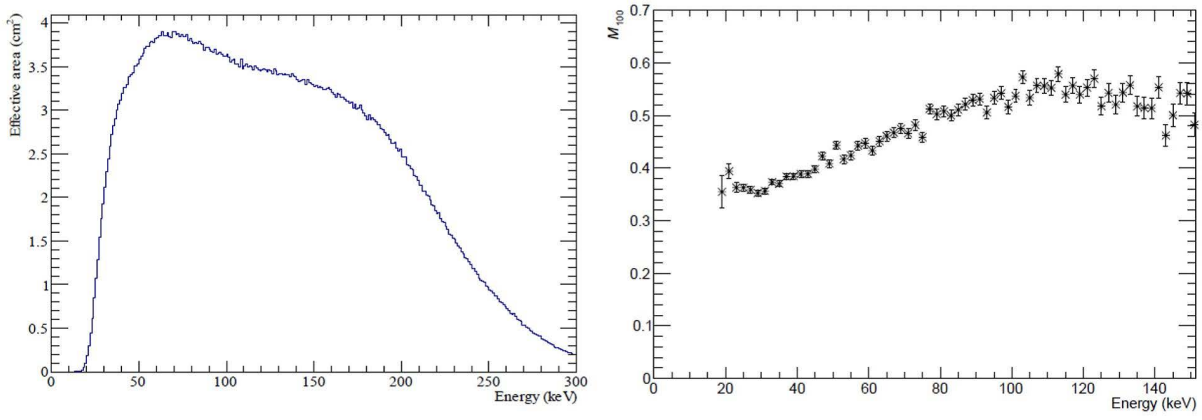

Figure 4.12: (Left) Effective area of PoGO+. (Right) Simulated modulation factor as a function of energy. Figures from Chauvin et al. (2017).

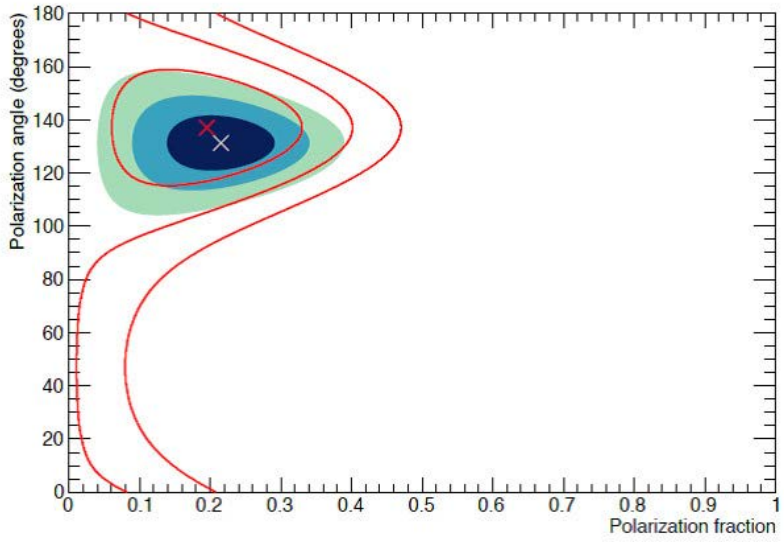

Figure 4.13: Contour plots for the Crab observation. Gaussian 1, 2 and 3σ probability contours for phase-integrated (shaded area) and off-pulse Crab observations (red lines) (Chauvin et al., 2017).

4.3 GRB Polarimeter

To observe bright GRBs, several Compton polarimeters with wide FoV and moderate detection area have been developed. The GAmma-ray Polarimeter (GAP) is the first flight instruments dedicated to GRB polarization measurements in the energy range 70–300 keV (Yonetoku et al., 2011a). The GAP experiment was flown as additional part of a Japanese solar power sail demonstration mission known as IKAROS (Interplanetary Kite-craft Accelerated by the Radiation Of the Sun) and performed several GRB observations in the deep space. As shown in Figure 4.14, it consists of one large plastic scintillator surrounded by an array of 12 CsI(Tl) scintillators. The location of the hit CsI detector gives $\mathcal{N}(\phi_{det})$, however $\mathcal{D}(\theta_{det}, \phi_{det})$ cannot be measured. The effective area and the modulation factor at 100 keV were 30 cm^2 and $\sim$0.3, respectively. In contrast to the *RHESSI*, GAP has a high axial symmetry and a high gain uniformity to suppress the systematic modulations due to background photons. The GAP group carried out the ground-based calibration using polarized X-ray beam and confirmed that the simulated $\mathcal{N}(\phi_{det})$ is agree well with the measured one in the case of on-axis incident. During two years observations, the GAP group reported three GRB polarization detections as shown in Table 2.2 with significance of $\sim 3\sigma$. To determine the measured polarization states, they simulated the model function of $\mathcal{N}(\phi_{det})$ with step resolutions of 5% for polarization degrees and 5° for polarization angles with GEANT4 Monte Carlo simulations. The measured $\mathcal{N}(\phi_{det})$, which does not follow $\cos(2\phi_{det})$, have been fitted using a least-squares method to the modeled modulation curves directly. The right of Figure 4.15 shows the measured and best fitted modulation curves, which represents the change of polarization angle during the interval of prompt emission of GRB 100826A, which was located at 20.0° off-axis from the center of the GAP field of view. We note that GRB 100826A was very bright burst with the energy fluence of $\sim 3.0 \times 10^{-4}$ erg cm^{-2}, which happen $\sim$1 events per year in the whole sky. Even in this case, the signal-to-noise ratio estimated from Figure 4.15 is not large, $\sim$1 on Interval-1 and $\sim$0.3 on Interval-2.

There has been proposals of various GRB polarimeters with wide-FoV and simple geometries consisting of an array of pixelated plastic scintillators so far (Bloser et al., 2009; Yonetoku et al., 2011a; Gunji et al., 2014; Yatsu et al., 2014). In particular, POLAR has recently launched on-board the Chinese space laboratory Tiangong-2 in 2016. The POLAR detector consists of an array of 5 $\times$ 5 modules, each of which includes 8 $\times$ 8 plastic scintillator bars as shown in Figure 4.16. Both the Compton scattering interaction of the photon and its secondary interaction, photoabsorption, are measured using the scintillator bars. The POLAR detector aims to measure the polarization of the prompt emission from GRBs in the 50–500 keV energy range with the wide FoV of about π str. It has been estimated that MDPs for bright GRB with a 10^{-5} erg cm^2 fluence are about 10% and therefore POLAR would measure the polarization of 10 GRBs with 10% polarization during a one-year observation at least. POLAR group reported that about 50 GRBs are detected within 6 months, and the polarization analysis of those GRBs are underway

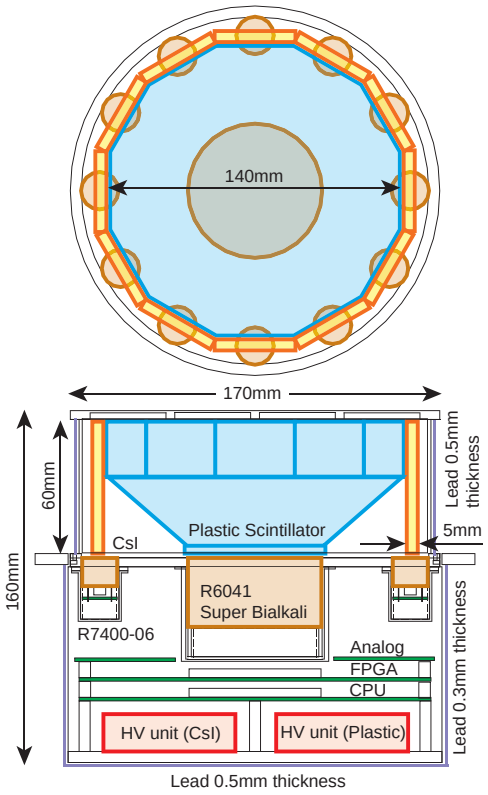

Figure 4.14: Schematic view of the GAP detector (Yonetoku et al., 2011a).

(http://polar.psi.ch/pub/).

These wide-FoV GRB polarimeters have four problems that should be noted. Due to the lack of imaging capabilities, (1) they are not able to confirm the reliability of the simulation in space by measuring the unpolarized background as mentioned in Section 3.2.2; (2) the MDP is statistically degraded by a huge background contribution coming from all directions as mentioned in Section 3.3; (3) they essentially have to rely on other satellites to know the direction of the target sources, which would reduce the number of GRBs to be measured. In addition, due to the lack of measurement of θ_{det}, (4) they are not able to correct the off-axis incident effect, and the MDP is also degraded by increasing the incident angle as mentioned in Section 3.2.3.

The bright GRBs with the fluence of larger than 10^{-5} erg cm^{-2} happen $\sim$50 events per year in the whole sky. Therefore, the GRBs located in the 2π-steradian-FoV, which should be observed by other satellites simultaneously, are reduced to $\sim$10 events per year. The number of GRBs which have a degree of polarization larger than the degraded MDP, is further reduced to several events per year, which is fewer than are necessary for the statistical analysis of GRB polarizations as mentioned in Section 2.2.1.

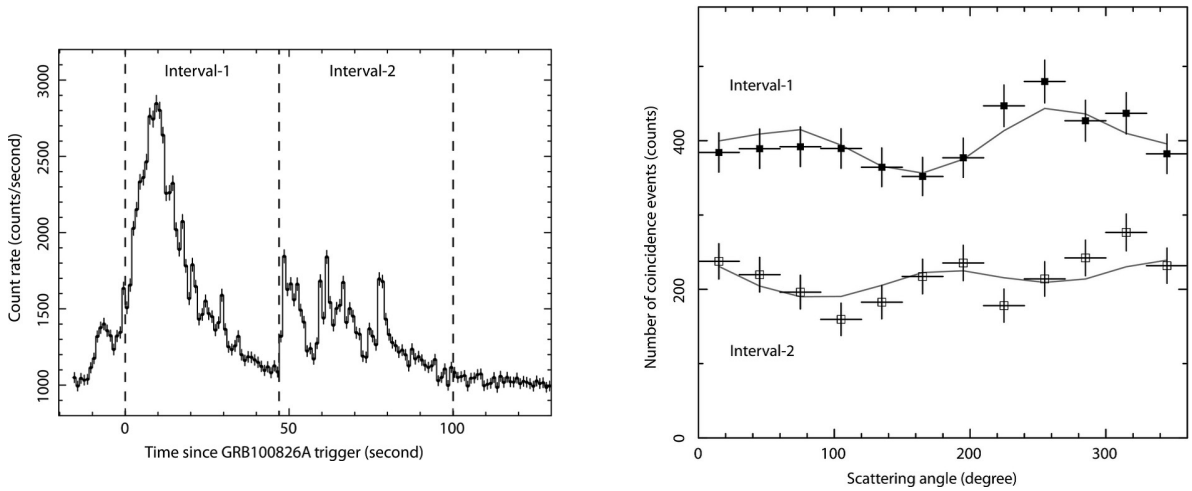

Figure 4.15: (Left) Light curve of the prompt gamma-ray emission of GRB100826A detected by the GAP. The GAP group divided the data into Interval-1 and -2 for the polarization analysis. (Right) Number of coincidence gamma-ray photons against the scattering angle of GRB 100826A measured by the GAP in 70–300 keV band. Black filled and open squares are the angular distributions of Compton scattered gamma-rays of Interval-1 and -2, respectively. The gray solid lines are the best-fit models calculated by the Geant4 Monte Carlo simulations (Yonetoku et al., 2011b).

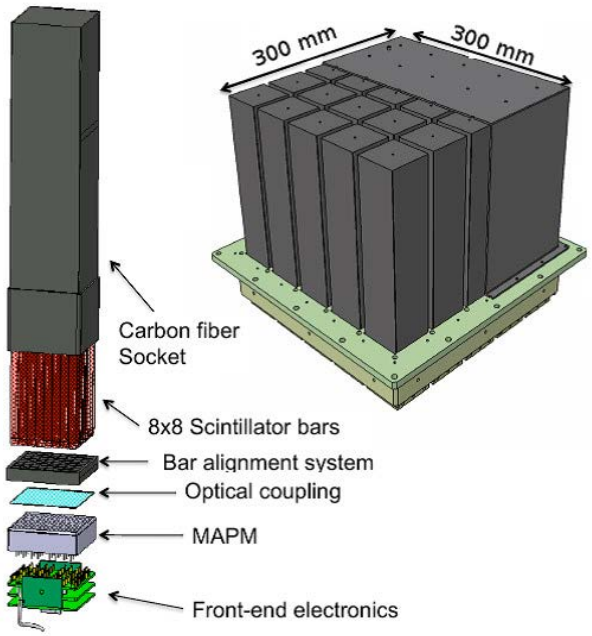

Figure 4.16: The schematic view of POLAR detector. Array of 40×40 plastic scintillator bars (each 5.8×5.8×172 mm^3), and bars grouped in 25 modules (Kole et al., 2016).

4.4 Compton Camera

As shown in the previous section, the wide-FoV GRB polarimeter has four problems due to the lack of imaging capability and measurement of θ_{det}. In the energy range from a few hundreds of keV to a few tens of MeV, Compton camera has a potential to be an imaging polarimeter with wide-FoV and to be an essential solution to such problems. The basic principle of Compton camera is to reconstruct the source direction as a superposition of event circle direction as shown in Figure 4.17 by measuring the momentum of Compton scattered photon. The measured three-dimensional scattering distribution $\mathcal{D}(\theta_{det}, \phi_{det})$ allows to determine the polarization states without the degradation of M and MDP due to the effect of off-axis incidence, although it has not been demonstrated yet. Therefore, a basic Compton camera intrinsically has a potential to resolve both the problems (3) and (4) shown in the previous section. To resolve the residual problems (1) and (2), a high-quality imaging based on a reliable and sharp PSF is required as discussed in Section 3.2.2 and 3.3.

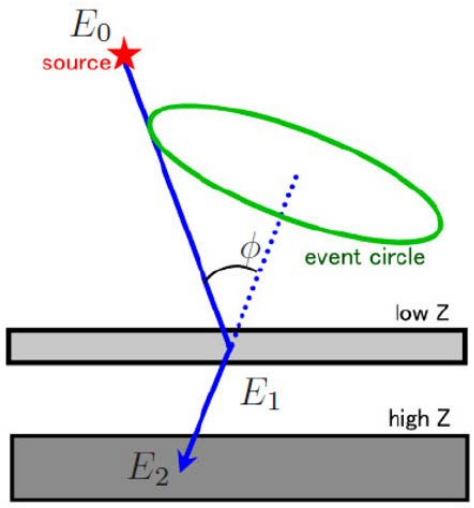

Figure 4.17: Schematic view of Compton cameras (Takada, 2007).

There have been several proposals of Compton cameras, whose objectives include the polarization measurement of the bright gamma-ray sources. They generally aim to improve a quality of image than COMPTEL to suppress the huge background in space according to the lesson of COMPTEL (Schönfelder, 2004). Major approach is improving the error of width of the circle direction by using high-energy resolution detectors. This idea underlies the Compton Spectrometer and Imager (COSI), which is the Ge-based Compton camera designed to study nuclear-line emission and polarization in the MeV band between 200 keV and 20 MeV (Boggs et al., 2004; Chiu et al., 2015). It consists

of ten high-purity germanium crossedstrip detectors that work as the both scatterer and absorber, enable the measurement of the three-dimensional points of the scattering and absorption point, as shown in Figure 4.18. The COSI has an active shield made of BGO scintillator, and the field of view is constrained to be 3.2 sr. Very recently, they succeeded to obtain the gamma-ray images of a few celestial objects and transients including one GRB in the long-duration balloon experiment (Kierans et al., 2017), however they reported that the MDP in this burst was very large ∼60–70% and COSI did not detect the polarization (Lowell et al., 2017).

Another promising approach is to determine the direction of the incident photon event by event, not circle direction, by measuring the initial direction of the Compton recoil electron, which surely change the imaging quality dramatically. Importantly, as pointed out in (Tanimori et al., 2015), the precise measurement of electron tracks achieve a proper geometrical imaging with well-defined PSF, which enables us to perform an accurate imaging spectroscopic measurement as same as optical, X-ray and GeV telescopes . Many groups have proposed and studied the Compton camera with an electron tracker using the stacked solid-state detectors, which is designed to measure the recoil electron with an energy of more than a few MeV (O'Neill et al., 1996; Bloser et al., 2002; Kurfess et al., 2004; Moiseev et al., 2015; Khalil et al., 2016; Tatischeff et al., 2016). On these types of Compton cameras, only the Medium Energy Gamma-Ray Astronomy telescope (MEGA; see Figure 4.19) succeeded the demonstration of gamma-ray imaging polarimetry for on-axis incidence of 100% polarized pencil beams at different energies (0.7, 2, and 5 MeV) (Zoglauer et al., 2004), where the beam images were reconstructed without (at 0.7 and 2 MeV) and with (at 5 MeV) electron tracks (Andritschke et al., 2005). Unfortunately, such a solid state electron tracker provided too sparse tracking to create an idea of well-defined PSF in Compton scattering. A fine electron tracking enough to define a PSF is realized only by an Electron-Tracking Compton Camera (ETCC) with a gaseous electron tracker as discussed in the next chapter.

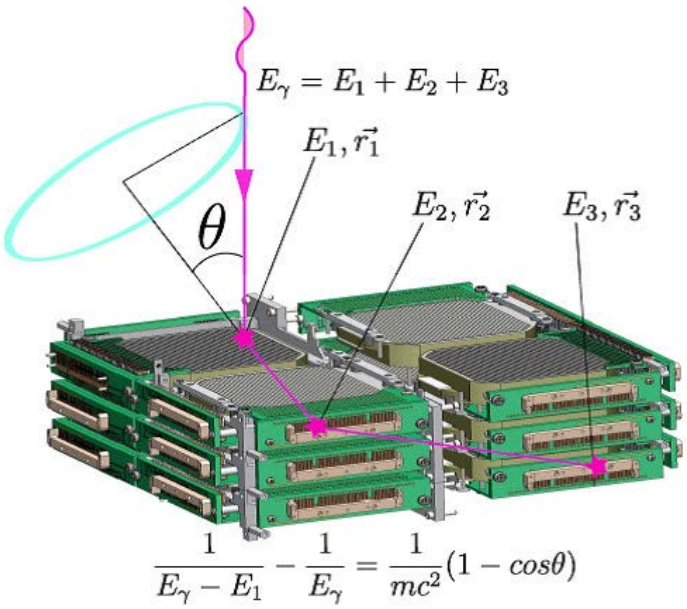

Figure 4.18: Schematic view of COSI detector (Chiu et al., 2015).

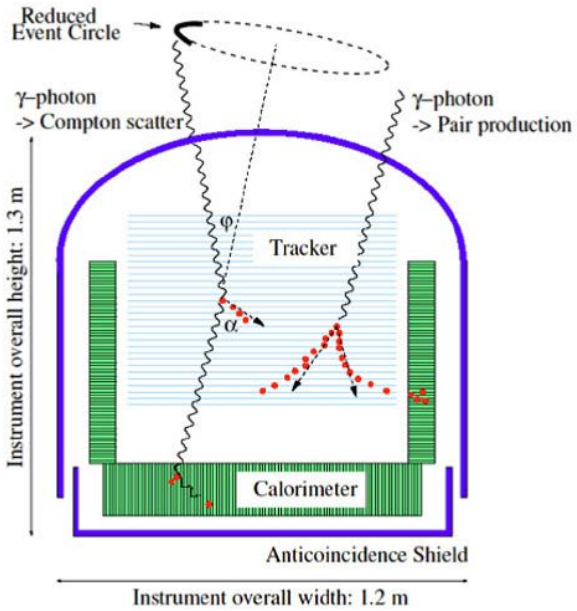

Figure 4.19: Schematic view of MEGA detector (Kanbach et al., 2003).

Chapter 5

Electron-Tracking Compton Camera

We have developed an electron-tracking Compton camera (ETCC) utilizing a gaseous three-dimensional electron tracker since 2004 (Tanimori et al., 2004). The gaseous tracker enables us to measure a quite fine three dimensional tracks as seen in a cloud chamber, while solid state trackers provide only several hit points for a track. Such fine electron tracking at first enables us to define a well-defined PSF, and thus consequently the detection and polarization sensitivity are greatly improved.

To verify the polarimetric performance of the ETCC, we used the ETCC with 30-cm cubic gaseous electron tracker, which has been originally developed since 2013 to measure the sub-MeV gamma-ray spectrum of the Crab with 6 hours balloon flight (Tanimori et al., 2015). Here we overview the detector configuration and the basic performance of the ETCC, which will be used in the polarimetric simulation and experiment in the following chapters.

5.1 Advantages of Electron Tracking

An Electron-Tracking Compton Camera (ETCC) reconstructs the both incident direction and energy of the gamma ray by measuring the momenta of the scattering gamma ray and recoil electron. The reconstructed energy E_0 and unit vector of the momentum direction $\vec{s}_{rcs}$ are expressed as

$$E_0 = E_\gamma + K_e, \tag{5.1}$$

$$\vec{s}_{rcs} = \left(\cos\phi - \frac{\sin\phi}{\tan\alpha}\right)\vec{g} + \frac{\sin\phi}{\sin\alpha}\vec{e}$$

$$= \frac{E_\gamma}{E_\gamma + K_e}\vec{g} + \frac{\sqrt{K_e(K_e + 2m_e c^2)}}{E_\gamma + K_e}\vec{e}, \tag{5.2}$$

$$\tag{5.3}$$

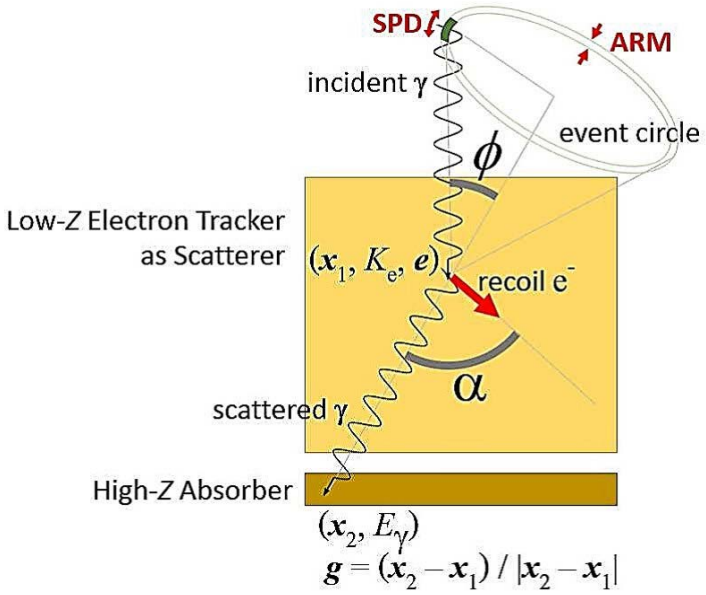

Figure 5.1: Schematic of an Electron-Tracking Compton Camera. It consists of an electron tracker as the scatterer made of low-Z material and an absorber made of high-Z material. The scatterer measures the scattering position $\vec{x}_1$, and the kinematic energy and momentum unit vector of the recoil electron, $\vec{e}$ and K_e, respectively. The absorber measures the absorption position $\vec{x}_2$ and energy of the scattered gamma ray E_γ. The momentum unit vector of the scattered gamma ray is obtained by calculating $(\vec{x}_2 - \vec{x}_1)/|\vec{x}_2 - \vec{x}_1|$ Figure from Sawano (2017).

where E_γ and K_e, and $\vec{g}$ and $\vec{e}$ are the kinetic energies and unit vectors of momentum directions of the scattering gamma ray and the Compton-recoil electron, respectively, ϕ is the polar scattering angle of the gamma ray, and α is the angle between the $\vec{g}$ and $\vec{e}$ as shown in Figure 5.1.

The primary advantage of electron tracking is the realization of the PSF based on geometrical optics, where there has been no definition of two dimensional PSF in Compton cameras. There are two components of the PSF. One is the uncertainty of the scattering angle ϕ, referred as the angular resolution measure (ARM), and the other is of the scattering plane of the gamma ray, referred as the scattering plane deviation (SPD) as shown in Figure 5.1. The errors of the reconstructed direction concerning the ARM and SPD, $\Delta\phi_{ARM}$ and $\Delta\phi_{SPD}$ are derived by

$$\Delta\phi_{ARM} = \arccos(\vec{s}\cdot\vec{g}) - \arccos\left(1 - \frac{m_e c^2}{E_\gamma + K_e}\frac{K_e}{E_\gamma}\right), \tag{5.4}$$

$$\Delta\phi_{SPD} = \mathrm{sign}\left(\vec{g}\cdot\left(\frac{\vec{s}\times\vec{g}}{|\vec{s}\times\vec{g}|}\times\frac{\vec{s_{rcs}}\times\vec{g}}{|\vec{s_{rcs}}\times\vec{g}|}\right)\right)\arccos\left(\frac{\vec{s}\times\vec{g}}{|\vec{s}\times\vec{g}|}\cdot\frac{\vec{s_{rcs}}\times\vec{g}}{|\vec{s_{rcs}}\times\vec{g}|}\right), \tag{5.5}$$

where $\vec{s}$ and $\vec{s}_{rcs}$ are the true and reconstructed unit vectors of the incident gamma ray. The PSF of the Compton camera is defined to contain a half of the gamma rays emitted from the point source within the angular radius. Figure 5.2 shows the cumulative ratio in the PSF for gamma rays from a point source as a function of its angular radius for various angular resolutions of the Compton cameras calculated by a Monte Carlo simulation Tanimori et al. (2015).

We note that the PSF is intrinsically dependent on the worse one of the ARM and SPD. The ARM resolution is limited to several degrees by its kinematical dependence on the Compton scattering angle and Doppler broadening. If the Compton camera has a moderate energy resolution of a few percent at 662 keV, the ARM resolution is nearly equal to the limitation of Doppler broadening. On the other hand, it is quite difficult to obtain the SPD of about 1°. The theoretical limit of SPD resolution is defined by the multiple scattering in the electron tracker. Figures 5.3 show the scatter angle as a function of the energy of electron in the scattering material Ar, Xe, and Si. In the case of Si detectors such as the silicon strip detector, the scatter angle deviation is quite worse than 100° even if the kinetic energy of the electron is 50 keV. On the other hand, a gaseous tracker filled with argon gas of 1 atm makes the the deviation of the scatter angle about 15° with a trajectory length of 1 mm and an electron kinetic energy of 50 keV. In order to achieve a few degree PSF, electron tracking in gaseous detector seems quite essential.

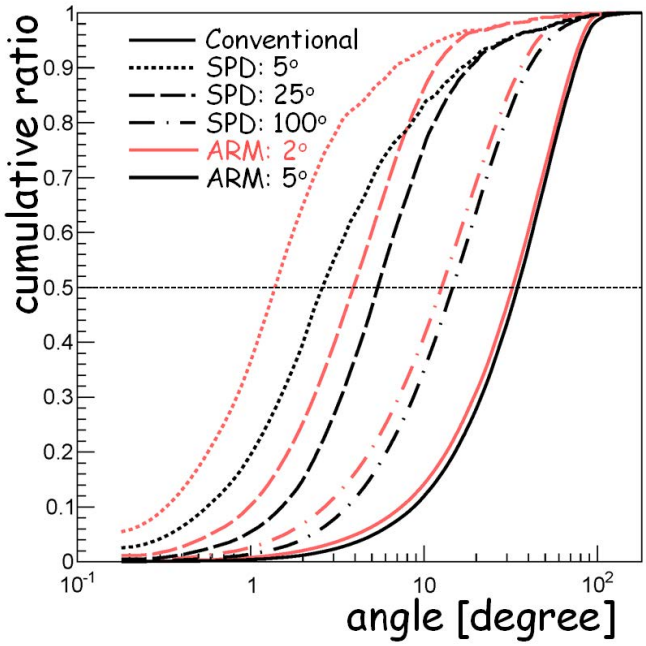

Figure 5.2: Point spread function of Compton cameras depending on the angular resolutions of ARM and SPD, described by the cumulative ratio for gamma rays from a point source as a function of its angular radius (Tanimori et al., 2015).

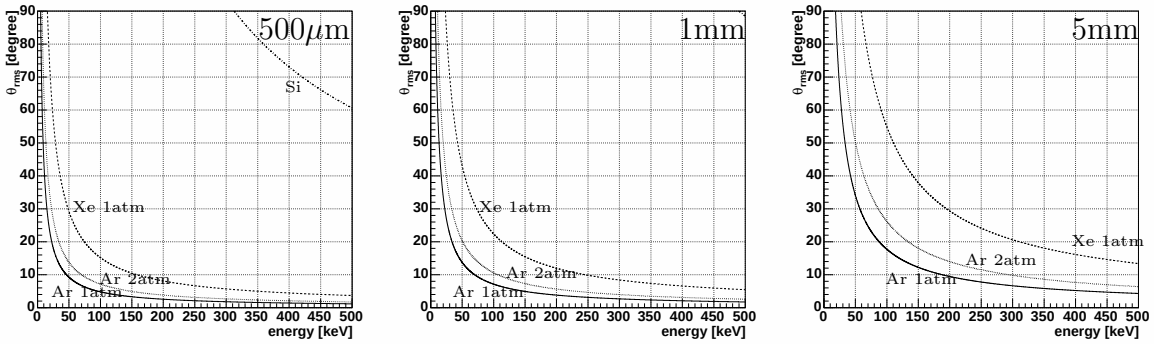

Figure 5.3: Scatter angle deviation with different ranges of the electron (left: 500μm, middle: 1mm, right: 5mm; temperature: 20°C; Takada 2007).

The information of an electron track also gives us the tools to suppress various backgrounds. The angle α (see Figure 5.1) is obtained by two independent ways. One is geometrically, calculating the inner product of the recoil electron vector and the scattered gamma-ray vector. The other is kinematically, calculating based on Compton kinematics with the measured energy deposit in TPC and PSAs. By checking the consistency between these two values, an ETCC rejects Compton scattering fake events such as chance coincidence hits of the TPC and PSAs and events where Compton scattering occurred in the PSAs. We can also obtain the energy-loss rate (dE/dx) of charged particles interacted in TPC by using the relationship of its energy and range calculated from the track information. Therefore, we can identify the kind of particles and reject non gamma-ray backgrounds, such as cosmic rays, neutrons and Compton-recoil electrons escaping from TPC. Thanks to these background suppression tools, without an active veto shielding, ETCC also has the large Field of View (FoV).

5.2 Detector Configuration

Figure 5.4 shows a schematic view and a photograph of the ETCC. Gd2SiO5:Ce (GSO) pixel scintillator arrays (PSAs), which act as absorbers for scattered gamma-rays, are set under the bottom and at each side of the 30 cm cubic TPC, which is filled with an Ar-based gas.

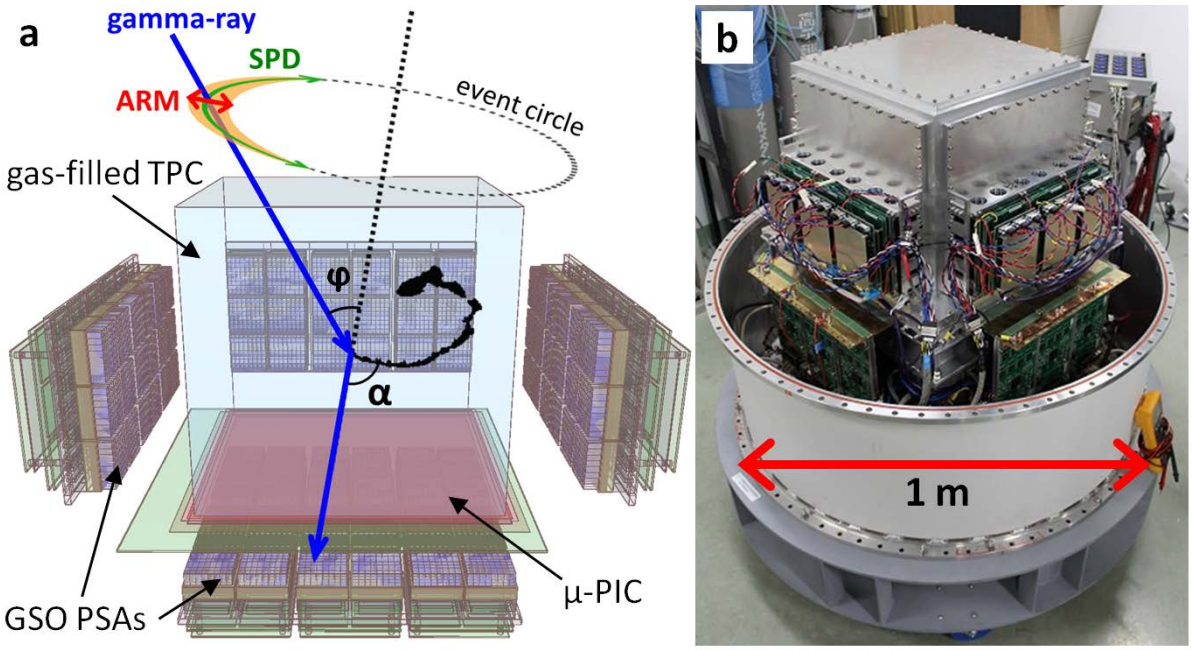

Figure 5.4: (a) Schematic view of the ETCC, which consists of a 30 cm-cubic gaseous time projection chamber (TPC) and pixel scintillator arrays (PSAs). The TPC detects the track and energy of the recoil electron, and the PSAs detect the pixel position of the absorption and the energy of the scattered gamma-rays event by event (Tanimori et al., 2015).

5.2.1 Gaseous Electron Tracker

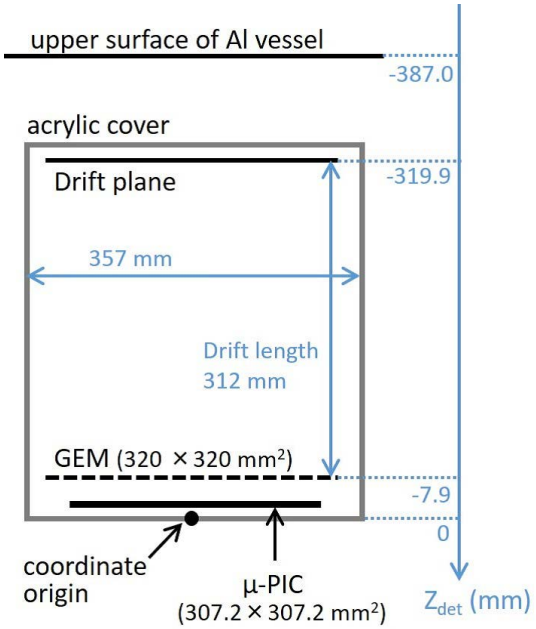

Figure 5.5: Schematic view of the gaseous electron tracker of the ETCC.

As shown in Figure 5.5, the gaseous electron tracker consists of a micro pattern gas detector (μ-PIC; Ochi et al., 2002), a gas electron multiplier (GEM; Sauli, 1997; Tamagawa et al., 2006), and a 312-mm thick gas detection volume. A brief explanation of a μ-PIC and a GEM is given in the caption of Figures 5.6 and 5.7, respectively. The μ-PIC in the gaseous electron tracker has an effective area of 307.2 $\times$ 307.2 mm^2 and 768 $\times$ 768 pixels with a pitch of 400 μm, which are connected orthogonally by 768 anode strips and 768 cathode strips (Takada et al., 2007). GEM with an effective area of 320 $\times$ 320 mm^2 is placed 5 mm above the μ-PIC as a sub-amplifier. GEM is made of a 100 μm-thick liquid crystal polymer, and the hole size and pitch are 70 μm and 140 μm, respectively. The combination of the μ-PIC and the GEM is used as a time projection chamber (TPC), where the electric drift field is applied to the detection volume and the drift time for which the electrons reach to the detector X–Y plane is used for the determination of the position along to the Z-axis. The filling gas of the TPC is a mixtured gas of (Ar 95%, CF_4 3%, iso-C_4H_{10} 2%) with 1 atm, and the gas gains of the μ-PIC and GEM are 2000 and 10, respectively.

We used the TPC readout board (Mizumoto et al., 2015) to read the μ-PIC signals. The TPC readout board contains 4 flash ADCs, an Ethernet port, an FPGA, and 8 CMOS FE2009bal ASIC chips, as shown in Figure 5.8. All discriminated signals from 128 input channels are fed to the FPGA. In the FPGA, the hit patterns and timing of the anode or cathode electrodes are individually synchronized with 100MHz (10 ns) clocks and recorded to the memory module in the VME bus. The three-dimensional hit position in the TPC

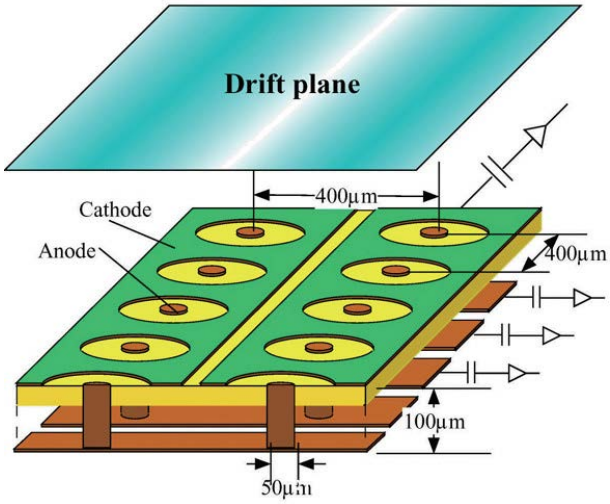

Figure 5.6: Schematic view of μ-PIC (Ochi et al., 2002). The primary electrons in the gas volume drift toward the anode and are multiplied by the gas avalanche mechanism due to a higher electric field between the anodes and the cathodes. The anodes are connected to the back strips, and the cathodes are printed on the surface to surround the anode pin; there is also a field plane. Two-dimensional hit coordinates are obtained by reading out both the anode and cathode strips. μ-PIC has a fine-position resolution of 120 μm (root-mean square (RMS)) and a high, stable gas gain of $\sim$ 6000 (Nagayoshi et al., 2004).

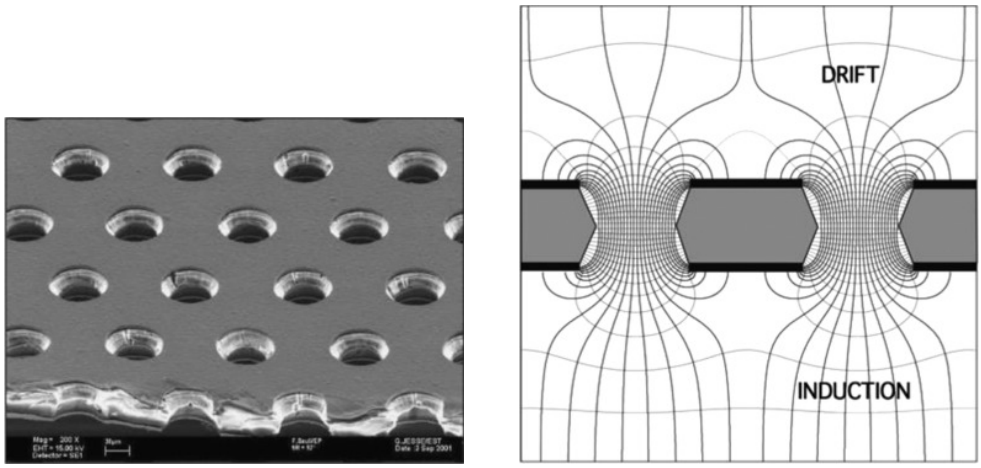

Figure 5.7: Gas Electron Multiplier electrode is a thin polymer foil, metal-coated on both sides and pierced with a high density of holes, typically 50–100 mm^{-2} (left panel). GEM electrode develops near the holes field lines and equipotential as shown in the right panel. The large difference of potential applied between the two sides of the foil provides the avalanche multiplication, and electrons are transfered into the lower section of the structure (Sauli, 2016).

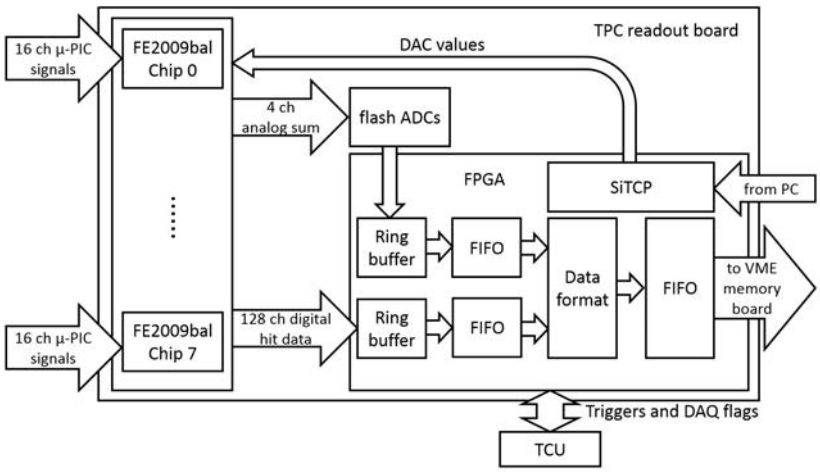

Figure 5.8: Block diagram of μ-PIC readout board (Mizumoto et al., 2015).

is obtained in the off-line analysis, where an adequate gate width is applied to anode and cathode hit strips using the hit timing (see Section 5.3). The clock duration between rising and falling edges crossing the threshold is also recorded as the time-over-threshold (TOT), which roughly corresponds to the deposited energy. All analog signals from from 128 input channels are summed with every 32 channels by FE2009bal ASIC chips on the board, and the waveforms of summed signals are individually digitized by 10-bit, 50MHz Flash ADCs. Summed waveforms are used to calculate the energy deposition of a charged particle.

Figure 5.9 shows a typical example of the recoil electron track image obtained by the gaseous electron tracker. Note that the electron track indicates the Bragg peak at the track end point by the TOT. Figure 5.10 shows an energy spectrum obtained by the gaseous electron tracker under the irradiation of X-rays from radioactive source ^{109}Cd, and one can clearly see the peak of X-ray fluorescences of Ag Kα (22.2 keV), Pb Lα (10.6 keV), Cu Kα (8.0 keV) and possibly Ar Kα (3.0 keV), indicating that the threshold level of the TPC is about 1 keV. The uniformities of gas gain and energy resolution of the TPC are shown in Figure 5.11, respectively. In the current operation, the typical gas gain is about 22000 and their non-uniformity is about 9% RMS. The typical energy resolution is 21% at FWHM for 22.2 keV, as shown in Fig. 5.12. Figure 5.13 shows a correlation between the track range and the energy loss in the TPC. The dE/dx distribution provides the identification of recoil electrons that stop in the TPC from minimum-ionizing particles such as cosmic rays and penetrating high-energy recoil electrons escaping from the TPC. The broken line shows the numerical calculation for fully-contained electrons, which is consistent with the measurement.

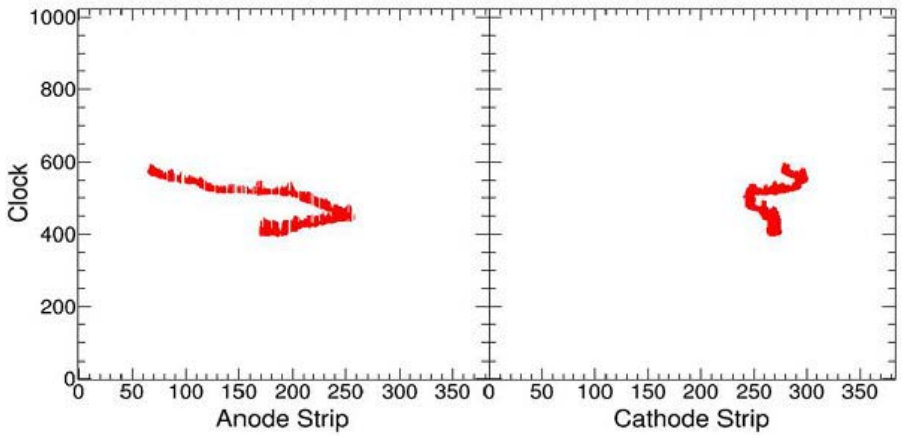

Figure 5.9: Typical examples of the projected track of a recoil electron, where both hit points are depicted. Since the drift velocity is 8 cm/μsec, 1 clock corresponds to 0.8mm. In addition, the clock duration between rising and falling edges crossing the threshold is recorded as the time-over-threshold (TOT), which roughly corresponds to the deposited energy (Mizumoto et al., 2015).

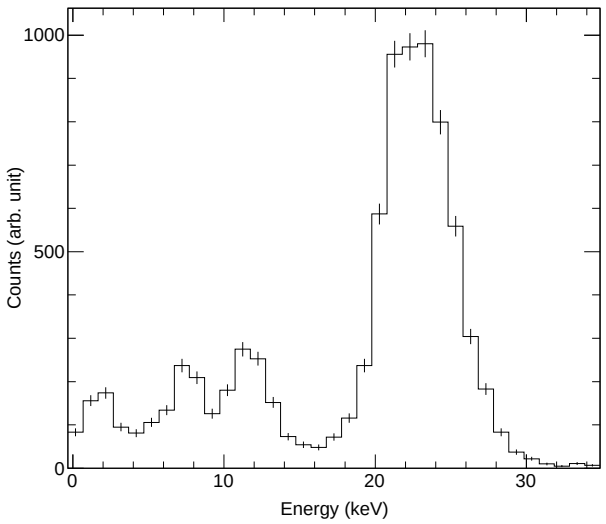

Figure 5.10: Spectrum obtained by irradiation of radioactive isotope source of ^{109}Cd. photoelectric peaks can be seen at Ag Kα (22.2 keV) from ^{109}Cd, and Pb Lα (10.6 keV), Cu Kα (8.0 keV) and possibly Ar Kα (3.0 keV) from the materials that are used for the TPC (Sawano, 2017).

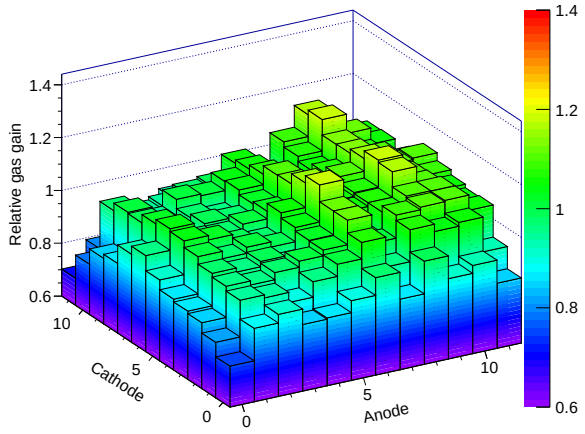

Figure 5.11: Gas gain map of the TPC. Color maps represent the relative gas gain with respect to the mean gas gain of the whole region (Sawano, 2017).

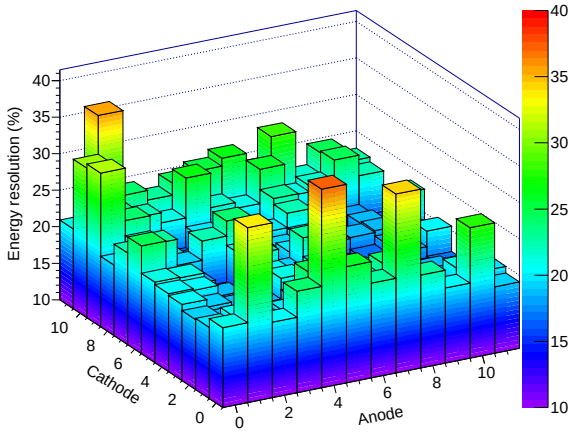

Figure 5.12: Distribution of the energy resolution for Ag Kα (22.2 keV). The mean energy resolution is about 21% (FWHM) (Sawano, 2017).

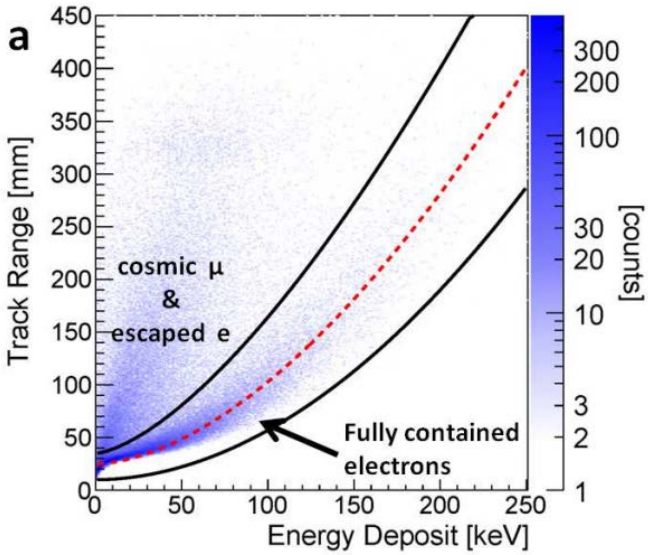

Figure 5.13: Track range vs the energy loss in the TPC under the condition of gamma-ray irradiation from ^{137}Cs (3 MBq) at a distance of 1 m in the laboratory (Tanimori et al., 2015). The broken solid line represents the numerical calculation curves of the energy loss for fully-contained electrons.

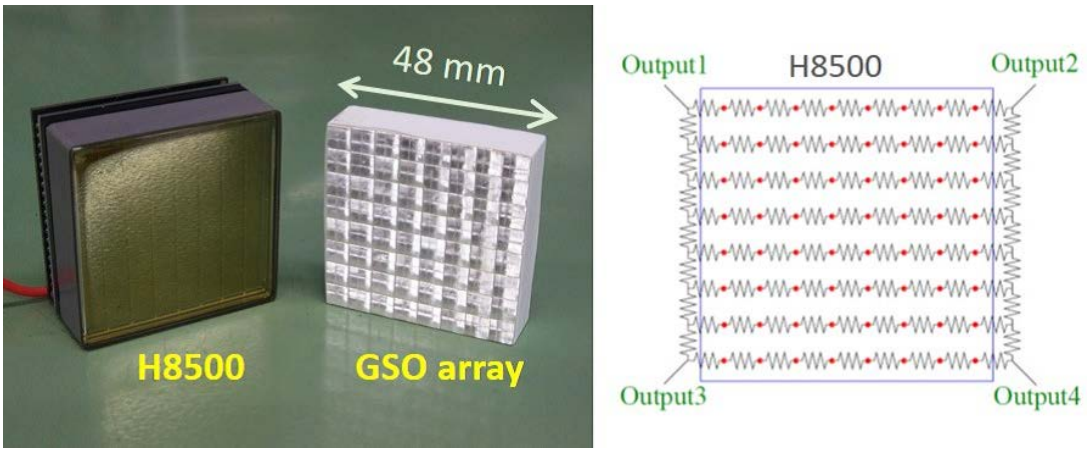

Figure 5.14: (Left) Multi-anode photomultiplier Hamamatsu H8500 and pixel scintillation arry of GSO crystal (8×8 pixels). (Right) Schematic view of the resistor matrix attached to a PSA, which has 64 inputs from a PSA (red circle) and 4 outputs of divided charge at the corner (Mizumoto et al., 2015).

5.2.2 Scintillation Camera

The PSA consists of 64 pixels of GSO:Ce scntillators, a multi-anode Flat Panel Photomultipier tube (PMT) H8500 manufactured by Hamamatsu Photonics as shown on the left in Figure 5.14. This PMT has a common photocathode and 64-segmented anodes with an area of 6×6 mm^2 for each pixel. The geometrical area is 52×52 mm^2 and thus the effective area is 89% of that geometrical. Each pixel scintillator has an incident area of 6×6 mm^2 and a height of 13 mm. 8×8 pixels of GSO crystal forms an array unit, in which a reflector of ESR is inserted between the pixels (Nishimura et al., 2007). This array is mounted on the PMT with an optical cement, BC-600. A resistor matrix is attached to each PSA as a readout circuit, as shown on the right in Figure 5.14, by which the 8×8 channels from the PSA reduce four signals from the four corners of the resistor matrix (Nishimura et al., 2007). The hit position within a PSA is calculated from the weighted average of four signals. An example of the reconstructed hit distribution for the gamma rays with an energy of 662 keV is shown in Figure 5.15. The energy deposition within a PSA is reconstructed by a summation of the pulse heights calculated by the sample and hold circuit and 12-bit ADCs in the PSA readout modules (Mizumoto et al., 2015).

The performance of the PSAs is summarized in Figure 5.16 and Figure 5.17. The distribution of the gain of the all GSO pixels in the ETCC is shown in Figure 5.16(a), and has a deviation of 25% at 1σ. The energy resolutions of the all pixels for the same condition are distributed from 10% to 14% at 662 keV, as shown in Figure 5.16(b). The energy resolution dependence on the gamma-ray energy as the entire scintillation camera is shown in Figure 5.17, and the energy resolution of the entire scintillation camera system is approximately 11% at 662 keV.

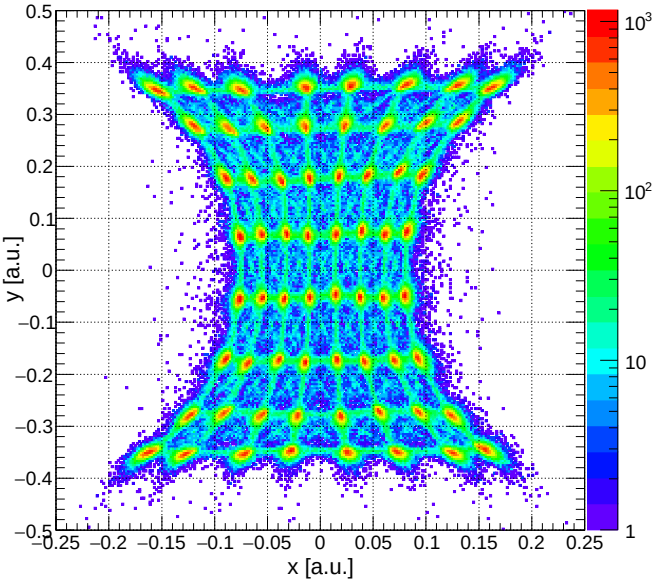

Figure 5.15: Reconstructed hit distribution image of the one unit of the PSA for the gamma rays with an energy of 662 keV (Mizumoto et al., 2015).

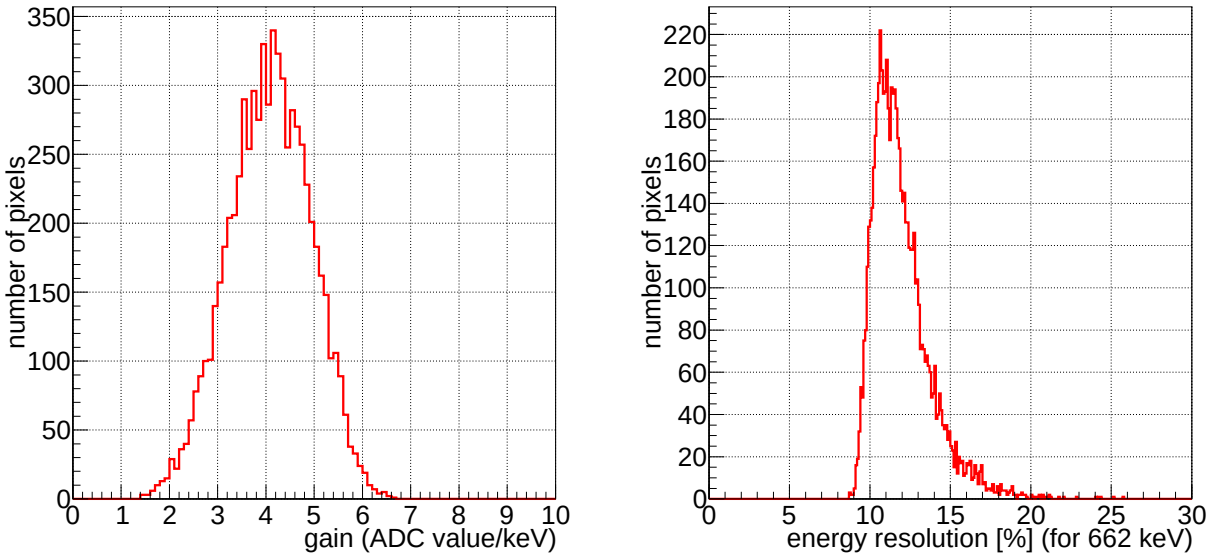

Figure 5.16: (Left) Gain distribution of the whole channels of the scintillation camera. The unit of the gain is ADU/keV and divided by the average. (Right) the same but for the energy resolution at FWHM for 662 keV (Mizumoto et al., 2015).

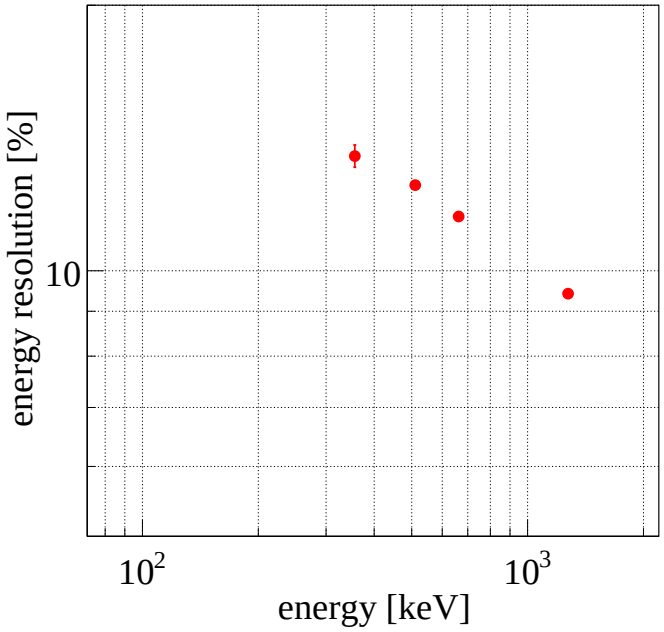

Figure 5.17: Energy resolution of the entire scintillation camera as a function of the incident gamma-ray energy (Mizumoto et al., 2015).

5.3 Event Reconstruction

Events are taken with a coincidence between the TPC and PSAs in the ETCC. There exists, however, lots of background events such as random coincidence events, charged particles such as cosmic muons, environmental gamma rays, and incomplete events, in which a electron penetrates from the gas volume or coming from the outside of the gas volume. To find correct events in which Compton scattering occurs in the active volume of the TPC and a electron stops within that active volume with one hit in PSAs, we performed a couple of following selection criteria.

1. **Energy loss rate cut**

   Energy loss rates (or, stopping power) varies depending on β, or the velocity of the particle. For the electrons in the argon gas with an energy up to a few hundred keV, the practical range R_p is approximately described as $R_p = 0.71 \left(\frac{E}{1\,\mathrm{MeV}}\right)^{1.72}\ \mathrm{g\,cm^{-2}}$, where E is the energy of the electron (Sauli, 1977). To reject the high energy electrons escaping from the active volume of the TPC or heavy ions, energy loss rate cut is applied as follows,

   $$\begin{cases} R_p \leq (1/\rho)0.71 \times E_e^{1.72+a_u} + b_u \\ R_p \geq (1/\rho)0.71 \times E_e^{1.72+a_l} + b_l \\ R_p < R_p^{\mathrm{lim}} \end{cases}, \tag{5.6}$$

   where E_e is the energy loss in the TPC, ρ is the density of the gas of the TPC, and the R_p is the practical range of the charged particle trajectory in the TPC, again. a_u, b_u, a_l, b_l, and R_p^{lim} are constants for the event selection. The range R_p is derived by calculating the length of the diagonal of the rectangular that surrounds the three-dimensional particle trajectory, formally described as

   $$R_p = \sqrt{(x_{\mathrm{max}} - x_{\mathrm{min}})^2 + (y_{\mathrm{max}} - y_{\mathrm{min}})^2 + (\min(z_{\mathrm{x,max}}, z_{\mathrm{y,max}}) - \max(z_{\mathrm{x,min}}, z_{\mathrm{y,min}}))^2} \tag{5.7}$$

   where x_{max} and x_{min} are the maximum and minimum position coordinates in the cathode hits, respectively, y_{max} and y_{min} are the same but for the anode hits, $z_{\mathrm{x,max}}$ and $z_{\mathrm{y,max}}$ are the maximum position coordinates of the hits in the drift direction for cathode and anode strip data, respectively, and $z_{\mathrm{x,min}}$ and $z_{\mathrm{y,min}}$ are the same but for the minimum position coordinates.

2. **Fiducial volume cut**

   Charged particles coming from the outside of the active volume of the TPC cannot be measured the total kinetic energy properly. To remove such events, the events for which there are hits near the edge of the active volume in the TPC are considered as bad events transporting the boundary of the active volume.

3. Total energy loss cut

For the calibration source, the incident energy of the gamma rays is already-known. To test the detection efficiency of the gamma rays from radioisotopes, we lay down the condition where the summation of the energy losses in the TPC and PSA should be equal to the incident gamma-ray energy, or

$$\left| \frac{E_{\rm tpc} + E_{\rm psa}}{E_{\rm inc}} - 1 \right| \leq p, \tag{5.8}$$

where $E_{\rm tpc}$, $E_{\rm psa}$ and $E_{\rm inc}$ are the energy losses in the TPC and PSA, respectively, and the incident energy, and the p is the fraction of acceptable residual.

Determination of the direction of the recoil electron

To determine the coordinate of the absorption point in the PSA, the scintillator pixel is firstly identified in the butterfly image, and then the coordinate of the center of the pixel is regarded as the absorption point. The Compton-scattering points and the direction of the recoil electrons are determined by the two sets of the two-dimensional hit images whose space are the clock of the TPC (Z-axis) versus the position number of the $\mu-$PIC strip (X-axis for cathode and Y-axis for anode). First, the three-dimensional track is reconstructed by the off-line coincidence of the X–Z and Y–Z images in the three-dimensional space. Next, the projection to the X–Y plane is made from the three-dimensional track. We consider that the scattering point projected to the X–Y plane must be located at the closest hit point from the absorption point (Komura et al., 2013). We also consider that the Z-coordinate of the scattering point corresponds to the mean of the hits satisfying the condition on the X–Y projected plane. The direction of the recoil electron is determined as a composite sum of two vectors of the gradients of the obtained two-dimensional hit images of X–Z and Y–Z planes.

5.4 Basic Performances

We checked the performance of the ETCC by using the radioisotopes (RIs), ^{139}Ce (166 keV) , ^{133}Ba (356 keV), ^{22}Na (511 keV), ^{137}Cs (662 keV) and ^{54}Mn (835 keV), placed approximately 2 m from the detector. Figure 5.18 shows the energy resolution of the ETCC, and its dependence on the incident gamma-ray energy is described as

$$\frac{\Delta E}{E} = 10.7 \times \left(\frac{E}{662\,\text{keV}} \right)^{-0.5} [\%] \quad \text{(FWHM)}. \tag{5.9}$$

The effective area is calculated by counting the events under the condition where the total energy loss is consistent within the twice FWHM of the energy resolution from the incident gamma-ray energy. Figure 5.19 shows the on-axis effective area of the ETCC with

a simulation result (Sawano, 2017), which has a good consistency with errors of +26%, −6%, −14%, −6%, and −10% for 166 keV, 356 keV, 511 keV, 662 keV, and 835 keV, respectively. For 662 keV gamma rays, the detection efficiency as a function of zenith angle is shown in the left panel of Figure 5.19. We may conclude that the acceptance FoV of the ETCC is approximately 180° (2π sr) (Matsuoka et al., 2015).

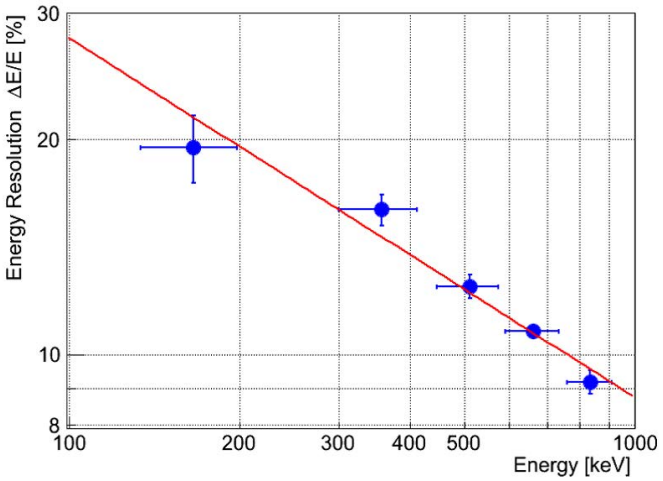

Figure 5.18: Energy resolution of the current ETCC. The fitted line is also shown with the red line (Sawano, 2017).

Figure 5.20(a) shows the measured ARM of the ETCC, and the calculated ones for the cases of the use of GSO and $LaBr_3$ crystals derived by the uncertainty of the measurement of the energy of the scattering gamma rays. The measured ARMs are close to the limit of the calculation. The discrepancies between the measured ARMs and the calculation indicates the uncertainty of 8 mm for the measurement of the scattering position in the TPC. Figure 5.20(b) shows the SPD distribution for the radioisotope of ^{137}Cs (662 keV), and the FWHM of the SPD is about 200°, which is about two times worse than the expected SPD resolution, due to multiple scattering in the gas. After the experiments mentioned in this thesis, SPD was improved to ∼100° (Tanimori et al., 2015). Figure 5.21 shows the measured variations of PSF for the conventional Compton Camera and ETCC after the improvement of SPD as a function of gamma energy with the simulation results derived with hypothetically improved ETCC (2° of ARM and 15° of SPD at 662 keV). As mentioned above, SPD of 200° is used in the whole of this thesis.

Thanks to the well-defined PSF, the ETCC provides the efficient background rejection similar to optical and X-ray telescope. We demonstrate the imaging spectroscopy to reconstruct the the correct energy-spectrum at a region of interest by using the ETCC. Figure 5.22 shows an image of ^{137}Cs (662 keV) source placed at the off-axis with a polar angle of 20°, and its air-scattered gamma-ray background. We can measure the energy distribution of both the source and the background within the radius similar to the PSF (15°). By subtracting the background distributions, the gamma-ray line at 662 keV clearly

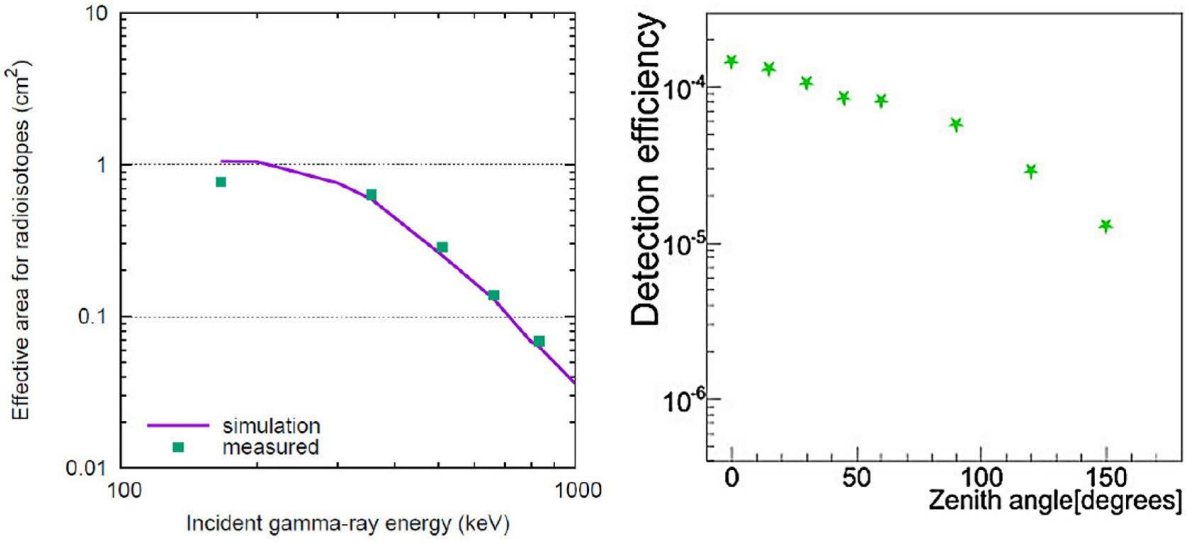

Figure 5.19: (Left) Effective area of the current ETCC for the RI sources (green solid triangle). The simulated effective area is also shown with the purple line (Sawano, 2017). (Right) Detection efficiency of ETCC at various zenith angles at the energy of 662 keV (Matsuoka et al., 2015).

remains without Compton edges and other lines, which in general appear in conventional gamma spectroscopy.

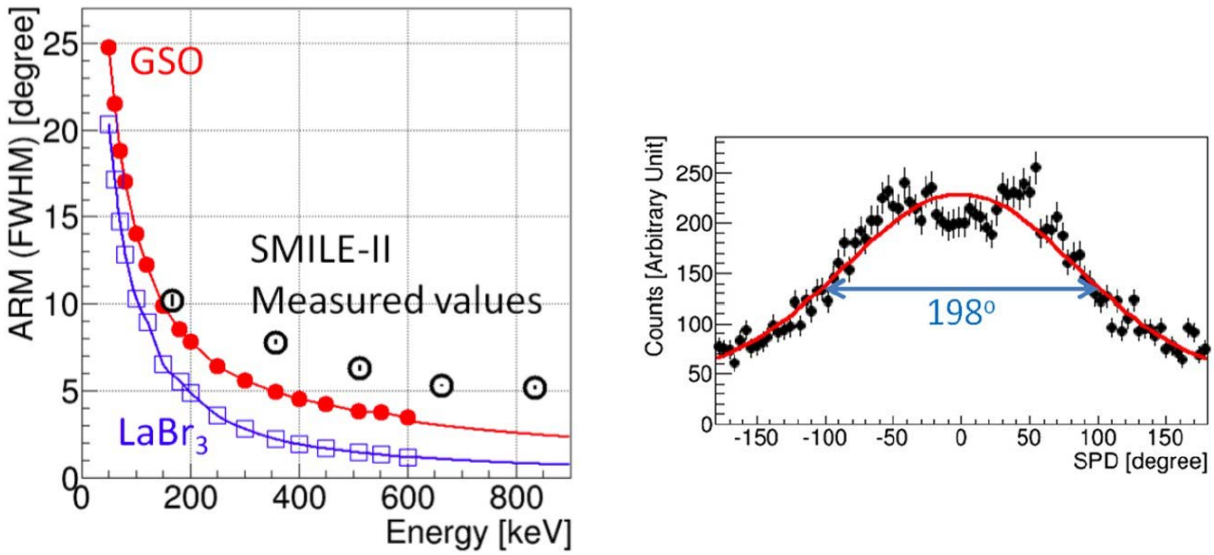

Figure 5.20: (Left) The energy dependence of the ARM of the current ETCC (open black circle). Calculations by the energy uncertainty are plotted with filled red circle and open blue square for GSO and $LaBr_3$ crystals, respectively. (Right) SPD distribution of the current ETCC using the simple track reconstruction method for an incident gamma-ray of 662 keV (Tanimori et al., 2015).

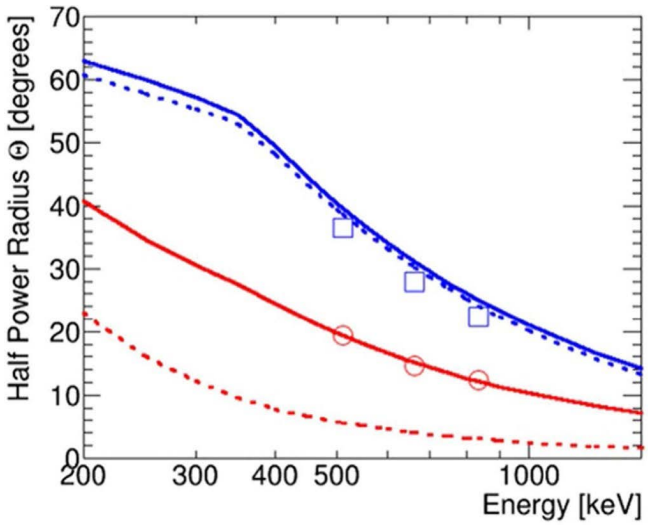

Figure 5.21: Measured variation of PSF with the (blue squares) conventional Compton camera and (red circles) ETCC analyses as a function of gamma-ray energy. Red solid and dotted lines show the simulation results with the present and improved (ARM = 2° and SPD = 15° at 662 keV) ETCCs, respectively, where the energy dependences of ARM and SPD are taken into account. Blue solid and dotted lines are the same simulation results of the CC analysis with ARM = 5° (present) and 2° (improved), respectively (Tanimori et al., 2017).

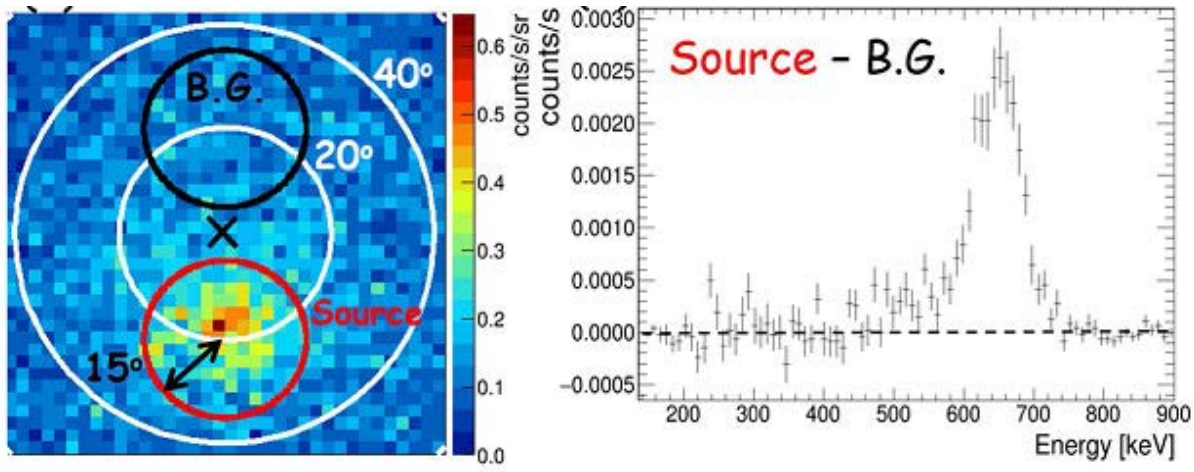

Figure 5.22: (Left) A image of ^{137}Cs (2.9 MBq) source at the off-axis with a polar angle of 20°. Red and black circles, each of which is 15° in radius, indicate source and background regions, respectively. (Right) The spectrum after air-scattered gammas within the PSF(∼15°) are removed, using the region symmetrical about the centre of the FoV (black circle in left panel) as the background region (Tanimori et al., 2017).

Chapter 6

Simulation Studies of Polarization Measurement

As discussed in Chapter 4, Compton cameras, including the ETCC, can be used as Imaging Compton polarimeters. Compton camera determines the three-dimensional direction of the scattered gamma-ray as the direction from the interaction point to the absorption point and obtains the angular distribution of the scattered gamma-ray $\mathcal{D}(\theta_{det}, \phi_{det})$ for each gamma-ray. In addition, the ETCC uniquely determines the incident direction event by event; therefore, θ_{ph} and ϕ_{ph} in the photon coordinate system can be geometrically calculated. Therefore, the ETCC is able to estimate precisely the effect of an off-axis incidence and hence enables us to measure the polarization within a large FoV. Furthermore, due to powerful background suppressions with a sharp PSF and particle identification of the electron tracks, we expect a much better MDP than that of standard Compton cameras even in intense background conditions, such as space. To calculate the MDPs of the ETCC, we estimated the modulation factor for various energetic gamma-rays, incident directions, and polarization directions using Monte Carlo simulations.

6.1 Physics Model of the ETCC

We constructed a simulation software with a detailed geometrical model of the ETCC (Sawano et al., 2014) based on the Geant4 tool kit (Agostinelli et al., 2003). To calculate the detection efficiency, we used the Geant4 (ver. 4.9.5p01) and the `Livermore` package, which supports the electromagnetic process of low-energy gamma rays with an energy of less than 1 MeV. The detection efficiency were obtained mainly from the production of two probabilities: that of Compton scattering and its recoil electron contained fully in the TPC, and that of the full absorption of scattered gammas in the PSAs. The electron drift and gas amplification in the gas volume, the uniformities of gain in TPC and PSAs, and the data acquisition system were not included in the simulations. Despite the simple constitution, the simulated detection efficiency well explains the detection

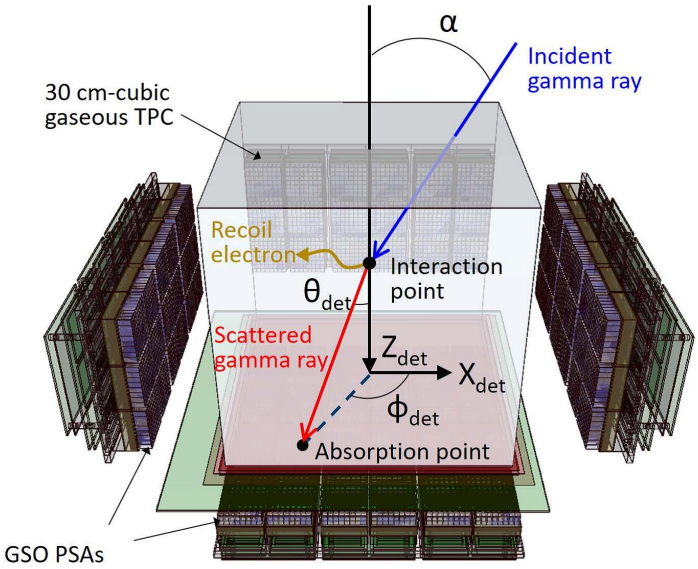

Figure 6.1: Schematic view of the ETCC, which consists of a 30 cm-cubic gaseous time projection chamber (TPC) and pixel scintillator arrays (PSAs). The TPC detects the track and energy of the recoil electron, and the PSAs detect the pixel position of the absorption and the energy of the scattered gamma-rays event by event. The X_{det}-Y_{det} plane of the ETCC is defined to be parallel to the bottom plane of the TPC, and the Z_{det}-axis is defined to be perpendicular to the X_{det}-Y_{det} plane. The Compton scattering angles θ_{det} and ϕ_{det}, and the incident angle α are also indicated as defined in Figure 3.6. Figure adapted from Komura et al. (2017).

efficiency measured in the ground experiments using non-polarized gamma-ray sources (see Figure 5.19 and Tanimori et al. (2015)).

To account for polarized low energy gamma-rays, we used the physics models called `G4EmLivermorePolarizedPhysics` in Geant4 (ver. 4.10.1p02) in this study. This simulation provides the Compton interaction point in the TPC, the pixel position of the absorption in the PSAs for the scattered photons, and the energies of the scattered photon and recoil electron for each incident photon. As shown in Figure 6.1, the three-dimensional direction of the scattered gamma-ray is determined as the direction from the interaction point to the absorption point. Then, the angular distribution of the scattered gamma-ray $\mathcal{D}(\theta_{det}, \phi_{det})$ is obtained for each gamma-ray. In addition, ETCC uniquely determines the incident direction event by event according to the Equation (5.2); therefore, θ_{ph} and ϕ_{ph} in the photon coordinate system can be geometrically calculated. As it does not include the electron tracking in the TPC, we do not take account of the uncertainty of the interaction point. This is not serious because its effects on the θ_{ph} and ϕ_{ph} for each photon are small, typically 1° and a few degrees, respectively.

6.2 Event Reconstruction

Compton scattering events are selected according to the following criteria: (a) Compton scattering occurs in the TPC volume, (b) the photoelectric absorption occurs in the PSA for the scattering gamma-ray, (c) the recoil electron should be stopped in the TPC, (d) the energy deposits in the TPC and PSA exceed the detector thresholds, and (e) without the loss of the incident photon energy within a certain energy resolution. Here the particle identification by dE/dx of a recoil electron is emulated by the criteria 'c'. For the real detector, the detector thresholds are set to be 1 keV and 90 keV for TPC and PSA, respectively. We used the energy resolutions of the TPC and PSA following Gaussian distribution with the FWHM of 22% for 22 keV and 11% for 662 keV, respectively, having an energy dependence of $E^{-0.5}$ due to statistical fluctuations from the measurement of the instrument.

On-axis incidence case

After applying the event selection criteria, the angular distribution of scattered gamma-rays $\mathcal{D}(\cos\theta_{det}, \phi_{det})$ and the integrated azimuthal angle distribution $\mathcal{N}(\phi_{det})$ are obtained as shown in Figure 6.2 for 200-keV incident gamma-rays, with an incident angle α set to zero (on-axis incidence) and a polarization direction along the X_{det}-axis. Figure 6.2(a) shows $\mathcal{D}_{non}(\cos\theta_{det}, \phi_{det})$ for non-polarized incident gamma-rays, and Figure 6.2(b) shows $\mathcal{D}_{pol}(\cos\theta_{det}, \phi_{det})$ for 100% linearly polarized incident gamma-rays. In both figures, Compton-scattered photons absorbed in the bottom PSAs are modulated near $\cos\theta_{det} = 1$ (i.e., forward scattering events). In Figure 6.2(a), events absorbed in the four side PSAs are modulated near values of ϕ_{det} of $-180°$, $-90°$, $0°$, $90°$, and $180°$ in the range of $\cos\theta_{det}$ between -1.0 and 0.8. Conversely, in Figure 6.2(b), many events are modulated near values of ϕ_{det} of $-90°$ and $90°$, where the direction of the incident gamma-ray is perpendicular to the polarization direction of the incident photon and the Compton scattering cross section is at its maximum according to Equation (3.3). The azimuthal distributions $\mathcal{N}(\phi_{det})$s integrated over θ_{det} are calculated according to

$$\mathcal{N}(\phi_{det}) = \int_{-1}^{(\cos\theta)_{max}} \mathcal{D}(\cos\theta_{det}, \phi_{det})\mathrm{d}(\cos\theta_{det}) \tag{6.1}$$

which is derived from Equation (3.8). Figures 6.2(c) and 6.2(d) show $\mathcal{N}_{non}(\phi_{det})$ and $\mathcal{N}_{pol}(\phi_{det})$, respectively. We found that, in $\mathcal{N}_{non}(\phi_{det})$, a small systematic modulation appears due to the non-uniformity of the detector response, as mentioned in Section 3.2.2. Figure 6.3 shows the azimuthal angle distribution $\mathcal{N}_{cor}(\phi_{det})$ corrected for the response effect according to Equation (3.21) with the best fit curve given by Equation (3.13); the modulation factor of the ETCC is estimated to be 0.52 ± 0.01 for on-axis incident photons with energies of 200 keV.

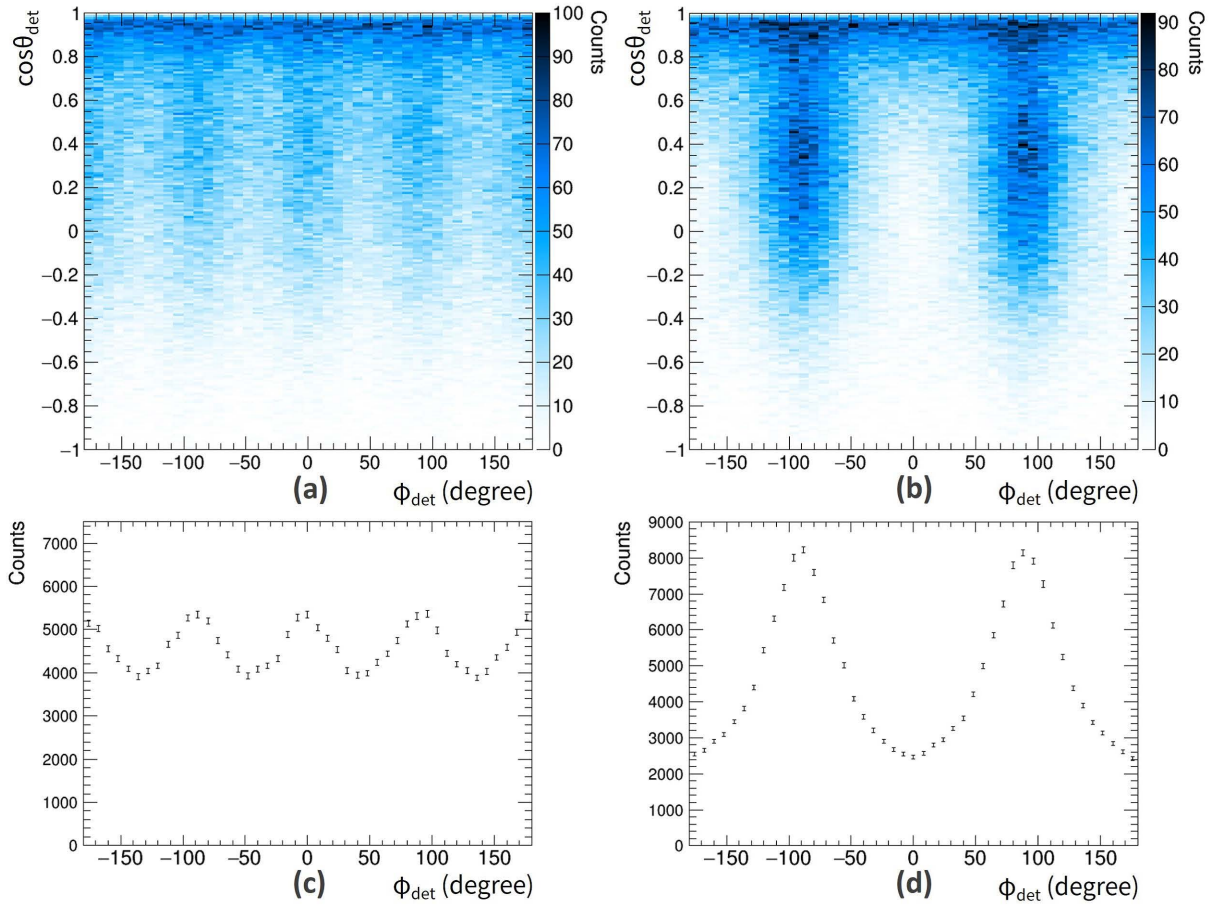

Figure 6.2: Simulated distributions of scattered gamma-rays for incident on-axis 200-keV gamma-rays for the ETCC. (a, b) Two-dimensional scatter plot of $\cos\theta_{det}$ and ϕ_{det} for non-polarized gamma-rays $\mathcal{D}_{non}(\cos\theta_{det}, \phi_{det})$ and for 100% linearly polarized gamma-rays $\mathcal{D}_{pol}(\cos\theta_{det}, \phi_{det})$, respectively. (c, d) Azimuthal event distributions integrated for the $\cos\theta_{det}$ of non-polarized gamma-rays $\mathcal{N}_{non}(\phi_{det})$ and the same for 100% linearly polarized gamma-rays $\mathcal{N}_{pol}(\phi_{det})$, respectively. The error bars in panels (c) and (d) represent the 1σ statistical error. Figures adapted from Komura et al. (2017).

Off-axis incidence case

When α is equal to 30° and a polarization direction is along the X_{det}-axis, the angular distribution of scattered gamma-rays $\mathcal{D}(\cos\theta_{det}, \phi_{det})$ and the integrated azimuthal angle distribution $\mathcal{N}(\phi_{det})$ are obtained as shown in Figure 6.4 for 200-keV incident gamma-rays. In both figures, Compton-scattered photons absorbed in the bottom PSAs are modulated near $\cos\theta_{det} = 1$ and $\phi_{det} = 90°$ since the forward scattering events with small θ_{det} are concentrated in the positive Y_{det} direction and generate large systematic modulations. Comparing to Figure 6.2, we can see that asymmetric modulation due to the off-axis incidence is much larger than the polarization modulation. Figures 6.4(c) and 6.4(d) show

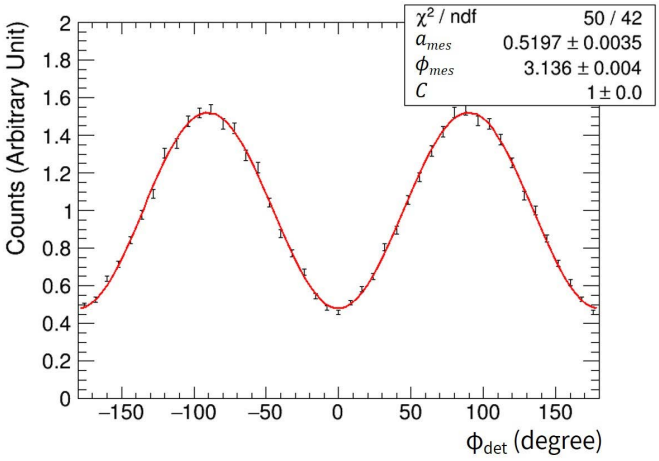

Figure 6.3: Corrected integrated azimuthal angle distribution of scattered photon $\mathcal{N}_{cor}(\phi_{det})$ calculated from $\mathcal{N}_{pol}(\phi_{det})/\mathcal{N}_{non}(\phi_{det})$. Figure adapted from Komura et al. (2017).

$\mathcal{N}_{non}(\phi_{det})$ and $\mathcal{N}_{pol}(\phi_{det})$, respectively. If we applied the cancellation of the effect due to the non-uniformity of the detector response to $\mathcal{N}_{pol}(\phi_{det})$ according to Equation (4), the obtained azimuthal angle distribution $\mathcal{N}_{cor}(\phi_{det})$ is far from a symmetrical distribution, as shown in Figure 6.5. From this response-corrected azimuthal angle distribution, we obtained a modulation factor of 0.45 ± 0.01, which is not reliable.

As mentioned in Section 3.2.3, we first have to transform the coordinate system to the photon system and calculate the azimuthal angle distribution in this system before canceling out the non-uniform response. Figure 6.6 shows the angular distribution of scattered gamma-rays $\mathcal{D}(\cos\theta_{ph}, \phi_{ph})$ and the integrated azimuthal angle distribution $\mathcal{N}(\phi_{ph})$ in photon coordinate system calculated from $\mathcal{D}(\cos\theta_{det}, \phi_{det})$ according to Equation (3.24) assuming $(\alpha, \beta) = (30°, 0°)$. Figure 6.7 shows the azimuthal angle distribution $\mathcal{N}_{cor}(\phi_{ph})$ with the best fit curve given by Equation (3.13), where the symmetries are obviously recovered. The modulation factor of the ETCC is estimated to be 0.53 ± 0.01 for on-axis incident photons with energies of 200 keV. Thanks to the transformation of the coordinate system to the photon system, the modulation factor is nearly independent of the incident gamma-ray direction.

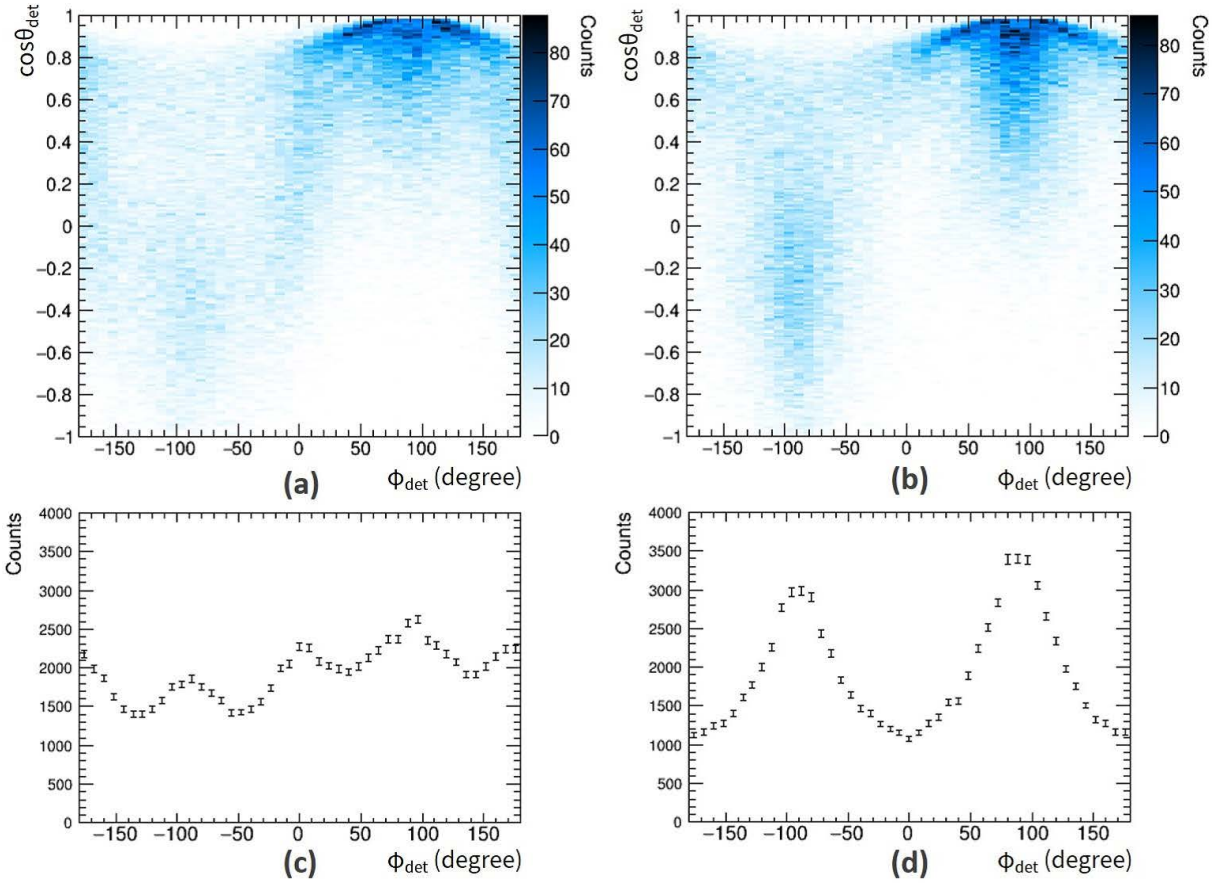

Figure 6.4: Simulated distributions of scattered gamma-rays for incident 200-keV gamma-rays for the ETCC, when the incident angle is equal to 30°. (a, b) Two-dimensional scatter plot of $\cos\theta_{ph}$ and ϕ_{ph} for non-polarized gamma-rays $\mathcal{D}_{non}(\cos\theta_{det}, \phi_{det})$ and for 100% linearly polarized gamma-rays $\mathcal{D}_{pol}(\cos\theta_{det}, \phi_{det})$, respectively. (c, d) Azimuthal event distributions integrated for the $\cos\theta_{det}$ of non-polarized gamma-rays $\mathcal{N}_{non}(\phi_{det})$ and the same for 100% linearly polarized gamma-rays $\mathcal{N}_{pol}(\phi_{det})$, respectively. The error bars in panels (c) and (d) represent the 1σ statistical error.

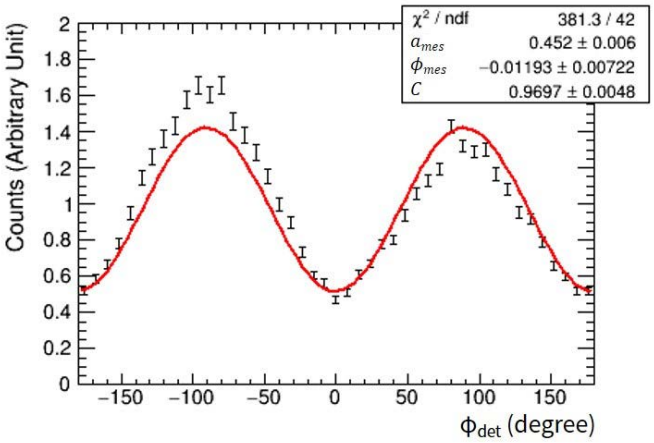

Figure 6.5: Corrected integrated azimuthal angle distribution of scattered photon $\mathcal{N}_{cor}(\phi_{det})$ calculated from $\mathcal{N}_{pol}(\phi_{det})/\mathcal{N}_{non}(\phi_{det})$.

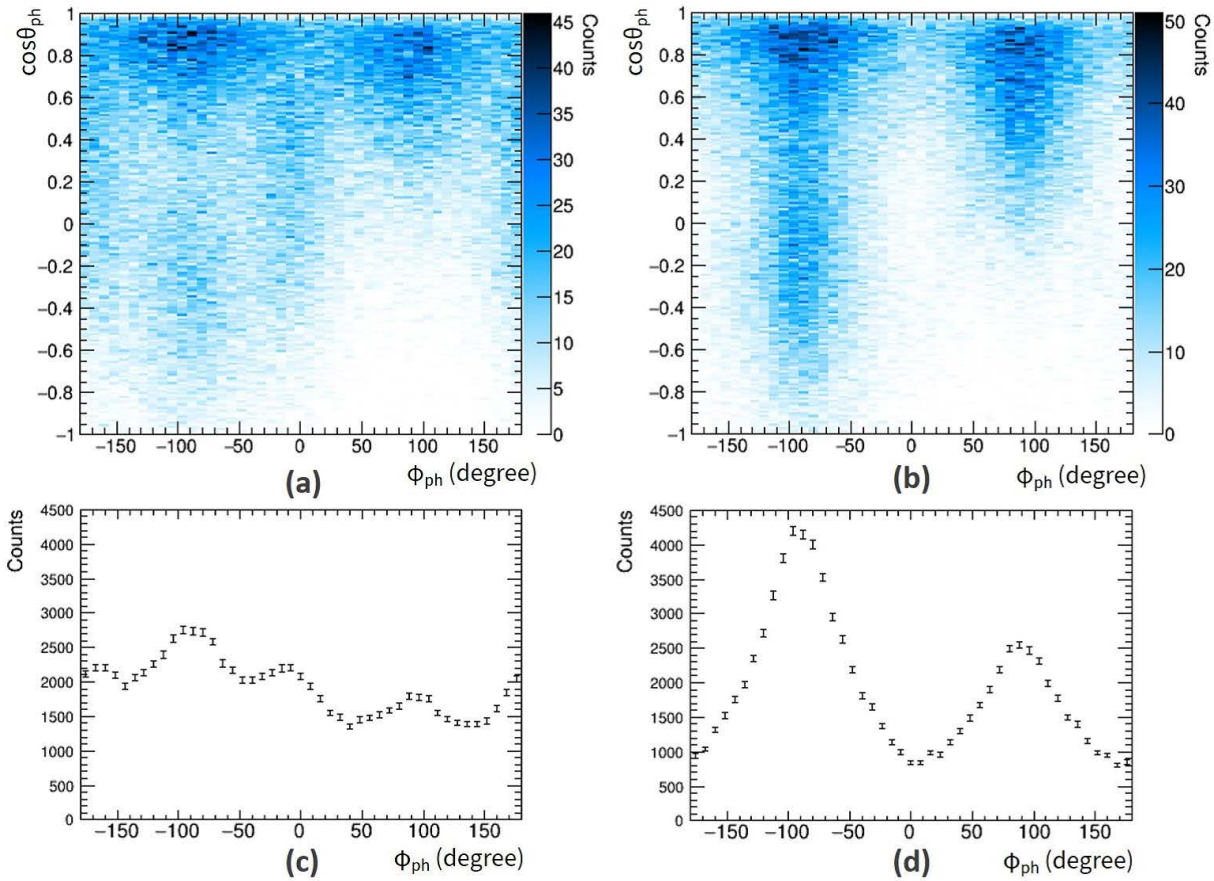

Figure 6.6: Same plots as shown in Figure 6.4 in the photon coordinate system.

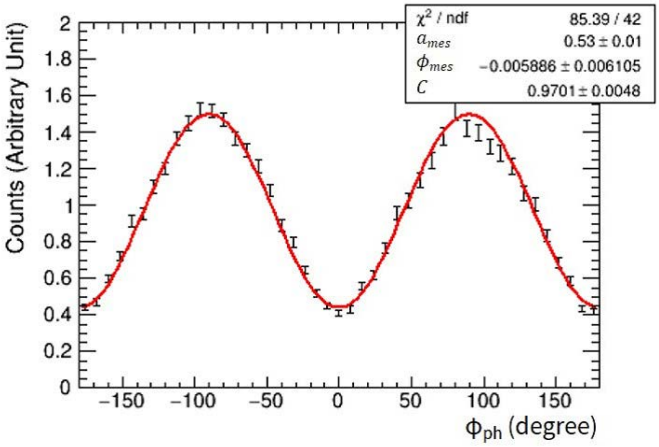

Figure 6.7: Same plots as shown in Figure 6.5 in the photon coordinate system.

6.3 Figures of Merit

As mentioned in Section 3.3, MDP is inversely proportional to $M\sqrt{A}$. Figure 6.8 shows the dependence of M, the relative detection efficiency λ, and $M\sqrt{\lambda}$ on $(\cos\theta)_{max}$ in Equation (6.1), where λ is normalized to 1 at $(\cos\theta)_{max} = 1$. We found that a $(\cos\theta)_{max}$ of 0.7 minimizes the MDP for on-axis incident photons with energies of 200 keV when $M\sqrt{\lambda}$ is at its maximum. Of course, the optimal range of the integration also depends on the incident energy and incident angle, and therefore we need to minimize the MDP for each energy band. For simplification in the following discussion in this thesis, we calculate the integrated azimuthal distribution $\mathcal{N}(\phi)$ in the range of $\cos\theta$ from -1.0 to 0.7.

The simulated response parameters (modulation factor and effective area) for parallel incident gamma-rays are shown in Figure 6.9 (on-axis incidence case) and Figure 6.10 (off-axis incidence case). The energy dependence of Modulation factor in Figure 6.9 mainly derived from the energy dependence of $\overline{\mu}$ as shown in Equation (3.12) and Figure 3.3. The ETCC have the best modulation factor and moderate effective area in the energy range from 150– 200 keV. We found that the modulation factor of the ETCC has a maximum of 0.68 near 150 keV, which is the typical photon energy of GRBs, and the modulation factor at 150 keV decreased by only 10% from 0.68 to 0.62 for an incident angle of 90°. Therefore, we expect that the ETCC could estimate for the effect of an off-axis incidence and has a large FoV for the polarization measurement.

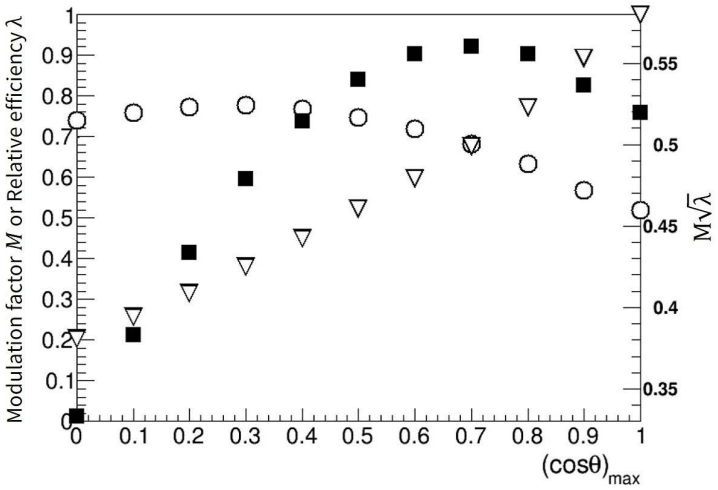

Figure 6.8: Dependences of the modulation factor M (open circles), the relative detection efficiency λ (open triangles), and the figure of merits $M\sqrt{\lambda}$ (filled squares) on the integration region from 0 to θ_{max}. Figure adapted from Komura et al. (2017).

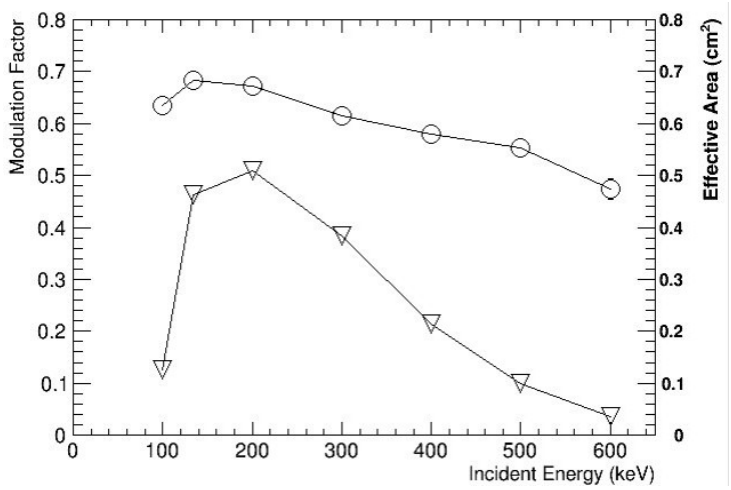

Figure 6.9: The energy dependence of the simulated modulation factor (circles) and the effective area (triangles) of the ETCC for the on-axis incidence of the parallel incident gamma-rays.

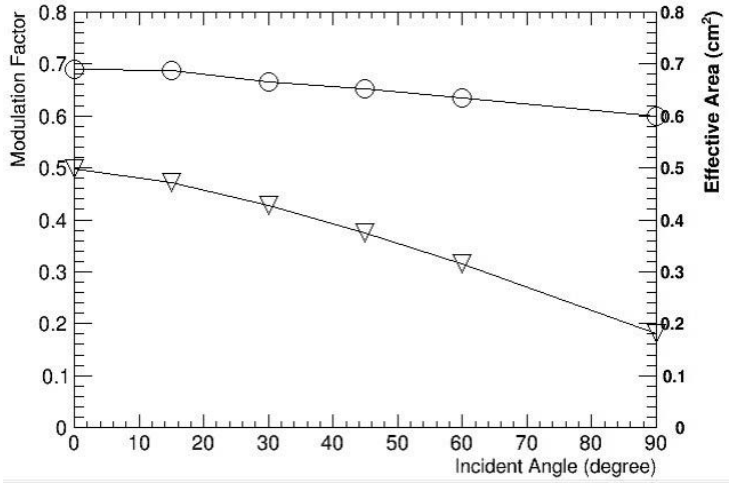

Figure 6.10: Dependence of the simulated modulation factor (circles) and the effective area (triangles) on the incident angle for an incident energy of 154 keV. It is assumed that the incident direction is defined in the Y_{det}-Z_{det} plane of the ETCC's coordinate system and the polarization direction is in the X_{det}-Y_{det} plane.

Chapter 7

Experiment on a Polarized X-ray Beam

We performed two types of experiments from January 27–31, 2015, using the ETCC on the High Energy Inelastic Scattering Beamline BL08W at SPring-8, which supplies a $> 99\%$ linearly polarized hard X-ray beam with an energy of 182 keV.

7.1 Setup of the ETCC

Figure 7.1 is the photograph of the experimental setup. The intensity of the X-ray beam was considerably weakened by 20 cm thick Al attenuators to avoid damage in the ETCC, and to set an acceptable photon rate for the ETCC's electronics. The X-ray beam passed through at 13 cm above the ETCC. The polarization direction of the beam is always horizontal. The front and back sides of the ETCC in the beam direction were shielded by 1mm thick lead sheets to reduce chance coincidence event between the TPC and the PSAs due to ambient X-rays in the laboratory. However, the side faces of the ETCC were not covered because of the lack of lead sheets; a large amount of chance coincidence event occurred as described below.

7.2 On-axis Incident Case

In the first experiment, we measured the modulation factor of the ETCC and compared it with our simulation results for an on-axis beam with various polarization directions. The experimental setup is shown in Figure 7.2(a). We irradiated the X-ray beam to a 10-mm thick aluminum (Al) target, from which X-rays scattered vertically at the target entered the ETCC. The (X_{det}, Y_{det}) coordinates of the beam spot on the Al target were set to (10 mm, 0 mm). Due to spatial limitations in the laboratory, the Al target was located at a height of 13 cm just above the ETCC. Scattered X-rays at the Al target were roughly collimated with an opening window (10 cm $\times$ 10 cm) in the lead blocks set at the top of

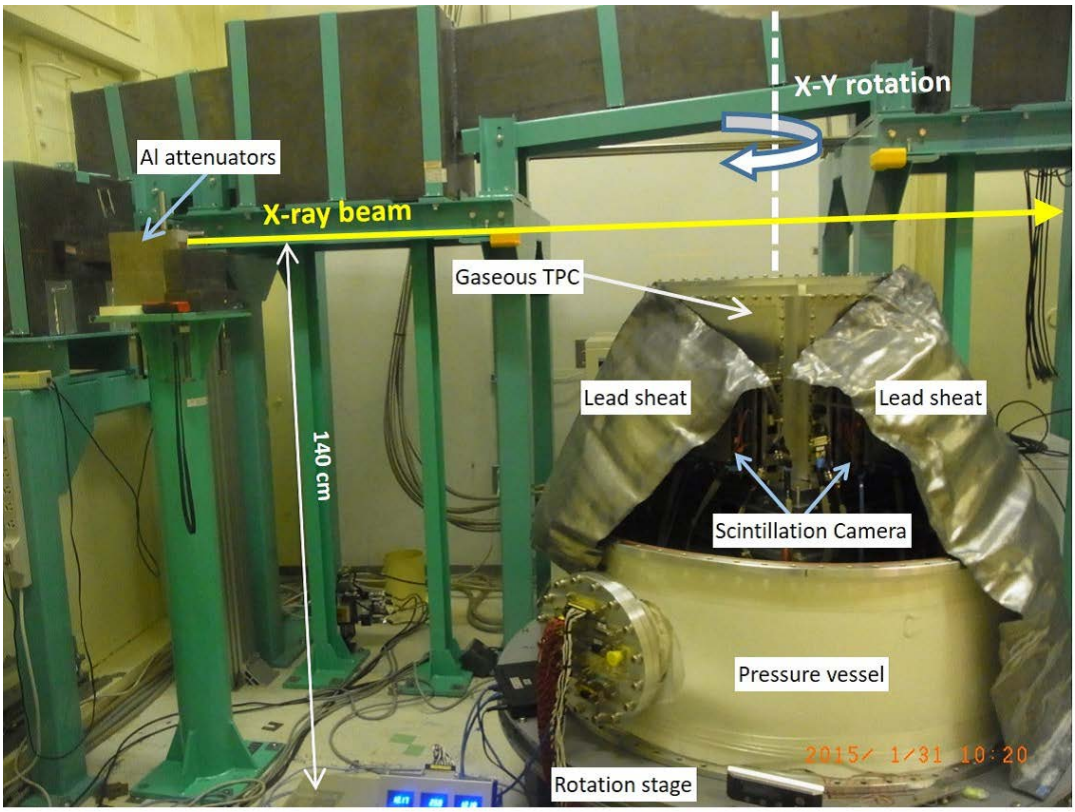

Figure 7.1: Photograph of the ETCC installed for the beam experiment at SPring-8 BL08W.

the TPC as shown in Figure 7.3, and therefore the energy and the degree of polarization of the incident X-rays were widely spread from 123 to 148 keV and from 93% to 98%, respectively. As shown in Figure 7.2(b), the ETCC measured the angular distribution of the Compton scattered X-rays for five different incident X-ray polarization directions by rotating the ETCC around its Z_{det}-axis. First, the azimuthal angle of the polarization direction of the X-ray beam was set to 0°. The event rate with the Al target (on-target measurement) was approximately 300 Hz and contained huge background levels due to air scattering, approximately three times larger than that expected at balloon altitude (Mizumoto et al., 2015). We performed the measurement with no Al target (off-target measurement) for each polarization direction to subtract backgrounds from the on-target data in the off-line analysis.

To obtain correctly reconstructed Compton events, we performed the same event selections mentioned in Section 5.3. First, we selected the correct Compton event, where the recoil electron stops in the TPC, using the relationship between the measured track

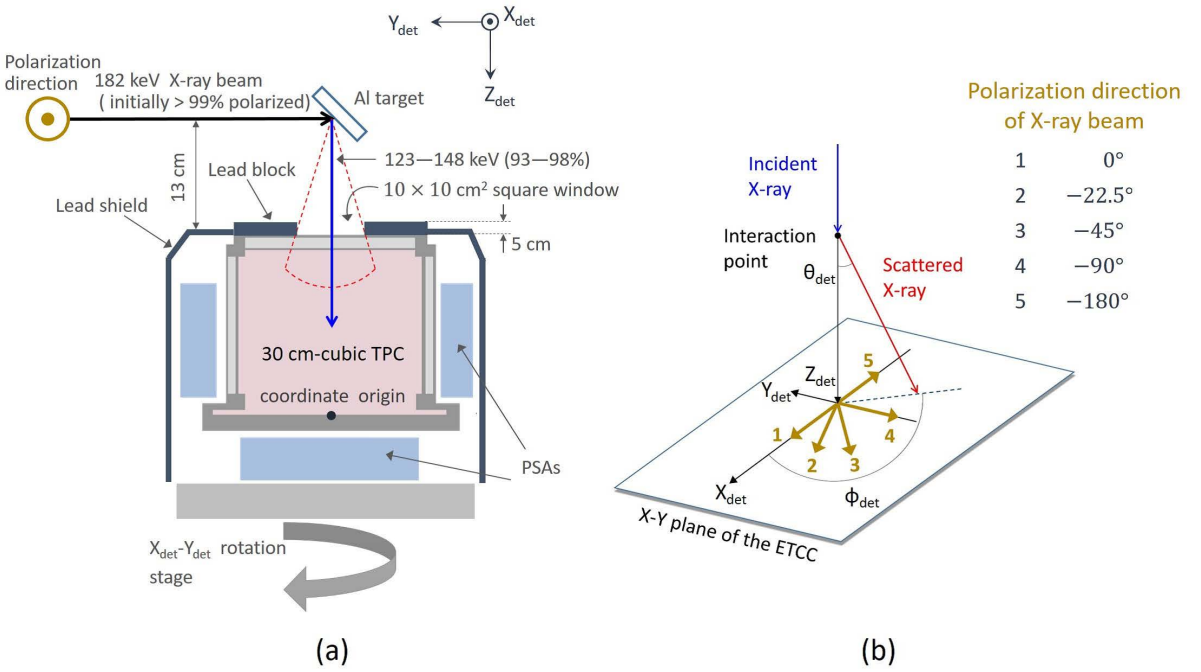

Figure 7.2: (a) A side view in the Y_{det}-Z_{det} plane of the ETCC setup for the first experiments on BL08W at SPring-8. The origin of the coordinate system of the ETCC ($X_{det}Y_{det}Z_{det}$) was set at the bottom center of the TPC. (b) The ETCC measured the angular distribution $\mathcal{D}(\theta_{det}, \phi_{det})$ of the scattered X-ray in the TPC, where θ_{det} and ϕ_{det} are the polar scattering angle and the azimuthal scattering angle, respectively. The measurements were performed for five different polarization directions of the X-ray beam by rotating the ETCC in the X_{det}-Y_{det} plane. The corresponding azimuthal angles are 0°, −22.5°, −45°, −90°, and −180°. Figures adapted from Komura et al. (2017).

range and the energy deposited in the TPC as described below:

$$\left(\frac{\text{Track Range}}{[\text{mm}]}\right) < 4.1 \times 10^3 \left(\frac{\text{Energy Deposit}}{[\text{MeV}]}\right)^{1.8} + 50, \tag{7.1}$$

which is drawn as the solid line in Figure 7.4(a). Next, we selected the events interacting in the fiducial volume of the TPC. Figure 7.4(b) shows the distribution of the analyzed starting positions of the measured tracks (i.e., the Compton scattering positions) along the Z_{det}-axis. The coincidence events between TPC and PSAs lay within the region of approximately -340 mm $< Z_{det} < 0$ mm, which includes both the signal X-rays scattered on the inside of the TPC and the chance coincidence background due to air scattering. The remaining areas are all formed by the chance coincidence background, in which the time lag between incidents on TPC and PSAs is longer than the time window of the coincidence. We defined the fiducial gas volume region as -319.9 mm $< Z_{det} <$ -7.9 mm, and we

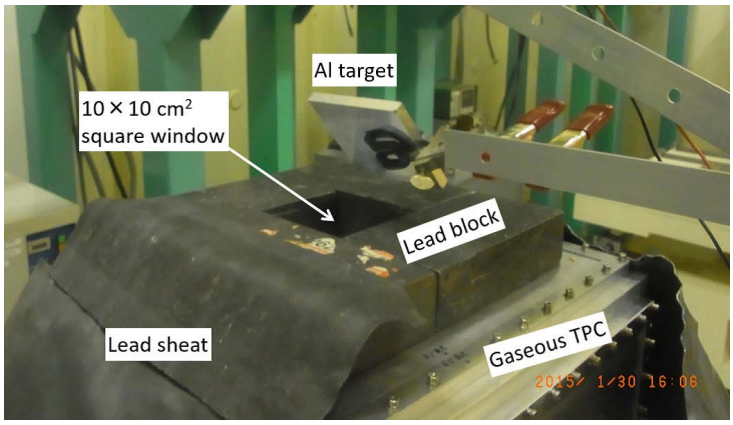

Figure 7.3: Photograph of the roughly collimated opening window at the top of the gaseous TPC.

selected events within this area. Even though chance coincidence events remain after the above removal, we can still estimate the signal-to-background ratio in the fiducial volume of the TPC by assuming that the chance coincidence events are approximately uniformly distributed along the Z_{det}-axis (Mizumoto et al., 2015), which is denoted as the hatched area in Figure 7.4(b). In the case of Figure 7.4(b), we found that the selected events contain approximately 63% of the background, and the signal occupied only one third of the recorded data. Therefore, the experiment was conducted under the background dominant conditions. Because the background in the fiducial volume has the same features as the events occurring outside the fiducial volume, the background component are able to be subtracted using these events.

We confirmed the validity of the above selections using the measured energy spectra of the incident X-rays. As shown in Figure 7.5(a), the spectrum of Al on-target data after the fiducial volume selection expanded to a higher energy region than the expected energy range of 123–148 keV. This means that the chance coincidence backgrounds are coincident with the direct hit of X-rays from the target to PSA and the hit of TPC due to air scattered X-rays. After subtracting the chance coincidence background, we found that the residual energy spectrum is concentrated near the expected energy range. In addition, by subtracting the energy spectrum of off-target measurement, an energy peak near 130 keV appeared, as shown in Figure 7.5(b), which is consistent with the expected energy of incident X-rays scattering at 90° from the Al target, 134 keV; in addition, there is good consistency between the measured and simulated energy spectrums within 10% below 170 keV. Although reconstructed back-projection image of Al target (Figure 7.6) is blurred due to the limitation of the present tracking accuracy of low-energy electron (<40 keV), we found that many events are highly concentrated on the expected region (white dotted line).

To obtain the modulation factor, we selected valid events near an energy peak of 134 keV within the FWHM of the energy resolution of the ETCC (29 keV FWHM at 134

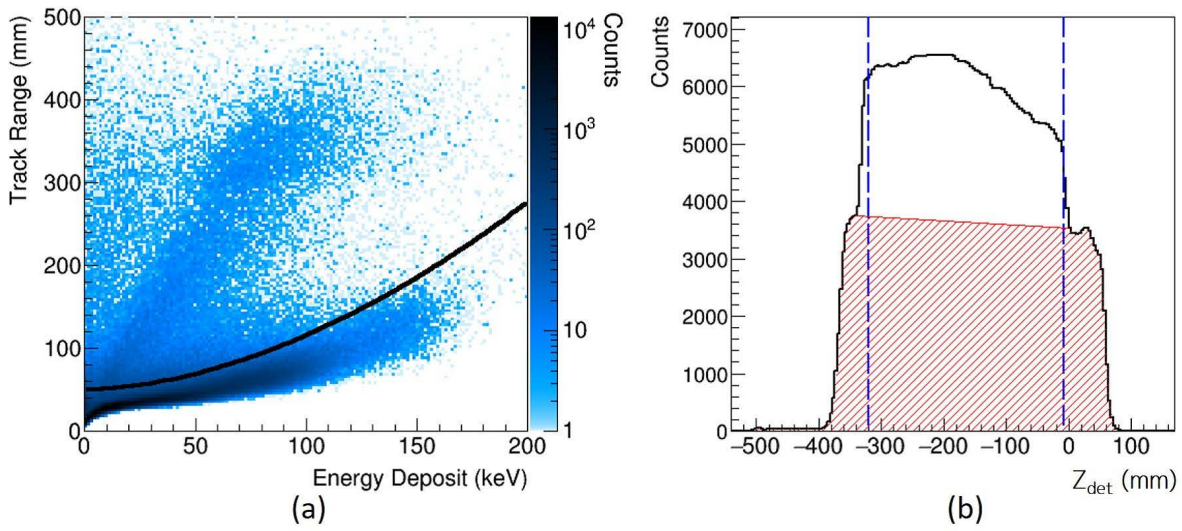

Figure 7.4: (a) Two-dimensional plot of the measured track range and energy deposit in the TPC indicating the energy loss rate (dE/dx) of the charged particles. The solid line represents the selection criteria described in Equation (7.1); the lower side of the line has fully contained electrons stopping in the TPC and the upper side has MIP-like charged particles, such as cosmic muons and high-energy electrons escaping from the TPC. (b) Distribution of Compton scattering position in the TPC along the Z_{det}-axis direction (solid bold line). The hatched area is due to the chance coincidence background. The two vertical dashed lines indicate the fiducial volume region used in this analysis. Figures adapted from Komura et al. (2017).

keV). The degree of polarization of the incident X-rays is estimated to be 96% using the theoretical calculation. Figure 7.7 shows the measured angular distribution of the scattered X-rays, $\mathcal{D}^{mes}_{pol}(\cos\theta_{det}, \phi_{det})$, for a polarization direction of 0°. The calculated azimuthal angle distribution, $\mathcal{N}^{mes}_{pol}(\phi_{det})$, from $\mathcal{D}^{mes}_{pol}(\cos\theta_{det}, \phi_{det})$ is plotted in Figure 7.8, where the simulated azimuthal angle distribution, $\mathcal{N}^{sim}_{pol}(\phi_{det})$, reproduces $\mathcal{N}^{mes}_{pol}(\phi_{det})$ within approximately 8%.

To cancel out the effect due to the non-uniformity of the detector response, we simulated the azimuthal angle distribution for non-polarized photons, $\mathcal{N}^{sim}_{unpol}(\phi_{det})$. Figure 7.9 presents the final azimuthal angle distribution corrected by $\mathcal{N}^{sim}_{unpol}(\phi_{det})$, $\mathcal{N}^{mes}_{cor}(\phi_{det})$ $(= \mathcal{N}^{mes}_{pol}(\phi)/\mathcal{N}^{sim}_{unpol}(\phi_{det}))$, and their best fitting results according to Equation (3.13) for five different polarization directions of the X-ray beam. The obtained modulation factors and polarization angles are summarized in Table 7.1. The ETCC clearly determined the polarization angles for all the measurements within an accuracy of 1°, which are consistent with the polarization directions of the X-ray beam considering the rotation angle accuracy of approximately 0.7°. From these results, we conclude that the modulation factor of the ETCC is in the range of 0.57–0.59 within an error of 0.02. The ideal value of the modulation factors can be obtained by fitting $\mathcal{N}^{sim}_{cor}(\phi_{det})$ $(= \mathcal{N}^{sim}_{pol}(\phi_{det})/\mathcal{N}^{sim}_{unpol}(\phi_{det}))$

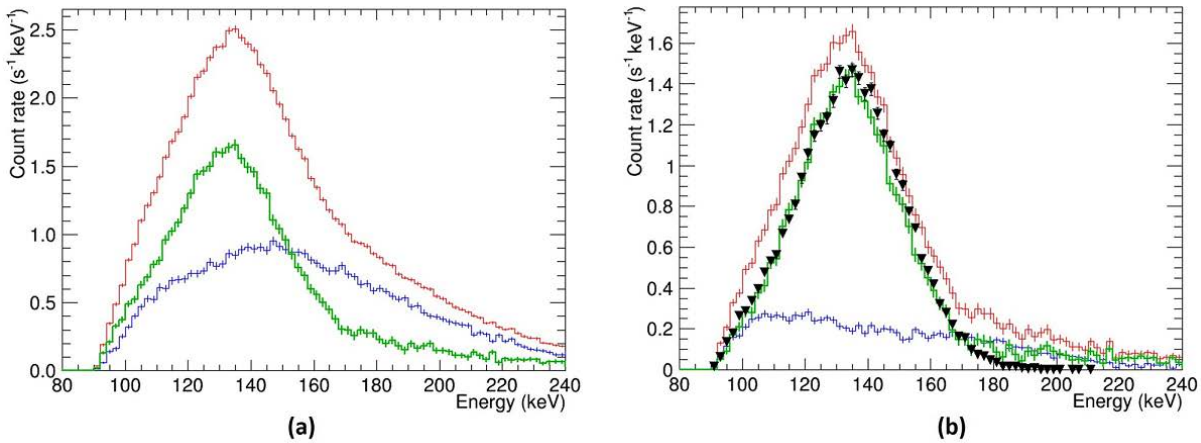

Figure 7.5: (a) Subtraction of the chance coincidence background from the measured energy spectrum of the incident X-rays. The energy spectrum of the Al on-target data after the fiducial volume selection (red), the chance coincidence background (blue), and the residual events (green) after the subtraction of the chance coincidence background are shown. The blue line is obtained by sampling and scaling the energy distribution of the events lying between $Z_{det} < -340$ mm and $Z_{det} > 0$ mm. (b) Subtraction of the Al off-target data and the final reconstructed energy spectrum. The red and blue lines represent the Al on-target and off-target data, respectively, after the removal of the chance coincidence background. The green line represents the residual events after the subtraction of the off-target data, which is in good agreement with the simulated spectrum (filled triangles). The error bars in panels (a) and (b) represent the 1σ statistical error (Komura et al., 2017).

and are also included in Table 7.1. The differences between the measured and simulated modulation factors are larger than the margin of errors due to the small differences in the azimuthal angle distributions and because the uncertainty in the simulation does not take into account the position resolution of the Compton interaction point in the TPC.

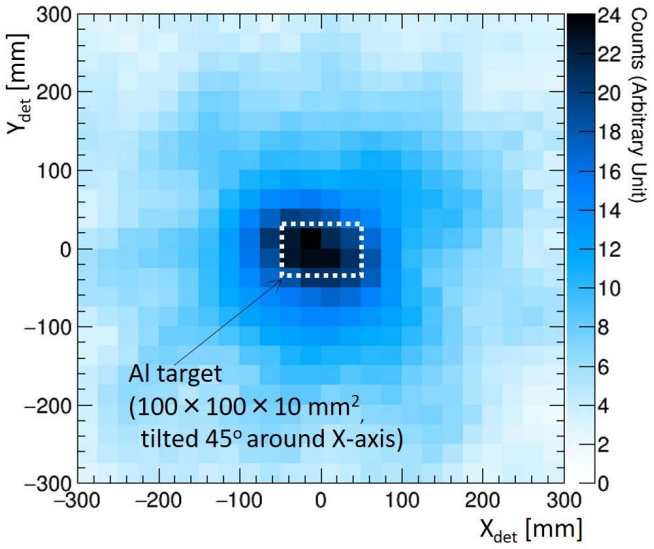

Figure 7.6: Reconstructed back-projection image of Al target.

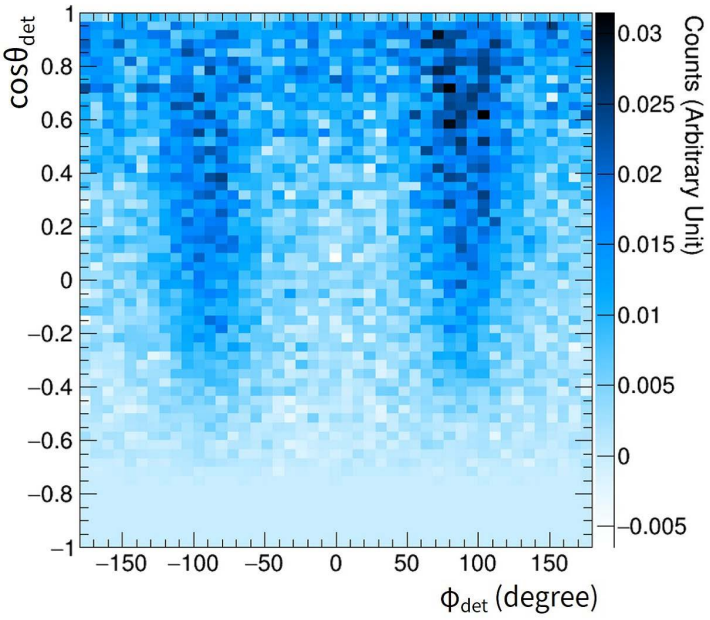

Figure 7.7: Two-dimensional scatter plot of the measured $\mathcal{D}_{pol}^{mes}(\cos\theta_{det}, \phi_{det})$ when the polarization direction of the X-ray beam is 0°. Figure adapted from Komura et al. (2017).

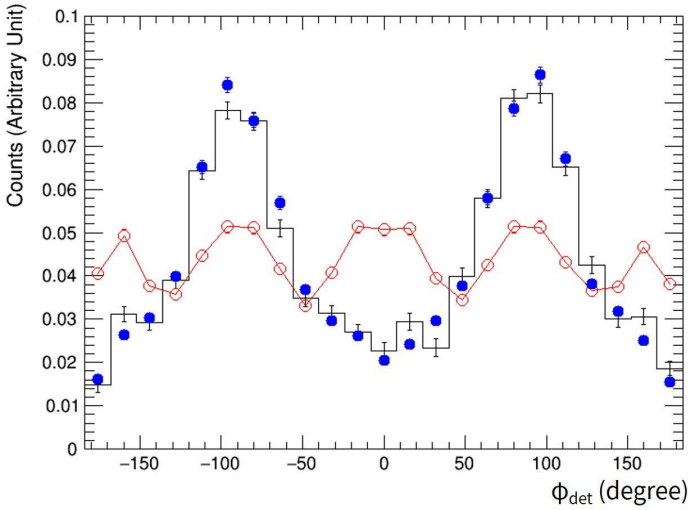

Figure 7.8: The solid line histogram represents the measured azimuthal angle distribution $\mathcal{N}_{pol}^{mes}(\phi_{det})$. The simulation results of the azimuthal angle distribution $\mathcal{N}_{pol}^{sim}(\phi_{det})$ and $\mathcal{N}_{unpol}^{sim}(\phi_{det})$ are plotted as filled circles and open circles, respectively. Figure adapted from Komura et al. (2017).

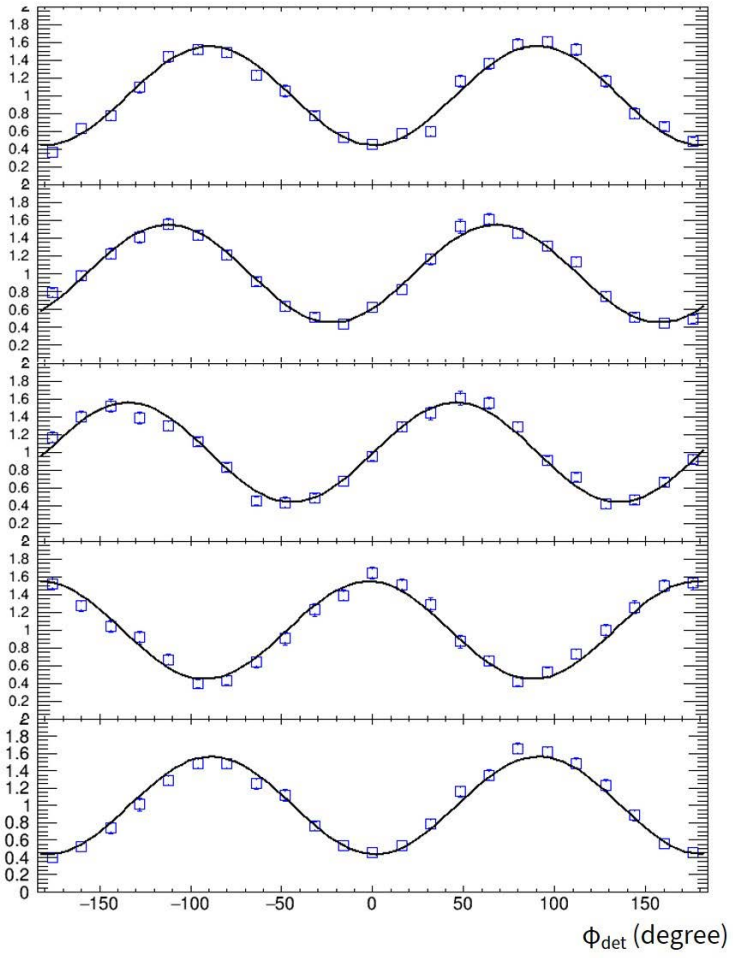

Figure 7.9: Corrected modulation curves (open squares) and the best fit curves (solid lines). The polarization direction of the X-ray beam is 0°, −22.5°, −45°, −90°, and −180°, respectively, from top to bottom. Figure adapted from Komura et al. (2017).

Table 7.1: Fit results of the polarization parameters for five different polarization directions

Polarization direction experimental setup (degree)	Polarization angle measured (degree)	Modulation factor measured	Modulation factor simulated
0	0.4 ± 0.9	0.58 ± 0.02	0.63 ± 0.01
−22.5	−22.3 ± 0.8	0.58 ± 0.02	0.63 ± 0.01
−45	−44.5 ± 0.7	0.58 ± 0.02	0.62 ± 0.01
−90	−92.2 ± 1.0	0.57 ± 0.02	0.60 ± 0.01
−180	−178.7 ± 0.9	0.59 ± 0.03	0.61 ± 0.01

The measured modulation factor is obtained by fitting $\mathcal{N}_{cor}^{mes}(\phi_{det})$, and the simulated modulation factor is obtained by fitting $\mathcal{N}_{cor}^{sim}(\phi_{det})$. These modulation factors and errors are scaled by 0.96, which is the assumed degree of polarization in these measurements.

7.3 Off-axis Incident Case

In the next experiment, we measured the modulation factor of the ETCC for an off-axis beam to demonstrate the cancellation of the effect of off-axis incidence. The experimental setup is shown in Figure 7.10 where the coordinate system of the ETCC, $X_{det}Y_{det}Z_{det}$, and the coordinate system of the incident photon, $X_{ph}Y_{ph}Z_{ph}$, is also defined. The position of the Al target was shifted 20 cm into the upper stream of the beamline compared to that of the previous experiment. Scattered X-rays at the Al target entered the ETCC with a tilted incident angle from the Z_{det}-axis of 20–60°. Even though the energy was widely spread from 147 keV to 179 keV, the degree of polarization was limited to high at 98–99% because the forward scattering events were dominant. Figure 7.11 shows the reconstructed energy spectra of Compton events selected using the same selection method as in the on-axis experiments. An obvious energy peak near 155 keV appeared after the background subtraction, and the shape of the distribution is well reproduced by the simulation within an error of 10%. An energy peak near 155 keV corresponds to the energy of photons with incident angles of approximately 30°, which is consistent with the direction of the reconstructed incident photons projected onto the sphere in Figure 7.12, where the spread of the image is due to the spread of the beam.

To obtain the modulation factor, we selected valid events near the energy peak of 155 keV considering the energy resolution of the ETCC (35 keV FWHM at 155 keV), where the degree of polarization of the incident X-rays is approximately 98%. Figure 7.13 and 7.14(a) show the measured angular distribution of the scattered X-rays, $\mathcal{D}_{pol}^{mes}(\theta_{det}, \phi_{det})$, and the measured azimuthal angle distribution in the $X_{det}Y_{det}Z_{det}$ coordinate system, $\mathcal{N}_{pol}^{mes}(\phi_{det})$, which are distorted by the effect of off-axis incidence. To clearly show the effect of off-axis incidence, we use the range of 0–1 for the integration over $\cos\theta_{det}$ in Equation (6.1) because the forward scattering events with small θ_{det} are concentrated in the positive Y_{det} direction ($\phi_{det} \sim 90°$) and generate large systematic modulations. Al-

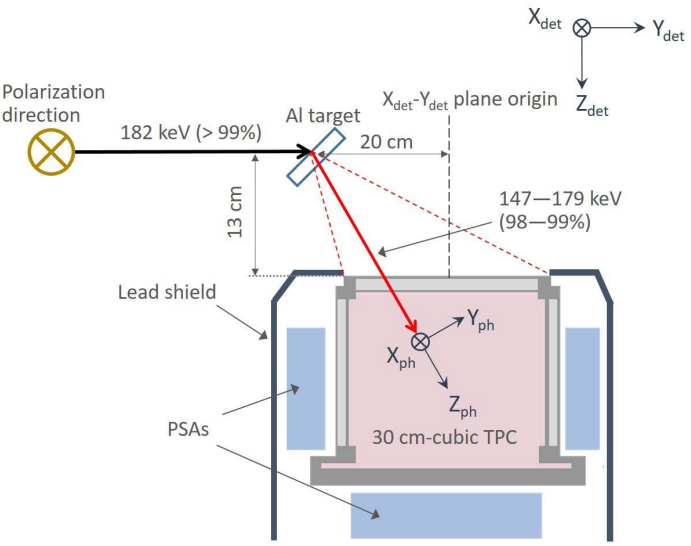

Figure 7.10: A side view in the Y_{det}–Z_{det} plane of the ETCC setup for the second experiment on BL08W at SPring-8. The Al target was shifted 20 cm into the upper stream of the beamline than in the previous experiment. The photon coordinate system $X_{ph}Y_{ph}Z_{ph}$ has the Z_{ph}-axis along the average direction of the incident photons, and the X_{ph}-axis coincides with the X_{det}–Y_{det} plane. Figure adapted from Komura et al. (2017).

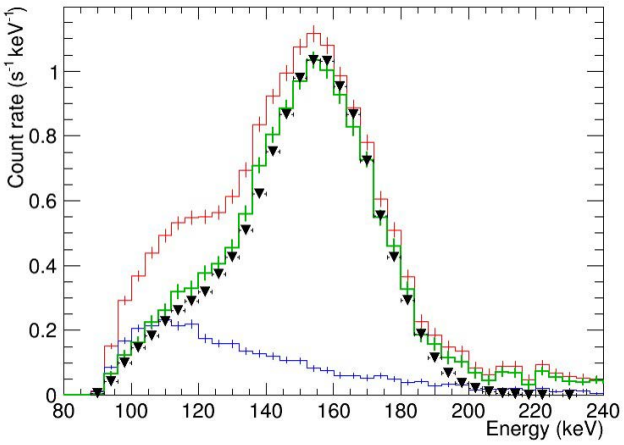

Figure 7.11: Reconstructed energy spectra of the incident photons. The red and blue lines represent the spectra for the Al on-target and off-target data, respectively. The green line is the difference between the red and blue lines, which corresponds to the pure energy spectrum of the incident X-rays after subtracting the background due to air scattering. There is good consistency between the green line and the simulated results (the filled triangles) near the energy peak at 154 keV (Komura et al., 2017).

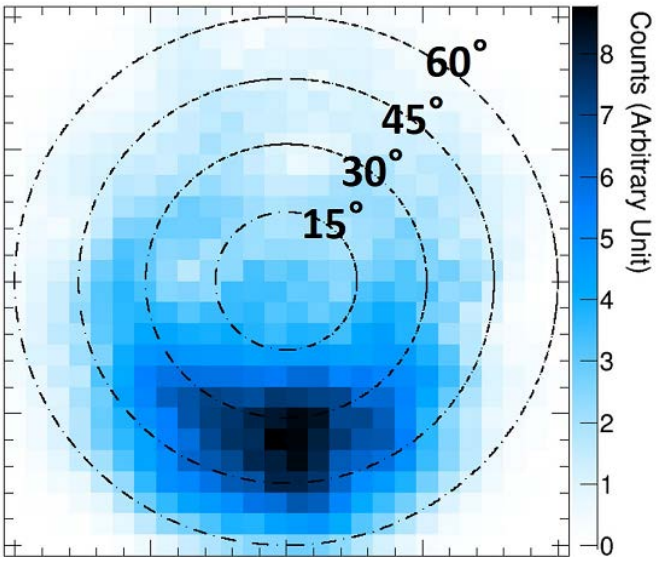

Figure 7.12: Reconstructed image showing the direction of an incident photon. The dotted concentric circles represent the incident angle (15°, 30°, 45°, and 60°) in the coordinate system of the ETCC. The spread in the image corresponds to the spread of the scattered beam. An enhancement is seen within the incident angles of 20–40°, and most events are concentrated near 30° (Komura et al., 2017).

though we would apply the cancellation of the effect due to the non-uniformity of the detector response to $\mathcal{N}_{pol}^{mes}(\phi_{det})$ according to Equation (3.21), the obtained azimuthal angle distribution is far from a symmetrical distribution, as shown in Figure 7.14(b) where the simulated azimuthal angle distribution $\mathcal{N}_{pol}^{sim}(\phi_{det})$ reproduces $\mathcal{N}_{pol}^{mes}(\phi_{det})$ within 8%. It is due to the asymmetric distribution of scattered angle θ_{det} for the Z_{det}-axis and hence the transformation to the photon system is quite essential to the polarization measurement in wide FoV. Therefore, from this response-corrected azimuthal angle distribution, we obtained a worse modulation factor of 0.33 ± 0.01 than that in on-axis incident case. As mentioned in Section 3.2.3, we first have to calculate the azimuthal angle distribution in the $X_{ph}Y_{ph}Z_{ph}$ coordinate system, $\mathcal{N}_{pol}^{mes}(\phi_{ph})$, before canceling out the non-uniform response. Figure 7.15 and Figure 7.16(a) shows the calculated $\mathcal{D}_{pol}^{mes}(\theta_{ph}, \phi_{ph})$ and $\mathcal{N}_{pol}^{mes}(\phi_{ph})$ using the coordinate transformation matrix assuming that the azimuthal and polar angles of the incident photon are 90° and 30°, respectively. Then, we canceled out the effect due to the non-uniformity of the detector response to obtain the response-corrected azimuthal angle distribution, $\mathcal{N}_{cor}^{mes}(\phi_{ph})$, as shown in Figure 7.16(b), where the symmetries are obviously recovered. By fitting $\mathcal{N}_{cor}^{mes}(\phi_{ph})$ with Equation (3.13), the modulation factor is found to be 0.44 ± 0.01, which is improved by a factor of 1.3 compared to Figure 7.14(b). Figure 7.17 shows the best results using an appropriate integration range for $\cos\theta_{ph}$, 0.7 as $(\cos\theta)_{max}$ in Equation (6.1), and a better modulation factor of 0.65 ± 0.01 is obtained. Thus, we consequently obtained same modulation factor compared to that in

on-axis incident case. This experiment clearly demonstrate that the lack of θ_{det} in most Compton polarimeters degrades M and MDP even in the ground-based calibration where $\mathcal{N}_{\Pi=0}(\phi_{det})$ to cancel out the non-uniform response is simulated easily and accurately.

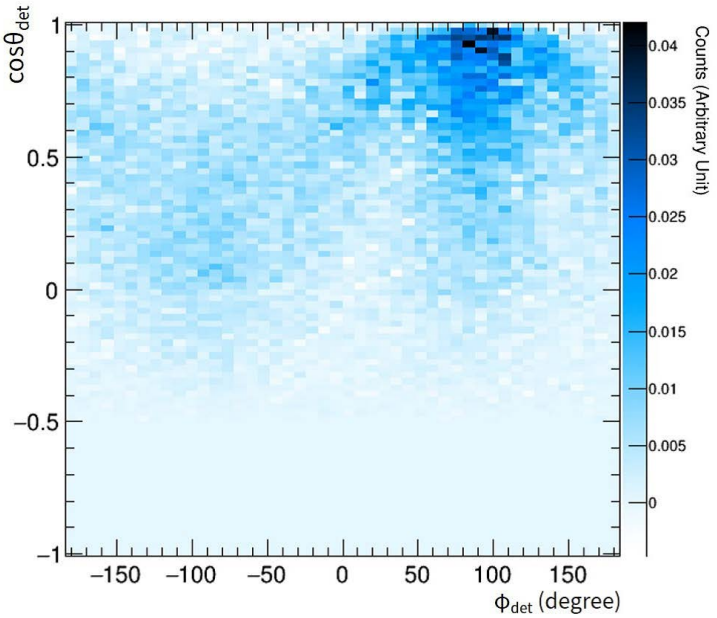

Figure 7.13: Two-dimensional scatter plot of the measured $\mathcal{D}_{pol}^{mes}(\cos\theta_{det}, \phi_{det})$.

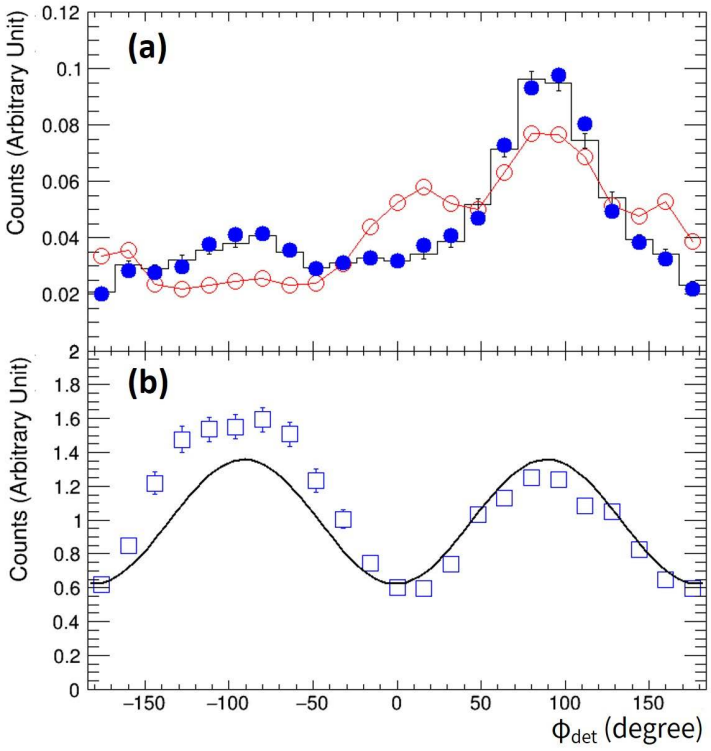

Figure 7.14: (a) Azimuthal angle distributions in the $X_{det}Y_{det}Z_{det}$ coordinate system: $\mathcal{N}_{pol}^{mes}(\phi_{det})$ (solid line histogram), $\mathcal{N}_{pol}^{sim}(\phi_{det})$ (filled circles) and $\mathcal{N}_{unpol}^{sim}(\phi_{det})$ (open circles). (b) Corrected azimuthal angle distribution (open squares) calculated by $\mathcal{N}_{pol}^{mes}(\phi_{det})/\mathcal{N}_{unpol}^{sim}(\phi_{det})$ and the best fitted curve (solid line). Figures adapted from Komura et al. (2017).

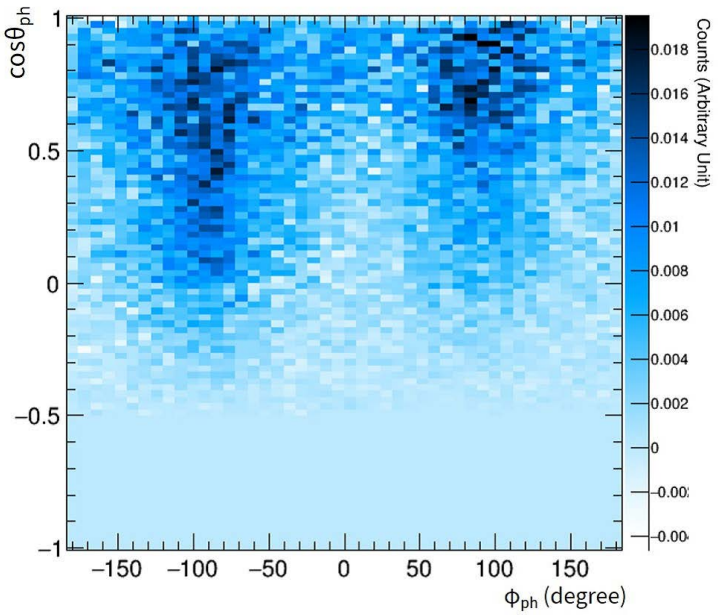

Figure 7.15: Two-dimensional scatter plot of the $\mathcal{D}_{pol}^{mes}(\cos\theta_{ph}, \phi_{ph})$ in the $X_{ph}Y_{ph}Z_{ph}$ coordinate system.

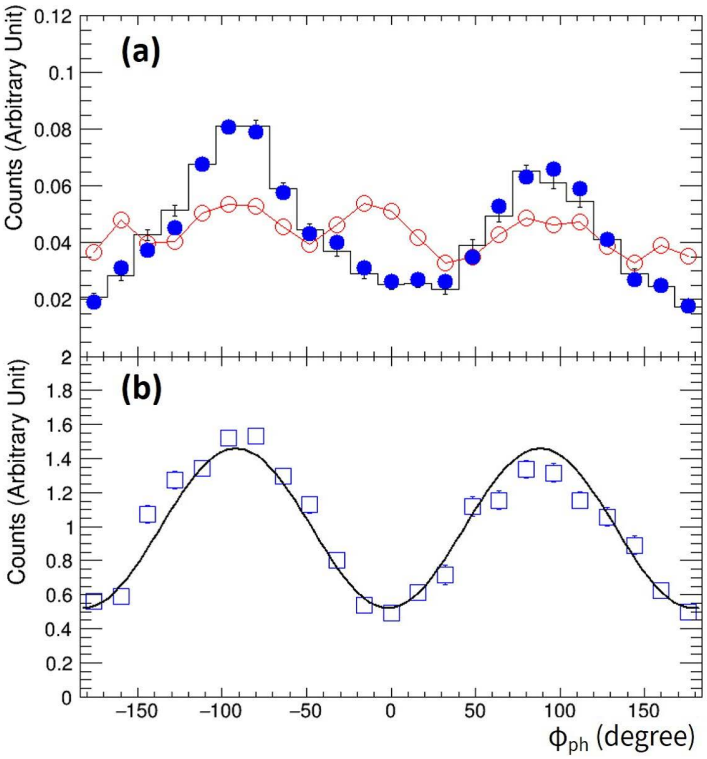

Figure 7.16: Same plots as shown in Figure 7.14 in the $X_{ph}Y_{ph}Z_{ph}$ coordinate system. Figures adapted from Komura et al. (2017).

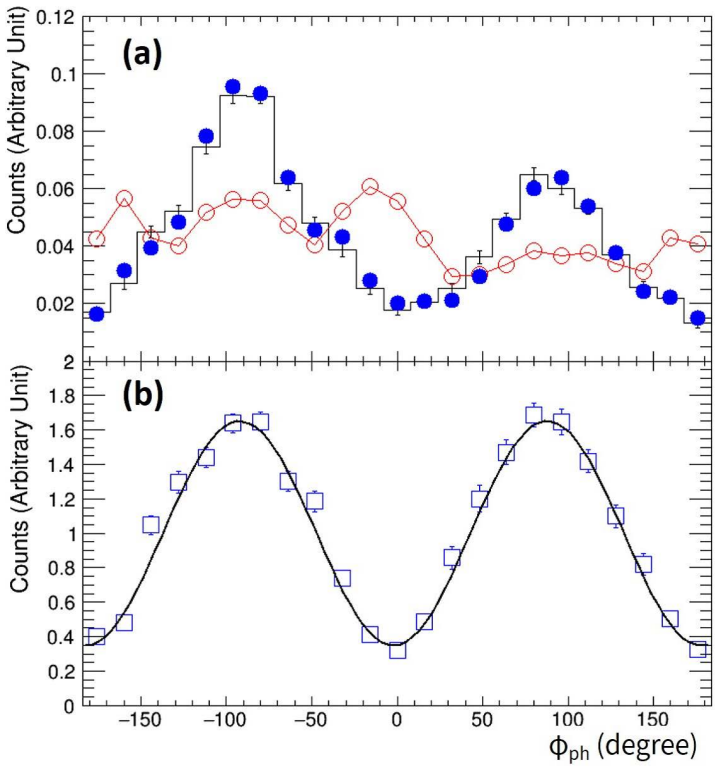

Figure 7.17: Same plots as shown in Figure 7.14 in the $X_{ph}Y_{ph}Z_{ph}$ coordinate system for a $(\cos\theta)_{max}$ of 0.7. Figures adapted from Komura et al. (2017).

Chapter 8

Discussion and Conclusion

We present a novel approach for a gamma-ray imaging spectroscopic polarimeter for all-sky surveys using an ETCC, which provides highly-sensitive polarimetry and imaging spectroscopy based on optics for each object, including both persistent and transient objects within its wide FoV of up to 2π sr all at once. The ETCC provides robust solutions to two major difficulties with wide FoV polarimetry, i.e., huge backgrounds coming from all directions and the degradation of the modulation factor due to the effect of off-axis incidence. It has already been demonstrated that an ETCC efficiently reject both photon and non-photon backgrounds even in intense radiation conditions similar to space using its excellent imaging performance based on a well-defined PSF and its particle identification using dE/dx (Tanimori et al., 2015). Furthermore, the ETCC is expected to maintain its modulation factor without degradation over its wide FoV because it measures all the required information to analytically correct for the effect of off-axis incidence, such as the three-dimensional direction of the scattered photons and the arrival direction and energy of incident photons for each event. To examine these capabilities, we performed a beam test of the current ETCC using a linearly polarized hard X-ray beam at SPring-8. Although there were huge backgrounds of more than twice the polarized X-ray signal, after background rejection, we obtained a modulation factor of 0.58 ± 0.02 at 134 keV for the quasi-on-axis incidence, which includes the deteriorating factor of oblique incident angles of at most 21°. As the greatest impact of this work, we demonstrated for the first time a precise polarization measurement for off-axis incidence with an incident angle of 30° on average; we confirmed that the ETCC can correct the distortion of the measured polarization modulation due to off-axis incidence using the measured gamma-ray image, and the obtained modulation factor was 0.65 ± 0.01 at 154 keV, which is not degraded compared to that of quasi-on-axis incidence. According to the simulated modulation factors for parallel incident gamma-rays as shown in Figure 8.1, we found that the modulation factor of the ETCC has a maximum of 0.68 near 150 keV, which is the typical photon energy of GRBs, and the modulation factor at 150 keV decreased by only 10% from 0.68 to 0.62 for an incident angle of 90°. These simulated modulation factors

are consistent with the experimental ones even though they are affected by non-parallel incidence and large backgrounds. Therefore, we conclude that the ETCC has a promising potential to perform the wide FoV polarimetry maintaining its high modulation factor of over 0.6 near 150 keV, at least for incident angles less than 30°.

We plan to carry on an all-sky imaging survey using the ETCCs, which are improved from the present ETCCs, in long-duration balloons and satellite experiments with 10 times and 100 times, respectively, better sensitivity than that of COMPTEL (Tanimori et al., 2015). In addition, these ETCCs will simultaneously provide polarization measurements of bright objects. First, we will calculate the MDPs in the energy range of 100–300 keV for the balloon observations. For long-duration balloon experiment, we designed an ETCC consisting of 30-cm-cubic ETCC whose effective area would reach 11 cm^2 at 200 keV (Tanimori et al., 2015) and PSF would be 23° at the incident energy of 200 keV and a few degrees over the incident energy of 600 keV (Tanimori et al., 2017). The background rate at balloon altitude is estimated to be approximately 0.11 ph cm^{-2} s^{-1}, which includes extragalactic diffuse gamma-rays, atmospheric gamma-rays, and intrinsic gamma-rays calculated by the Geant4 simulations based on results of previous balloon experiments using a small ETCC (Takada et al., 2011). The MDPs at 99% confidence level for the Crab nebula and Cygnus X-1 are calculated as approximately 20% and 30%, respectively, according to Equation (3.26) in one-day balloon flights with 10 hours of observation. Therefore, the ETCC could confirm the observations of *INTEGRAL*, which reported that the degree of polarization of the Crab nebula is approximately 40% (Dean et al., 2008; Forot et al., 2008). Thanks to the large FoV of the ETCC, we expect to survey transient objects, in particular typical GRBs with moderate brightness. Note that, in observations of transients using ETCC, we do not always need simultaneous observations by other satellites to know the energy and direction of the targets, therefore ETCC can perform polarization measurements of all the GRBs in its FoV. In long-duration balloon experiments, we will use four ETCCs whose effective area would reach 44 cm^2 (4×11 cm^2) at an incident energy of 200 keV. The MDP of an ETCC for GRBs with an intensity 10^{-5} erg cm^{-2} is calculated to be approximately 25%. Even if such GRBs had a long duration of several tens of seconds, it is expected that the MDP will degrade less than 5% thanks to the powerful ETCC background suppression. If we assume that the degree of polarization of the GRBs is greater than 30%, we expect to observe approximately 2–3 GRBs during a one-month balloon-flight; this is estimated from the fluence and the duration parameter T_{90} of GRB samples based on the BATSE Current Gamma-Ray Burst Catalog. Next, we will calculate the MDPs in the energy range of 100–300 keV for the satellite observations. For a middle-class satellite experiment, we designed an ETCC consisting of four 50-cm-cubic ETCCs whose effective area would reach 280 cm^2 (4×70 cm^2) at 200 keV (Tanimori et al., 2015). Using the effective area of the satellite-ETCC, we calculated the MDPs with respect to the source flux as shown in Figure 8.2. We estimate that the MDPs at 13 mCrab would be approximately 10% for an observation time of 10^7 s. Utilizing advantage of wide-FoV, the satellite-ETCC will contribute to the exploration

of polarized serendipity sources as well as major gamma-ray objects, such as AGNs, BBHs, and pulsars at the same level of MDP as that of the pointing X-ray polarimeters. Simultaneously, we expect that the satellite-ETCC will measure over 20 GRBs that have a fluence of more than 6×10^{-6} erg cm^{-2} and polarization degree of more than 10% during a one-year observation. The number of expected GRBs per year is comparable to that of the largest-scale missions, such as POLAR (Orsi & Polar Collaboration, 2011); therefore, the satellite-ETCC will contribute to the desired statistical observations of GRB polarizations.

As discussed in Chapter 3, to achieve the MDP at the same level as that of the pointing X-ray polarimeters, the wide-FoV gamma-ray polarimeter should have the following characteristics: (1) high M and large effective area to suppress the statistical fluctuation of signal photon; (2) imaging ability based on a well-defined PSF to verify the reliability of the correction of non-uniform response and to subtract the background components of $\mathcal{N}(\phi_{det})$; (3) measuring θ_{det} and source direction to cancel out the effect of off-axis incidence; (4) background rejection power to reduce the background contribution to $\mathcal{N}(\phi_{det})$, especially the imaging ability based on a sharp PSF is essential. Although several proposed GRB polarimeters have moderate $M \sim 0.5$ and effective area ~ 100 cm^2, they do not have the capability of imaging and measuring θ_{det}: MDP is largely degraded due to the lack of requirements (2), (3), and (4). Conventional Compton cameras measure both ϕ_{det} and θ_{det} event by event, therefore they have the potential to measure the polarization without the degradation of MDP due to the effect of off-axis incidence. However the source direction is determined as the circle direction, which is not sufficient to defined the PSF and to satisfy requirements (2) and (4). Although Compton camera is effective to observe the very bright GRBs, the MDP become too high to measure the polarization of low signal-to-noise gamma-ray objects. To lower the MDP enough to observe the faint GRBs and persistent objects, the imaging ability based on a well-defined and sharp PSF is essential. Consequently, we conclude that the imaging polarimetry using an ETCC, which has the potential to provide a well-defined and sharp PSF and satisfy all the requirements (1)–(4), is the only approach to perform the all-sky gamma-ray polarization survey for both transient and persistent objects of $\sim$10 mCrab with 10% polarization level.

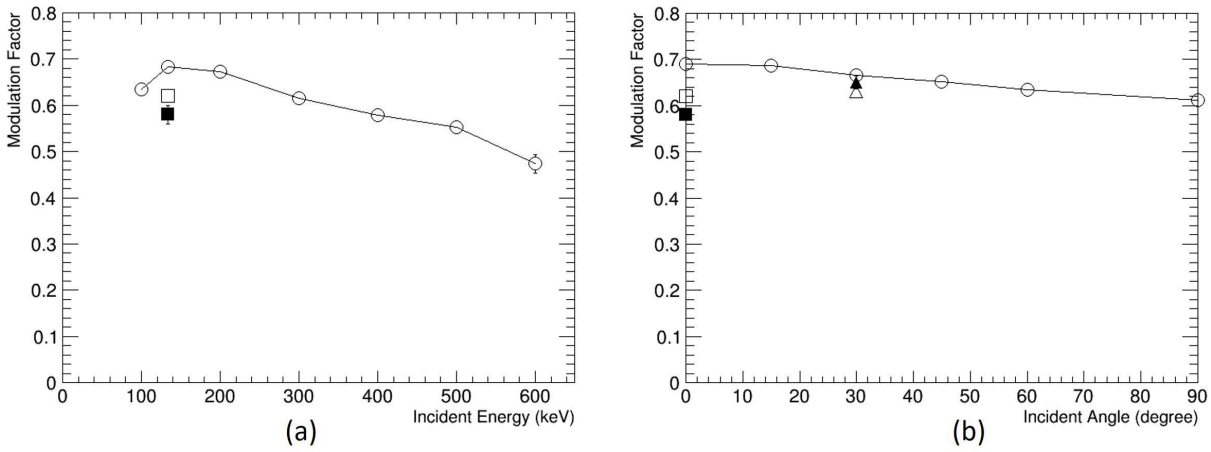

Figure 8.1: (a) The energy dependence of the simulated modulation factor (circles) of the current ETCC for the on-axis incidence of the parallel incident gamma-rays. The measured (filled squares) and simulated (open squares) modulation factors obtained in Section 7.2 are also plotted. The modulation factors of the experiment are 9%–15% smaller than that of the simulated one at 134 keV due to the non-parallel incidence and the residual backgrounds in the experiment. (b) Dependence of the simulated modulation factor (circles) on the incident angle for an incident energy of 154 keV. It is assumed that the incident direction is defined in the Y-Z plane of the ETCC's coordinate system and the polarization direction is in the X-Y plane. The modulation factors obtained in Section 7.2 are plotted at an incident angle of 0° using the same symbols as in panel (a). The measured (filled triangles) and simulated (open triangles) modulation factors obtained in Section 7.3 are also plotted at an incident angle of 30° (Komura et al., 2017).

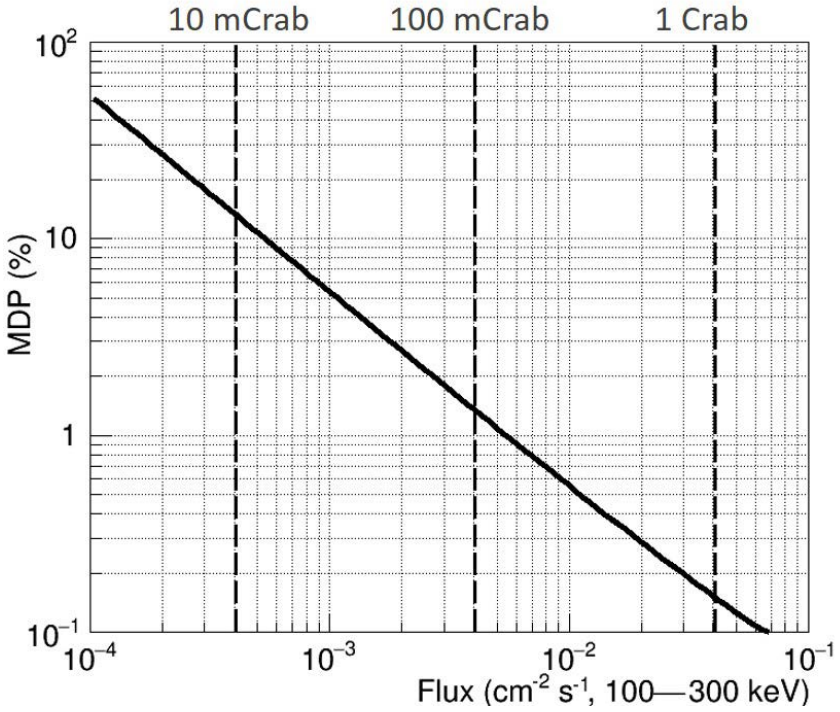

Figure 8.2: Solid line showing the calculated MDPs of the satellite-ETCC as a function of the source flux in the energy range of 100–300 keV for an observation time of 10^7 s. The dashed vertical lines represent source fluxes of 1, 1/10, and 1/100 the Crab nebula (Komura et al., 2017).

Acknowledgments

I am deeply grateful to Prof. Toru Tanimori for his guidance and encouragements in this work. I would also like to my gratitude to Dr. Atsuhi Takada for a plenty of insightful comments. I specially thanks the μ-PIC collaborators: Associate Prof. Hidetoshi Kubo, Dr. Yositaka Mizumura, Dr. Tetsuya Mizumoto, Dr. Shinya Sonoda, Dr. Dai Tomono, Dr. Shunsuke Kurosawa, Dr. Tatsuya Sawano, Yoshihiro Matsuoka, Tetsuro Kishimoto, Shohei Miyamoto, and Taito Takemura. Finally, I would like to thank to my family for having brought me up with continuous encouragements.

This study was supported by a Grant-in-Aid for Scientific Research from the Ministry of Education, Culture, Sports, Science and Technology (MEXT) of Japan (Grant numbers 21224005, 20244026, 23654067, and 25610042), a Grant-in-Aid from the Global COE program, "Next Generation Physics, Spun from Universality and Emergence", from the MEXT of Japan, and a Grant-in-Aid for JSPS Fellows (Grant number 13J01213). This study was also supported by the "SENTAN" program promoted by the Japan Science and Technology Agency (JST). The synchrotron radiation experiments were performed on the BL08W at SPring-8 with the approval of the Japan Synchrotron Radiation Research Institute (JASRI) (Proposal No. 2014B1088). Some of the electronics development was supported by KEK-DTP and the Open-It Consortium.

Bibliography

Agostinelli, S., Allison, J., Amako, K., et al. 2003, Nuclear Instruments and Methods in Physics Research A, 506, 250

Andritschke, R., Zoglauer, A., Kanbach, G., Bloser, P. F., & Schopper, F. 2005, Experimental Astronomy, 20, 395

Band, D., Matteson, J., Ford, L., et al. 1993, ApJ, 413, 281

Baumgartner, W. H., Tueller, J., Markwardt, C. B., et al. 2013, ApJS, 207, 19

Beilicke, M., Kislat, F., Zajczyk, A., et al. 2014, Journal of Astronomical Instrumentation, 3, 1440008

Bloser, P. F., Andritschke, R., Kanbach, G., et al. 2002, New A Rev., 46, 611

Bloser, P. F., Legere, J. S., McConnell, M. L., et al. 2009, Nuclear Instruments and Methods in Physics Research A, 600, 424

Boggs, S. E., Coburn, W., Smith, D. M., et al. 2004, New A Rev., 48, 251

Briggs, M. S., Band, D. L., Kippen, R. M., et al. 1999, ApJ, 524, 82

Bühler, R., & Blandford, R. 2014, Reports on Progress in Physics, 77, 066901

Chauvin, M., Jackson, M., Kawano, T., et al. 2016a, Astroparticle Physics, 82, 99

Chauvin, M., Florén, H.-G., Jackson, M., et al. 2016b, MNRAS, 456, L84

Chauvin, M., Floren, H.-G., Friis, M., et al. 2017, Scientific Reports, 7, 7816

Chauvin, M., Friis, M., Jackson, M., et al. 2017, Nuclear Instruments and Methods in Physics Research A, 859, 125

Chiu, J.-L., Boggs, S. E., Chang, H.-K., et al. 2015, Nuclear Instruments and Methods in Physics Research A, 784, 359

Coburn, W., & Boggs, S. E. 2003, Nature, 423, 415

Costa, E., Frontera, F., Heise, J., et al. 1997, Nature, 387, 783

Covino, S., & Gotz, D. 2016, Astronomical and Astrophysical Transactions, 29, 205

Dean, A. J., Clark, D. J., Stephen, J. B., et al. 2008, Science, 321, 1183

Fishman, G. J. 1999, A&AS, 138, 395

Forot, M., Laurent, P., Grenier, I. A., Gouiffès, C., & Lebrun, F. 2008, ApJ, 688, L29

Goldstein, A., Preece, R. D., Mallozzi, R. S., et al. 2013, ApJS, 208, 21

Gunji, S., Nakamori, T., Sakano, M., et al. 2014, in Proc. SPIE, Vol. 9144, Space Telescopes and Instrumentation 2014: Ultraviolet to Gamma Ray, 91444J

Guo, Q. 2014, Arts & Sciences Electronic Theses and Dissertations. 373.

Hughes, J. P., Long, K. S., & Novick, R. 1984, ApJ, 280, 255

Iwakiri, W. B., Black, J. K., Cole, R., et al. 2016, Nuclear Instruments and Methods in Physics Research A, 838, 89

Kalemci, E., Boggs, S. E., Kouveliotou, C., Finger, M., & Baring, M. G. 2007, ApJS, 169, 75

Kanbach, G., Andritschke, R., Bloser, P. F., et al. 2003, in Proc. SPIE, Vol. 4851, X-Ray and Gamma-Ray Telescopes and Instruments for Astronomy., ed. J. E. Truemper & H. D. Tananbaum, 1209–1220

Katsuta, J., Edahiro, I., Watanabe, S., et al. 2016, Nuclear Instruments and Methods in Physics Research A, 840, 51

Khalil, M., Laurent, P., Lebrun, F., et al. 2016, Nuclear Instruments and Methods in Physics Research A, 835, 74

Kierans, C. A., Boggs, S. E., Chiu, J.-L., et al. 2017, ArXiv e-prints, arXiv:1701.05558

Kislat, F., Beheshtipour, B., Dowkontt, P., et al. 2017, Journal of Astronomical Instrumentation, 6, 1740003

Klein, O., & Nishina, T. 1929, Zeitschrift fur Physik, 52, 853

Kole, M., Bao, T. W., Batsch, T., et al. 2016, ArXiv e-prints, arXiv:1612.04098

Komura, S., Tanimori, T., Kubo, H., et al. 2013, in 2013 IEEE Nuclear Science Symposium and Medical Imaging Conference (2013 NSS/MIC), IEEE, 1–5

Komura, S., Takada, A., Mizumura, Y., et al. 2017, ApJ, 839, 41

Kouveliotou, C., Meegan, C. A., Fishman, G. J., et al. 1993, ApJ, 413, L101

Krawczynski, H., Garson, A., Guo, Q., et al. 2011, Astroparticle Physics, 34, 550

Krawczynski, H. S., Stern, D., Harrison, F. A., et al. 2016, Astroparticle Physics, 75, 8

Krivonos, R., Tsygankov, S., Lutovinov, A., et al. 2015, MNRAS, 448, 3766

Kurfess, J. D., Johnson, W. N., Kroeger, R. A., et al. 2004, New A Rev., 48, 293

Laurent, P., Rodriguez, J., Wilms, J., et al. 2011, Science, 332, 438

Lei, F., Dean, A. J., & Hills, G. L. 1997, Space Sci. Rev., 82, 309

Lei, F., Hills, G. L., Dean, A. J., & Swinyard, B. M. 1996, A&AS, 120, 695

Long, K. S., Chanan, G. A., & Novick, R. 1980, ApJ, 238, 710

Lowell, A. W., Boggs, S. E., Chiu, J.-L., et al. 2017, ArXiv e-prints, arXiv:1709.05349

Madejski, G. ., & Sikora, M. 2016, ARA&A, 54, 725

Mallozzi, R. S. 2014, Durations of the 4B Catalog Gamma-Ray Bursts recorded with the BATSE on board CGRO, , . https://gammaray.nsstc.nasa.gov/batse/grb/duration/

Matsuoka, Y., Tanimori, T., Kubo, H., et al. 2015, Journal of Instrumentation, 10, C01053

McConnell, M. L. 2017, New A Rev., 76, 1

McConnell, M. L., Bancroft, C., Bloser, P. F., et al. 2009, in Proc. SPIE, Vol. 7435, UV, X-Ray, and Gamma-Ray Space Instrumentation for Astronomy XVI, 74350J

McConnell, M. L., Ryan, J. M., Smith, D. M., Lin, R. P., & Emslie, A. G. 2002, Sol. Phys., 210, 125

McConnell, M. L., Smith, D. M., Emslie, A. G., et al. 2004, Advances in Space Research, 34, 462

McNamara, A. L., Kuncic, Z., & Wu, K. 2009, MNRAS, 395, 1507

Mizumoto, T., Matsuoka, Y., Mizumura, Y., et al. 2015, Nuclear Instruments and Methods in Physics Research A, 800, 40

Moiseev, A. A., Ajello, M., Buckley, J. H., et al. 2015, ArXiv e-prints, arXiv:1508.07349

Muleri, F. 2014, ApJ, 782, 28

Nagayoshi, T., Kubo, H., Miuchi, K., et al. 2004, Nuclear Instruments and Methods in Physics Research A, 525, 20

Nishimura, H., Hattori, K., Kabuki, S., et al. 2007, Nuclear Instruments and Methods in Physics Research A, 573, 115

Nolan, P. L., Abdo, A. A., Ackermann, M., et al. 2012, ApJS, 199, 31

Ochi, A., Nagayoshi, T., Koishi, S., et al. 2002, Nuclear Instruments and Methods in Physics Research A, 478, 196

Ogasaka, Y., Tueller, J., Yamashita, K., et al. 2005, in Proc. SPIE, Vol. 5900, Optics for EUV, X-Ray, and Gamma-Ray Astronomy II, ed. O. Citterio & S. L. O'Dell, 217–224

O'Neill, T. J., Akyuez, A., Bhattacharya, D., et al. 1996, A&AS, 120, 661

Orsi, S., & Polar Collaboration. 2011, Astrophysics and Space Sciences Transactions, 7, 43

Poutanen, J. 1994, ApJS, 92, 607

Rao, A. R., Chand, V., Hingar, M. K., et al. 2016, ApJ, 833, 86

Romero, G. E., Vieyro, F. L., & Chaty, S. 2014, A&A, 562, L7

Roques, J. P., Schanne, S., von Kienlin, A., et al. 2003, A&A, 411, L91

Rutledge, R. E., & Fox, D. B. 2004, MNRAS, 350, 1288

Sauli, F. 1977, Principles of operation of multiwire proportional and drift chambers, Tech. rep., European Organization for Nuclear Research

Sauli, F. 1997, Nuclear Instruments and Methods in Physics Research A, 386, 531

Sauli, F. 2016, Nuclear Instruments and Methods in Physics Research Section A: Accelerators, Spectrometers, Detectors and Associated Equipment, 805, 2 , special Issue in memory of Glenn F. Knoll. http://www.sciencedirect.com/science/article/pii/S0168900215008980

Sawano, T. 2017, Ph.D. thesis, Kyoto University

Sawano, T., Tanimori, T., Kubo, H., et al. 2014, JPS Conference Proceedings, 1, 013099

Schnittman, J. D., & Krolik, J. H. 2010, ApJ, 712, 908

Schoenfelder, V., Aarts, H., Bennett, K., et al. 1993, ApJS, 86, 657

Schönfelder, V. 2004, New A Rev., 48, 193

Schönfelder, V., Bennett, K., Blom, J. J., et al. 2000, A&AS, 143, 145

Smith, D. M., Lin, R. P., Turin, P., et al. 2002, Sol. Phys., 210, 33

Soffitta, P., Barcons, X., Bellazzini, R., et al. 2013, Experimental Astronomy, 36, 523

Takada, A. 2007, Ph.D. thesis, Kyoto University

Takada, A., Hattori, K., Kabuki, S., et al. 2007, Nuclear Instruments and Methods in Physics Research A, 573, 195

Takada, A., Kubo, H., Nishimura, H., et al. 2011, ApJ, 733, 13

Tamagawa, T., Tsunoda, N., Hayato, A., et al. 2006, Nuclear Instruments and Methods in Physics Research A, 560, 418

Tanimori, T., Kubo, H., Miuchi, K., et al. 2004, New A Rev., 48, 263

Tanimori, T., Kubo, H., Takada, A., et al. 2015, ApJ, 810, 28

Tanimori, T., Mizumura, Y., Takada, A., et al. 2017, Scientific Reports, 7, 41511

Tatischeff, V., Tavani, M., von Ballmoos, P., et al. 2016, in Proc. SPIE, Vol. 9905, Society of Photo-Optical Instrumentation Engineers (SPIE) Conference Series, 99052N

Toma, K., Sakamoto, T., Zhang, B., et al. 2009, ApJ, 698, 1042

Ubertini, P., Lebrun, F., Di Cocco, G., et al. 2003, A&A, 411, L131

Vadawale, S. V., Rao, A. R., Bhattacharya, D., et al. 2016, in Proc. SPIE, Vol. 9905, Space Telescopes and Instrumentation 2016: Ultraviolet to Gamma Ray, 99051G

Vedrenne, G., Roques, J.-P., Schönfelder, V., et al. 2003, A&A, 411, L63

Weidenspointner, G., Varendorff, M., Oberlack, U., et al. 2001, A&A, 368, 347

Weisskopf, M. C., Elsner, R. F., & O'Dell, S. L. 2010, in Proc. SPIE, Vol. 7732, Space Telescopes and Instrumentation 2010: Ultraviolet to Gamma Ray, 77320E

Weisskopf, M. C., Silver, E. H., Kestenbaum, H. L., Long, K. S., & Novick, R. 1978, ApJ, 220, L117

Weisskopf, M. C., Ramsey, B., O ' Dell, S. L., et al. 2016, Results in Physics, 6, 1179

Wigger, C., Hajdas, W., Arzner, K., Güdel, M., & Zehnder, A. 2004, ApJ, 613, 1088

Winkler, C., Courvoisier, T. J.-L., Di Cocco, G., et al. 2003, A&A, 411, L1

Xiong, S., Produit, N., & Wu, B. 2009, Nuclear Instruments and Methods in Physics Research A, 606, 552

Yatsu, Y., Ito, K., Kurita, S., et al. 2014, in Proc. SPIE, Vol. 9144, Space Telescopes and Instrumentation 2014: Ultraviolet to Gamma Ray, 91440L

Yonetoku, D., Murakami, T., Gunji, S., et al. 2011a, PASJ, 63, 625

—. 2011b, ApJ, 743, L30

Zdziarski, A. A., Poutanen, J., Paciesas, W. S., & Wen, L. 2002, ApJ, 578, 357

Zhang, H., & Böttcher, M. 2013, ApJ, 774, 18

Zoglauer, A., Andritschke, R., Kanbach, G., Bloser, P. F., & Litvinenko, V. N. 2004, in ESA Special Publication, Vol. 552, 5th INTEGRAL Workshop on the INTEGRAL Universe, ed. V. Schoenfelder, G. Lichti, & C. Winkler, 921